공학박사학위논문

통합 로봇-비전 시스템 기반의 의류 제조 공정 자동화

Seamless Automation of Garment Manufacturing Enabled by Integrated Vision and Robotic Manipulation

2023 년 8 월

서울대학교 대학원

기계항공공학부

구 수 병

통합 로봇-비전 시스템 기반의 의류 제조 공정 자동화

Seamless Automation of Garment Manufacturing Enabled by Integrated Vision and Robotic Manipulation

지도교수 박 용 래

이 논문을 공학박사 학위논문으로 제출함

2023 년 4 월

서울대학교 대학원

기계항공공학부

구 수 병

구수병의 공학박사 학위논문을 인준함

2023 년 6 월

위 원 장 : 안 성 훈 (인)

부위원장 : 박 용 래 (인)

위 원 : 김 호 영 (인)

위 원 : 한 경 원 (인)

위 원 : 허 태 명 (인)

Abstract

Smart manufacturing environments make manufacturing more efficient, enable flexible production, and increase safety by allowing robots to replace human operators in hazardous environments. The labor-intensive garment manufacturing industries are in high demand of robotic systems. However, automation of garment manufacturing has been delayed by the lack of technologies for reliable recognition of target objects, handling capabilities of delicate fabrics, and methods of dexterous manipulation that can safely interact with humans while handling the target fabric. These obstacles can be overcome with machine intelligence combined with computer vision, dexterous grippers that handle highly deformable objects, and manipulators that are safe to and interactive with human operators.

This thesis proposes three robotic manipulation techniques to automate garment production and support handling of deformable fabrics. First, an automated sewing system enabled by computer vision is proposed for autonomous operation without human intervention. Second, a soft robotic gripper is proposed to enable the delicate handling of fabrics. Third, a soft modularized robotic arm with proprioception is proposed to interact safely with humans.

First, a custom-built automated production system is proposed by integrating computer vision with a commercial sewing machine. The camera for the computer vision system captures the target fabrics, called assembled patterns that consist of clothes and a seam line. The region of interest (ROI) including the seam line in the image is segmented by a trained deep learning model, and the seam line is determined by the proposed image processing algorithms. Determining the seam line is possible regardless of the exposure time and the color

of the patterns, and it is also insensitive to noise and irregularities. The sewing path is generated based on the seam line, and the generated path is transmitted to the custom-built sewing machine and perform sewing task autonomously.

Second, a soft gripper for manipulating deformable and highly flexible fabrics is proposed. The proposed gripper with a small form factor is able to pick up a single sheet of fabric by pinching enabled by the structural deformation of the gripper. The gripper is able to pick up not only meshed fabrics with high air permeability but also coated ones that are not air permeable. By measuring the capacitance between the two fingers while holding fabrics with the electrodes attached to the fingers, the number of held by the gripper sheets can be estimated, which helps enhancing the reliability of the gripping process. Based on this gripper, a more advanced soft gripper with an added function of vacuum suction to the function of structural pinching realized in a single gripper structure is proposed. In addition, a multi-functional compliant structure is added to the gripper to easily conform to the stack of the target fabric by distributing the excessive load on the fingertip. An air pressure sensor, connected to the compliant structure, detects the contact, and controls the pressing force for automating the fabric handling process. The number of fabric sheets held by the gripper can be estimated by a deep learning model using computer vision. This requires neither prior knowledge on the fabric nor measurements. The proposed gripper is also able to detect the air permeability of the fabric, to select a proper actuation mode, and separate a single sheet from the stack.

Lastly, a soft modularized robotic arm is proposed for functional interaction with humans. The proposed robotic arm is composed of three pneumatic bellow actuators that have a complex

structure with embedded channels, easily fabricated with 3D printing. By filling the channel with organogel, a human touch can be independently recognized. A manipulator module, which is part of the robotic arm, is composed of pneumatic bellows, sensing solutions, and a control system. Since a manipulator module can contract, expand, and bend in different directions, omnidirectional soft string sensors are developed correspondingly. The manipulator module is controlled by soft string sensors, an inertial measurement unit, and a red-green-blue (RGB) camera. The manipulator module can recognize its surroundings and be controlled by sensor fusion of the string sensors and the computer vision, or it can be solely controlled in occlusion environments by string sensors. The soft robotic arm, made of multiple modules connected in series, can be integrated either with a conventional robotic gripper or the proposed soft gripper for assisting the human or for handling the fabric.

Keyword: Smart manufacturing, Machine vision, Multi-functional structure, Soft gripper, Soft robotic arm

Student Number: 2017-23754

Acknowledgement

My meaningful time as a graduate student comes to a close, I would like to express my gratitude to those who helped me along the way. First and the most, I would like to express my sincere gratitude to my advisor, Professor Yong-Lae Park. He was always supportive and encouraging of my research and patiently waited for me to be free to conduct my own research. He also provided me with directions to strengthen the relevance of my research to the field of soft robotics and guided me to be a researcher with research ethics and competence.

I also would like to express gratitude to my defense committee members: Professor Sung-Hoon Ahn, Professor Ho-Young Kim, Professor Amy Kyoungwon Han, Professor Taemyung Huh. From their research experience and knowledge, they advised me on what I needed to improve my research and helped me develop insights. It was a great honor for me to share and present my research experience with them.

Thanks to all of outstanding and brilliant colleagues at Soft Robotics and Bionics Lab. in Seoul National University. Especially, Byung-Hyun Song, Taejun Park, Professor Younghoon Lee, HyunWoong Choi, Taehwan Kim, and Jaejin Kim deserve my gratitude for their constructive and informative discussions on research directions and their supporting. Byung-Hyun Song always gave me creative research ideas and enthusiasm and helped me improve my research with logical analysis. Taejun Park helped me to make liquid metal sensors using a dispenser and conduct challenging experiment and was kind enough around his busy schedule. Professor Younghoon Lee helped me to develop tribo-sensitive bellow with Organogel and gave me lots of opportunity to develop my insights and capabilities.

HyunWoong Choi helped me to develop vision algorithm for seam line detection and apply the vision algorithm to the real-world robotic system. Taehwan Kim, HyunWoong Choi, Jaejin Kim, and Byung-Hyun Song were members of the garment smart factory project in our lab with me and I would like to express apology and gratitude. I appreciated the effort they put into making the project a success, and I apologized for not being able to inspire their own research. Their devotion and dedication helped my research as well. Outside of research, I would like to thank Taekyoung Kim and Gyowook Shin. They made me always think about the qualities I should have as a researcher and helped me with a lot of things.

I am always sincerely grateful to my parents and older brother. My parents always encouraged me and treated me with unconditional love. The encouragement, support, and love I received from my parents would not be enough to give back for the rest of my life. My older brother took care of my parents during my degree, and I am grateful for his wise advice when I needed to make choices.

I am truly grateful to my spouse, Yeonhee Lim. She always gave support and encouragement to help me focus on my degree. Thank her for understanding and loving me for who I am, and I apologize for giving her a hard life.

For Guzzi, my pet. I am sorry for not taking better care and thank her for always being healthy and welcoming to me. I look forward to the future with Guzzi and Yeonhee Lim.

Finally, I am grateful to myself for having lived a worthwhile and challenging life in the time that has passed. As I have done in the past, I will never forget the value of the given life to me, and I will wisely overcome the hardships and adversity that will come.

Table of Contents

List of Tables

List of Figures

Chapter 1 Introduction

1.1 Motivations

Smart manufacturing is an industrial revolution that starts with automating individual production equipment. Manufacturing processes are connected to each other through the introduction of manipulation and transportation systems in which intermediate parts from each production equipment are transferred to the next process. Controlling quality with automated handling and conveying systems for production, as well as quality inspection systems, reduces errors made by human operators and increases productivity. From a few related processes to the entire production process, automated production becomes possible based on the data which was previously designed. In addition, the introduction of cyber-physical systems enables efficient deployment of production equipment, and simulations can be used to identify potential problems in advance. This allows for flexible production management and the protection of workers from hazardous environments by enabling proactive actions rather than reactive actions in response to accidents. The smart manufacturing environment that includes all these processes is referred to as "Industry 4.0" [1]–[8]. Many industries, including automobiles [9], semiconductors [10], pharmaceuticals [11], medical and healthcare [12], foods [13], and aerospace [14], are adopting smart manufacturing environments to increase productivity. In the 2020s, the concept of "Industry 5.0" [15]–[17] emerged, emphasizing human dominance in manufacturing and focusing on the safe collaboration between robots and humans.

The garment manufacturing industry, which is highly labor-intensive with low automation, is also conducting research on adopting smart manufacturing environments [18]–[21]. Studies on augmented reality (AR) have been conducted to customize clothing for each customer [22]–[25]. Studies have been conducted to automatically generate designed fabric, called patterns, that make up clothes by AR or 3D measurements [26]–[29]. Studies have been conducted from inspecting fabric quality with the naked eye to automatically inspecting by applying computer vision and image processing algorithms [30]–[33]. With the recent advancement of graphic computing devices and deep learning research [34], [35] using them. It is possible to segment meaningful parts from an image and use them to evaluate not only the quality of the fabric but also the result after sewing [36], [37].

Automated clothing design and quality control have become possible, but automated sewing, the key to smart garment manufacturing, is lagging. A majority part of making clothes is sewing patterns together [38]–[41], which needs to be addressed for automated production. While there are machines that can take a trajectory and sew automatically along the path, there is a lack of research on algorithms that can recognize a seam line and generate a path based on it. Controlling the environment in the actual production area is difficult. This makes it even more difficult to recognize the seam line. Therefore, it is necessary to develop a vision environment to detect the seam line and image processing algorithms that are insensitive to external conditions. The vision environment is not only used to detect the seam line but also to monitor the sewing process and evaluate the quality of work after sewing.

Full automation of the individual sewing process is the basis of smart garment manufacturing. For achieving a higher level of

automation, grippers are required to connect the processes by handling the pattern. Lots of principles, including tendon-driven [42]–[44], fluidics [45]–[48], particle jamming [49], and vacuum suction [50], [51], are applied to the grippers and show an ability to handle the objects. However, due to the complex properties of the fabric itself [52]–[54], and the interaction between the gripper and the fabric, it is difficult to handle the fabric properly. Multi-actuation of the gripper is required for flexible usage in actual garment production. Additionally, the grippers are mounted to the robotic system, which requires multi-functionalities, including adaptive contact with the fabric, structural stability, and sensing capabilities for automation.

The gripper allows for interacting and handling the fabric, but a manipulator is required to move the gripper. Conventional rigid body-based manipulators allow for precise and fast motion but are unsafe for human interaction. This does not fit the human-centric Industry 5.0 manufacturing environment, where safe human-robot interaction is key. For safe interaction with humans while performing various actions, studies have been conducted on manipulators with high degrees of freedom and innate safety from a collision [55]–[61]. To estimate and control the pose of these manipulators, stereo vision or motion capture systems are used [62]–[66]. These vision systems require a chroma key or a controlled environment, which makes it difficult for manipulators to coexist with humans. In addition, the lack of sensing capabilities for interaction in the manipulators makes collaboration difficult. Therefore, the soft manipulator requires estimating and controlling the pose in a real-world environment and an interface for human interaction.

This research introduces the development of an automated sewing system enabled by machine vision for achieving a basic level of smart

garment manufacturing. I developed a sequence of image-processing algorithms, including segmenting the ROI as a preprocessor, detecting the seam line, and generating a top stitch path for automated sewing. Furthermore, I developed a soft gripper for the delicate handling of an unstructured and highly flexible fabric showing pinching and suction actuation in a single structure. In addition, I proposed a soft modularized robotic arm with a proprioceptive receptor for robotic manipulation of the proposed gripper and safe human-robot interaction.

1.2 Contributions

The main contribution of the thesis is to develop components for constructing smart garment manufacturing environments.

Specific contributions are included under the titles:

- **Automated Sewing System Enabled by Machine Vision for Smart Garment Manufacturing:** I proposed a machine vision-integrated automated sewing system that automatically segments the target region, detects the seam line corresponding region, and sews along the line without human intervention. The vision system and the developed algorithms can be used in a real production environment, where a pattern fixture called an acrylic template and the sewing machine are connected to each other. A transfer-learned model segments the sewing workspace regardless of the template's position, the color of the patterns, and the exposure time of the camera. By adjusting only two parameters, seam line detection and generating a secondary sewing path are possible regardless of unwound thread or dust. In addition to the algorithms, I developed a custom-built sewing machine that can be controlled externally. The developed machine is integrated with a vision

system using Robot Operating System (ROS) environment, can be controlled via serial communication, and operates like a conventional sewing machine. The performance of the developed automated sewing system was demonstrated.

- **Delicate Fabric Handling Using a Soft Robotic Gripper With Embedded Microneedles:** The proposed gripper could grip a fabric with various air permeabilities by structural deformative frictional pinching of fingers. Gripping was possible from some of the non-air-permeable coated fabric to the air-permeable porous fabric with the proposed gripper. The gripper had a small form factor and could be quickly actuated by vacuum pressure. The embedded microneedles penetrated and engaged the fabric without damage, preventing slippage between the fabric and the gripper when pinching. With the developed gripper, single-sheet separation from a stack was possible. In addition, the estimation of the number of gripped sheets was possible by measuring capacitance between electrodes attached to the gripper's fingers. Various robotic applications were demonstrated to show the possibilities of fabric handling and transferring fabrics.
- **Multi-Functional Soft Gripper with Microneedles and Integrated Sensing for Robotic Fabric Handling:** I proposed a gripper that allows multi-actuation in a single structure and has a multi-functional structure for automation and robotic handling of the fabric. The developed gripper had two independent actuation modes, pinching and vacuum suction, and could be used flexibly depending on the air permeability of the fabric. The multi-functional structure connected to the actuation part of the gripper compensated for the non-ideal non-zero angle of attack and distributed excessive load on the fingertip due to the compliance

of the structure. In addition, a pneumatic pressure sensor connected to the compliant structure was able to measure the pressure as the volume changed, which was used to determine contact and control the contact force. Fabric handling and automation were demonstrated by robotic manipulation systems.

- **Soft Modularized Robotic Arm for Safe Human-Robot Interaction Based on Visual and Proprioceptive Feedback:** I proposed a soft modularized robotic arm for performing dexterous manipulation and safe interaction with humans. I designed a complex bellow with an embedded channel on the surface. The bellows were 3D-printed, simplifying the previous fabrication process, like molding. The bellows were treated for surface activation, and organogel was embedded in the channel for triboelectric nanogenerator (TENG) effect, which allowed the bellows to respond to human touch. I developed a manipulator module with the bellows, a pneumatic control system (e.g., solenoid valves, ejectors), and a customized controller and assembled them to form the soft robotic arm. I proposed a deep learning model and algorithm to control the manipulator module with vision without strict environmental control and developed an omnidirectional soft string strain sensor to control the module to use in an occlusion environment. A conventional gripper was mounted to demonstrate performing a task by human touch, and an application was demonstrated that handles the fabric using the previously developed soft gripper.

1.3 Thesis Outline

The thesis is organized into the following four chapters.

Chapter 2 introduces an automated sewing system. A deep learning model for segmenting a region of interest containing a seam line and algorithms for detecting the seam line from the segmented region and generating a secondary sewing path are introduced. The system configuration and connections are introduced, and a robotic application of the automated sewing system is demonstrated.

Chapter 3 introduces a soft robotic gripper as the first part. The design and the analysis of the gripper structure are introduced first. Second, the operation procedure and the fabrication procedure are presented. Third, experimental characteristics of the gripper are presented. Lastly, robotic system applications using the proposed gripper are demonstrated.

The second part of Chapter 3 introduces a multi-functional soft robotic gripper. First, the design and the concept of multi-actuation in a single structure. Second, the design and the analysis of a multi-functional structure for automation. Lastly, the experimental characteristics and robotic applications are demonstrated.

Chapter 4 introduces a soft modularized robotic arm. First, the design of the bellow actuator and the components of the manipulator module are presented. Second, the fabrication process of the tribo-sensitive bellow and an omnidirectional soft string strain sensor are presented. Third, simulations and experimental results of controlling the modules are presented. Lastly, robotic applications of collaboration with a human and handling the fabric are demonstrated.

Finally, Chapter 5 concludes the thesis by summarizing the contributions of the research and discussing future work.

2. Automated Sewing System Enabled by Machine Vision for Smart Garment Manufacturing

2.1 Background

Smart manufacturing refers to the advancement of technology through the integration of networks, robotics, sensors, artificial intelligence (AI), and the Internet of Things (IoT) [3], [67], enabling autonomous production driven by data. This involves transforming qualitative information, including consumer preferences and requirements, into digitized data that can be used to design and produce the personalized product for individual customers. Based on this digitized design, robots perform automated production and support human operators while monitoring the whole process using sensors and computer vision, assessing output quality, and supervising each process. To achieve the adaptability required for smart manufacturing, machines must be systematically interconnected through data, allowing for seamless and efficient operations.

Many industries, such as automotive, pharmaceutical, and semiconductor, have adopted smart manufacturing environments [68]–[70]. The garment industry, which is notably labor-intensive, has recently begun adopting automated systems equipped with advanced production tools and sensing technologies [71]–[73]. In the garment industry, smart manufacturing begins on social commerce platforms, where consumers select and virtually try on clothing using augmented

reality (AR). Sewing patterns, basic fabric components that form the final clothing pieces, are designed and prepared based on each consumer's fitting data measured through AR technology in virtual environments. By assembling these patterns, customized clothes are produced.

The implementation of smart manufacturing in the garment industry relies on computer vision for not only guiding and monitoring operations but also inspecting the quality of both intermediate parts and final products. Specifically, computer vision is employed to identify shapes, sizes, and positions of patterns accurately [73], generate sewing trajectories [71], [74], supervise sewing and assembly processes [4], [75], and evaluate results [37], [76], [77]. Thus, computer vision is crucial for systematically connecting and automating multiple processes seamlessly.

Generating sewing paths, a key task for automated production, is greatly aided by computer vision. However, due to technical challenges, its application has been restricted to generating paths for simple overlapped patterns [71], patches, and logos [74] using simple edge detection algorithms. The main processes for clothing production involve stitching two distinct patterns. For example, a basic T-shirt comprises a collar, cuffs, back and front bodies, and left and right sleeve patterns, which are initially stitched for connection and tightly secured by top stitching (Fig. 2. 1-(a) and 2. 1-(b)) [78], [79]. Although the first stitch (i.e., basting stitch) can be easily sewn along the marked profile on the two overlapped patterns, the second stitch (i.e., top stitch) must be sewn along the seam line, which is made by flipping the overlapped upper pattern and separating it from the lower pattern. The top stitch must maintain a predetermined distance from the seam line. Generally, since the two patterns share the same color,

distinguishing the seam line using traditional computer vision methods is challenging. Additionally, environmental factors such as uncontrolled lighting, dust, or irregular substances on the patterns complicate seam line detection and post-processing. As a result, seam line detection and path generation for topstitching are the obstacles to applying computer vision to automate garment manufacturing.

Since manual sewing is common in traditional garment factories, the resulting quality may vary based on the operator's skill level [80]. To automate the sewing process, a pattern former, an automatic sewing machine with a motorized stage, has been used (Fig. 2. 1-(c)) [81]. Suitable for stitching planar and large-area patterns in general, the pattern former consists of a sewing unit and an x-y stage, automatically sewing the pattern according to the trajectory which operators input. A template comprising two thin acrylic plates is used to secure and hold the overlapped target fabric layers (Fig. 2. 1-(d)). This template has a window that exposes the seam line and the sewing area. Despite their automatic capabilities, commercially available pattern formers have proprietary path-generation software and interfaces provided by manufacturers, complicating use in an autonomous and seamless production. Even when a sewing path is automatically generated, human intervention remains necessary due to the lack of autonomous pattern recognition capabilities.

Studies for vision-based automated garment production have been conducted and applied to patches, logos, underwear [71], [73], [82]. However, those are limited to detecting and only giving an offset from the edges of the pattern, and seam line-based top stitch automation has not been studied. Based on machine vision and deep learning, studies have been conducted to recognize these seam line and connectivity of sewn threads or puckering can be evaluated [83]–[87].

These studies have been limited to the evaluation of outputs from sewing and have not been applied to automated production based on the detected seam line.

In this research, I propose an automated sewing system that incorporates machine vision and image processing algorithms to detect the seam line and generate corresponding top stitch paths. Additionally, I present an instance segmentation model that infers the template window from the captured image for algorithm preprocessing. This area is detected by the proposed instance segmentation model, which employs transfer learning [88] from a segmentation model known as YOLOv5 [89]. Based on the segmented template window, the seam line is detected, and the top stitch path, at a predetermined distance from the seam line, is generated using the proposed algorithms. The top stitch path is successfully generated by the proposed smoothing algorithm, insensitive to dirt on the pattern or changes in illumination. Furthermore, I develop a programmable sewing machine that automatically executes the top stitching process along the generated sewing path using the integrated vision system, without any input or intervention from human operators. By incorporating an additional inspection process after stitching, the quality of the stitched path can be assessed, and the resulting data can be generated for monitoring within the proposed system.

In the following section, I first discuss the implemented algorithm of segmenting the region of interest, followed by seam line detection and top stitch path generation. After that, I introduce a mechanical sewing system with its communication configuration. I then evaluate the performance of the proposed algorithms: segmentation of a trained deep learning model, seam line detection, top stitch path generation, and insensitivity to noise and dirt. In addition, I evaluate the

performance of the developed sewing machine: spatial resolution in x and y directions, maximum speed, and stitching intervals. With these features of the automated sewing machine, I demonstrate applications for automating top stitching patterns. I finally conclude my research with discussions of the contributions and future work.

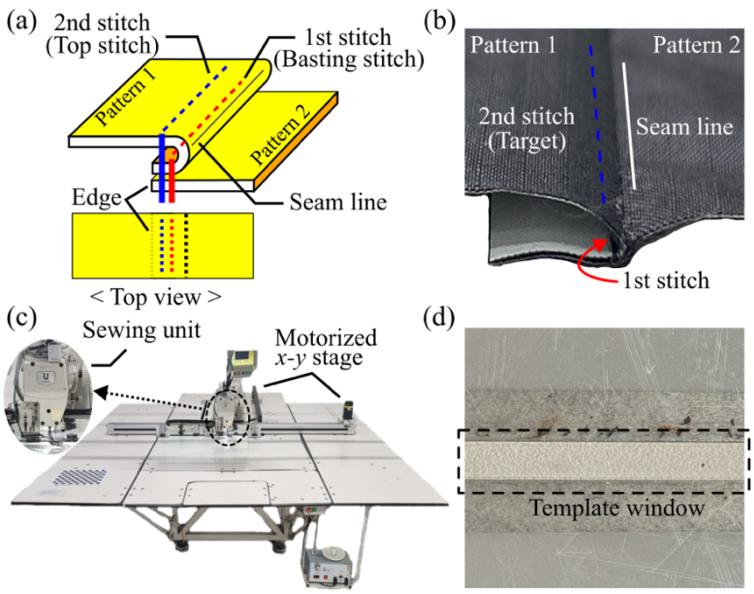

Fig. 2. 1. (a) Description of stitching and (b) its actual image. (c) Main components of an automated sewing machine. (d) Acrylic template used to secure the fabrics and exposed window for sewing.

2.2 Algorithms

2.2.1 Instance segmentation based on YOLOv5

I utilize the YOLOv5 model to identify the template window, which

involves the seam line within an image. By employing instance segmentation rather than object detection, which solely discovers a bounding box surrounding the template window, it becomes possible to infer the area occupied by the target in the image. As the image is captured in a controlled environment, segmentation accuracy is anticipated to be high. Consequently, I apply a one-stage detector [90], [91] instead of a two-stage detector [92], [93] to minimize inference time. The YOLOv5 instance segmentation model's architecture consists of three components: a backbone, a neck, and a head, as depicted in Fig. 2. 2. Within the backbone, features are extracted from the input image via convolution and subsampling (Fig. 2. 2-(a)). In the neck, each output from the backbone is input for the layer with the corresponding resolution, and features are mixed through upsampling (Fig. 2. 2-(b)). In the head, masks and classes are predicted at each image scale (Fig. 2. 2-(c)), and the results are combined into a singular image.

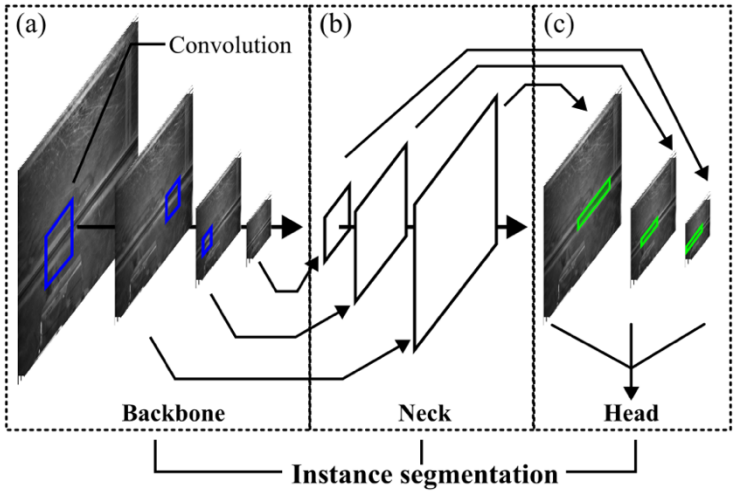

Fig. 2. 2. Simplified architecture of YOLOv5. (a) Backbone for extracting features. (b) Neck for mixing features. (c) Head for inference of bounding boxes, masks, and class prediction.

For fine-tuning the YOLOv5 model, 69 images containing the template window are captured using a vision environment (Fig. 2. 3). Six images are allocated to the validation dataset, another six images are assigned for the test dataset, and the remaining images are assigned to the training dataset. The experimental setup is composed of a monochromatic camera (BFSU3-123S6M-C, FLIR) and illuminations (EuroBrite™ Bar Lights, Advanced Illumination). The image dimensions are 4,096 × 3,000 pixels, and the developed system exhibits a resolution of 68 μm per pixel.

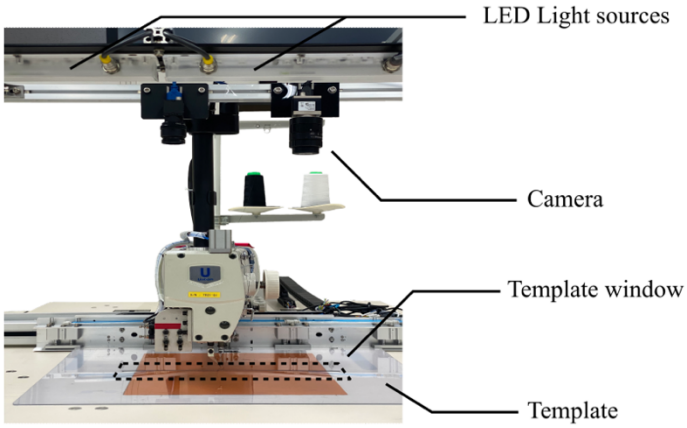

Fig. 2. 3. Vision setup for taking images of templates.

Three fabric types with colors of black, orange, and blue are used for training, and each fabric has a unique weaving pattern and a seam line (Fig. 2. 4-(a), 2. 4-(b), and 2. 4-(c)). Since the camera captures the light reflected from the fabric, captured intensities vary depending on the fabric's color. Consequently, I select fabrics ranging from dark to bright colors. Furthermore, images are captured while modifying the exposure time from 10,000 μsec. to 100,000 μsec. to facilitate detection under diverse illumination conditions.

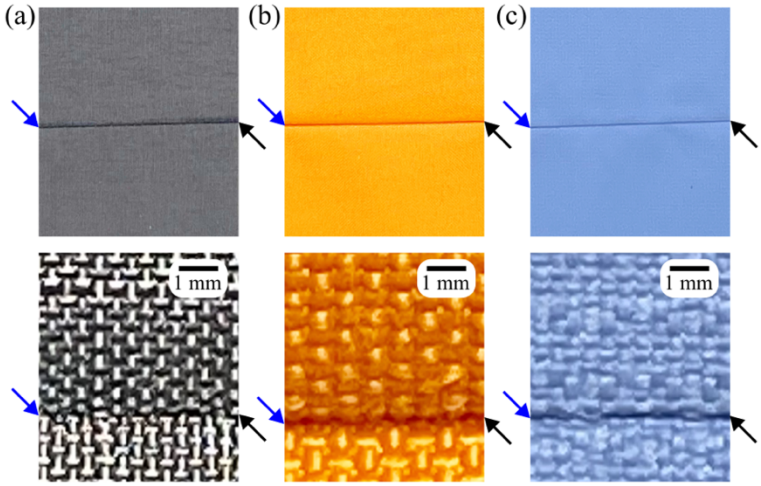

Fig. 2. 4. Fabrics used in experiments. (a) Black, (b) orange, and (c) blue colored fabric, and their magnified images near the seam line. Blue and black arrows indicate the start and the end points of the seam line, respectively.

Prior to training the model, I conduct a series of image preprocessing steps (Fig. 2. 5-(a)). Given the large input image dimension, which is not suitable for model training, the image is resized to 1,000 × 750 while preserving the aspect ratio (Fig. 2. 5-(a)-i). Then, a contrast-limited adaptive histogram equalization (CLAHE) [94] is applied to the image. The CLAHE divides the image into a grid of tiles, establishes a limit on pixel intensity, redistributes values exceeding the limit, and equalizes the grid's histogram. Since the installed light sources do not cover the entire template area, intensity gradation appears along the window's length in the image. Therefore, the CLAHE is employed to decrease brightness differences between the image's center and edge, followed by the application of a Gaussian blur to reduce sharpness (Fig. 2. 5-(a)-ii). In the image, the template window takes up 150 pixels in height, which is relatively

small compared to the total height of 3,000 pixels. Thus, 4 × 4 tiling is applied to magnify minor features (Fig. 2. 5-(a)-iii). The image is divided into 16 tiles, each area resized to 1,000 × 750 pixels and added to the dataset. Data augmentation is applied to add variance to the image dataset, such as rotation for detecting the template window at various orientations, mosaic for small feature detection, and image cropping to alter the size and position of the template window. The YOLOv5 model is fine-tuned using the processed images and a GPU (A100-SXM4-40GB, NVIDIA). Conversely, during inference, only CLAHE and Gaussian blur are applied to the input image to predict the template window.

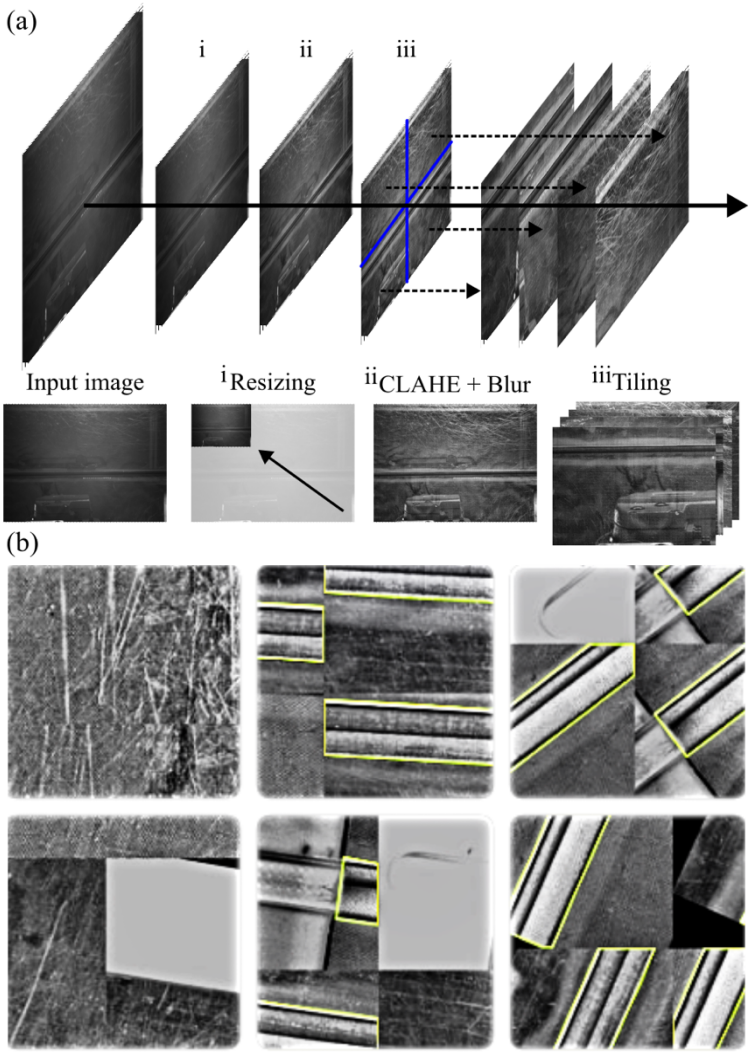

Fig. 2. 5. (a) Procedures of preprocessing. i. Resizing. ii. Applying contrast-limited adaptive histogram equalization and Gaussian blur. iii. Tiling. (b) Augmented images after preprocessing. Yellow boxes are the target (template window).

2.2.2 Seam line detection and path generation

The seam line is identified based on the difference in the amount of light reflected by the fabric under the illuminations (Fig. 2. 6-(a)). Light sources are positioned asymmetrically to the camera to amplify

the difference in reflected light. p_1 represents the curved portion of the folded upper pattern, which flattens as it moves away from the seam line. p_2 and p_3 denote the seam line and the flat section of the bottom pattern, respectively. Ideally, incident light on the seam line shows minimal reflection. Consequently, pixel intensity reaches a local minimum at this point (p_2) (Fig. 2. 6-(b)-i, 2. 6-(b)-ii, and 2. 6-(b)-iii). Since the light source does not cover the entire template area, the average pixel intensity varies according to the value of d, representing the pixel distance from the light source's center. Nevertheless, regardless of the value of d, the local minimum intensity within the template window is derived from the pixel position p, in proximity to the seam line, excluding both boundaries.

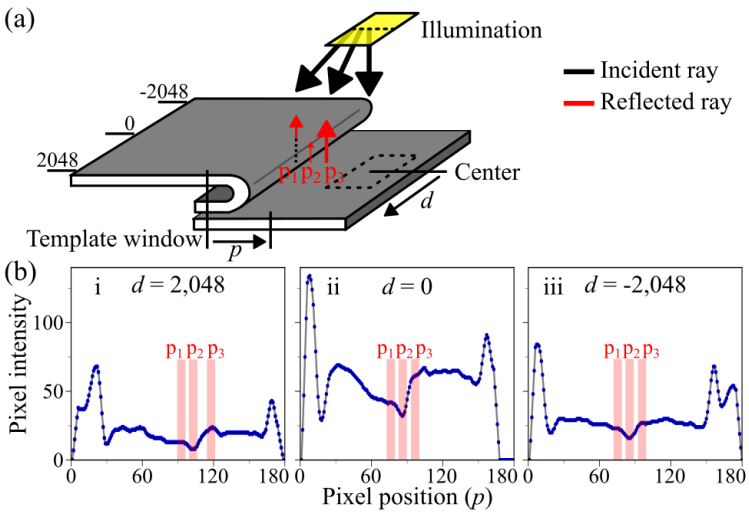

Fig. 2. 6. Schematic of seam line detection principle and pixel intensity plots in different d and p locations.

I propose image processing algorithms for seam line detection based on the following assumptions: i. Within the detected template window, each column of the image array has a single seam line point. ii. The seam line points of adjacent columns are in similar locations. iii.

The seam line point in each column has the minimum intensity. Using these assumptions, seam line detection is achievable using only pixel intensities without implementing additional image processing techniques (e.g., thresholding, edge detection) and is possible irrespective of the illumination conditions. An algorithm to identify points of interest (e.g., p_1, p_2, and p_3) with the local minimum intensity within the template window is initially developed, as depicted in Algorithm 2. 1.

Algorithm 2. 1 Suggest possible seam line points

Input: width of detected template window w, adjacent pixel distance adj_d, i-th column of template window array C_i, number of seam line points g, rejected group of index R, temporary array A

Output: seam line candidates L

Initialization: $adj_d \leftarrow 3$, $g \leftarrow 5$

```
for i = 0 to w do
    j = 0, array A
    while A length ≠ g do
        index of j-th minimum intensity in C_i k_j, j ← j + 1
        if C_i[k_j − 1] = 0 or C_i[k_j + 1] = 0 then
            append k_j to R
        else
            for u = 1 to adj_d do
                if k_j + u ∈ R or k_j − u ∈ R then
                    append k_j to R
                else
                    append k_j to A and R
                end if
            end for
```

```
        end if
    end while
    append A to L
end for
return L
```

This algorithm determines g indexes of pixels with the minimum intensity in all columns encompassed by the detected template window. Ideally, the index with the minimum intensity in the template window is assumed to be the seam line, but I discover g $(g = 5)$ candidates for the seam line points. At the template window boundaries, pixel intensities equal zero. Since these values are not of interest, they are excluded from the seam line point candidates, and all the indexes connected to these indexes are also excluded. Furthermore, if the identified index is within the adjacent distance, adj_d $(adj_d = 3)$, this index is excluded from the seam line point as it is considered connected. By adjusting only two parameters, candidates for the seam line points in the image can be identified.

Algorithm 2. 2 Determine seam line

Input: width of detected template window w, number of seam line points g, seam line candidates L, j-th seam line candidate SL_j, j-th group connectivity score s_j, j-th group minimum pixel difference $\min_j$, k-th pixel index difference Δp_k, $(i-1)$-th pixel index in SL_j $p_{i-1}[j]$, j-th group seam line index p_j

Output: u-th seam line SL_u

Initialization: $g \leftarrow 5$, $SL_j[0] \leftarrow SL_j[i-1]$

```
for i = 1 to w do
```

```
    for j = 0 to g do
        min_j ← 9999, p_{i-1}[j] ← SL_j[i − 1]
        for k = 0 to g do
            Δp_k = abs(L[i][k] − p_{i-1}[j])
            if Δp_k < min_j then
                min_j ← Δp_k, p_j ← L[i][k]
            end if
        end for
        append p_j to SL_j, s_j ← s_j + min_j
    end for
end for
u ← argmin(s_1, s_2, ..., s_g)
return SL_u
```

From the suggested seam line points L, the actual seam line points are determined based on the connectivity between adjacent columns (Algorithm 2. 2). Since the seam line generated by folding the upper pattern is a smooth curve, the actual seam line among the candidates has the minimum sum of the change in pixel position.

The top stitch path is generated from the identified seam line SL_u. Before generating the path, the established seam line is smoothed because the seam line does not have a smooth curve due to noise caused by dust or substances on the patterns, even if connectivity is minimized. Consequently, I divide the template window into n intervals, smooth each interval, and merge them. Rather than applying a moving average significantly influenced by outliers, I employ a Savitzky-Golay smoothing filter ($\hat{y}$) [95], a finite impulse response system analysis method, as an alternative to time-consuming local regression. After

smoothing the seam line, the point p_j of the path TS is generated and merged, using the distance per pixel r of the vision system and the predetermined gap for the top stitch d_g. d_g is set as 1.6 mm, the smallest gap required for precise clothing production (Algorithm 2. 3).

Algorithm 2. 3 Smoothing and generating top stitch path

Input: width of detected template window w, seam line SL, smoothing window size m, number of window n, smoothed seam line point $\hat{y}$, temporary array A, resolution of vision system r, j-th top stitch point ts_j, predetermined gap d_g

Output: top stitch path TS

Initialization: $m \leftarrow 300$

interval $n = integer(w/m)$
for $i = 0$ to n **do**
    $A = SL[i * m : (i + 1) * m]$
    apply Savitzky-Golay filter to A, result $\hat{y}$
    for $j = 0$ to m **do**
        $ts_j = \hat{y}[j] + d_g/r$ and append p_j to TS
    end for
end for
return TS

2.3 System

An automated sewing system consists of a vision system and a custom-built sewing machine. As outlined in Section 2.2.1, the vision system has a camera and light sources for detecting the seam line of

the patterns. This section introduces the sewing machine's details, including its hardware specifications. Additionally, the communication methods between the system components and operational sequences are presented.

2.3.1 Automatic sewing machine

To automatically sew along the generated top stitch path, I develop an automatic sewing machine based on a commercial pattern former (UAS-H700-D, UNICORN). The operational unit of the developed machine consists of three motors: two servo motors (SGM7J-04AFA21, SGM7J-08AFA21, YASKAWA) attached to the x-y stage to control the template's position, and one servo motor (SGM7J08AFA21, YASKAWA) that manages the sewing needle's position and trims the thread. By connecting the motor controllers and an external PC, it becomes possible to control the motors' position and speed without utilizing the factory-installed program. The sewing machine also includes four pneumatic-guided cylinders that stabilize the template from vibrations and a presser foot that flattens the patterns during sewing (Fig. 2. 7).

The maximum travel distance of the stage is 1,230 mm in the x direction, parallel to the template window's long side, and 720 mm in the y direction. The spatial resolution of the x-y stage is 10 μm in both directions. The sewing needle motor's maximum RPM is 600. The average speed for linear translation is proportional to the sewing needle motor's RPM and the sewing interval. The x-y stage has a maximum translation speed of 60 mm/s when the RPM is 600 and the sewing interval is 5 mm.

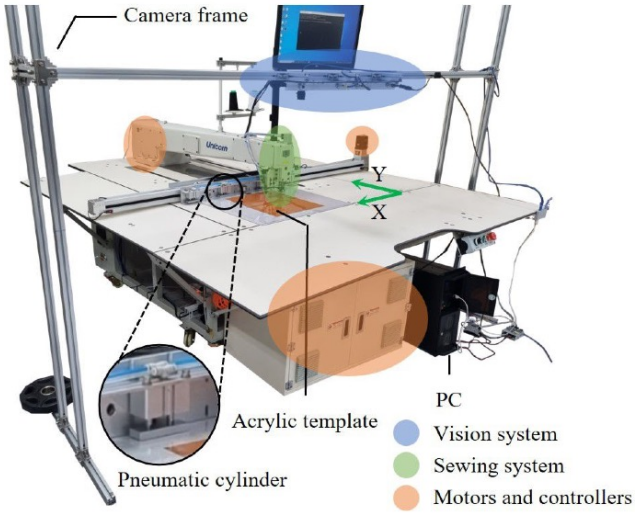

Fig. 2. 7. Components of automated sewing machine.

2.3.2 Communication

The entire system can be categorized into three sub-systems: the sewing machine, the camera, and the lighting. To enable seamless communication between these sub-systems, I utilize the Robot Operating System (ROS) with TCP/IP communication [96]. Within the ROS, each sub-system is represented as a node, and communication is established through messages in ROS topics. The system is composed of four nodes: the sewing machine node, the vision node, the light node, and the graphical user interface (GUI) node (Fig. 2. 8). The sewing machine node controls the x-y stage motors and monitors the motor encoder values. The vision node captures images through the camera and executes the proposed algorithm. The light node manages the state of the LED light sources, and the operator can monitor and control the top stitching process via the GUI node.

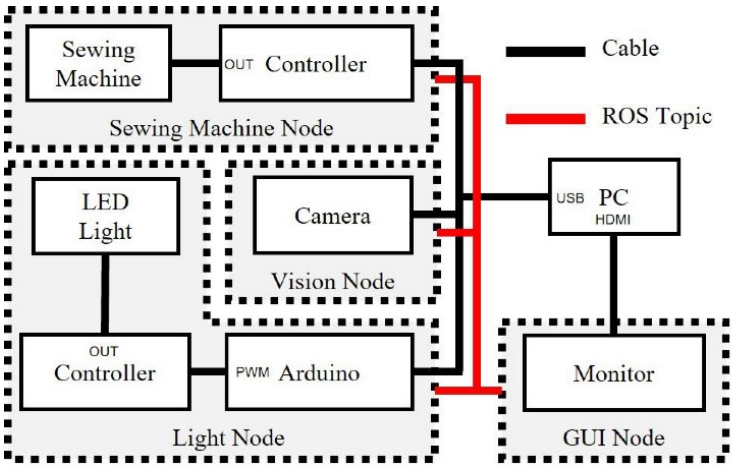

Fig. 2. 8. Schematic diagram of communication in the automated sewing system.

2.4 Experiments and results

I conduct experiments to evaluate the performance of the trained segmentation model, the seam line detection and top stitch path generation using the proposed algorithm, and the sewing machine and stitching quality.

2.4.1 Instance segmentation

For evaluating the trained model, the black (Fig. 2. 9-(a) and 2. 9-(b)) and blue (Fig. 2. 9-(c) and 2. 9-(d)) fabrics are used because the amount of reflected light varies with colors. Additionally, dark and bright images are obtained by using two different camera exposure times. Then, the CLAHE and Gaussian blur are applied to the captured images, which are provided to the trained model as inputs (Fig. 2. 9-ii). The segmentation takes approximately 0.3 seconds when using a GPU (Geforce 3080 TI, NVIDIA). The trained model detects the

template window regardless of the optical noise reflected on the glossy acrylic template, the fabric's color and unique weaving pattern, and the illuminations' brightness.

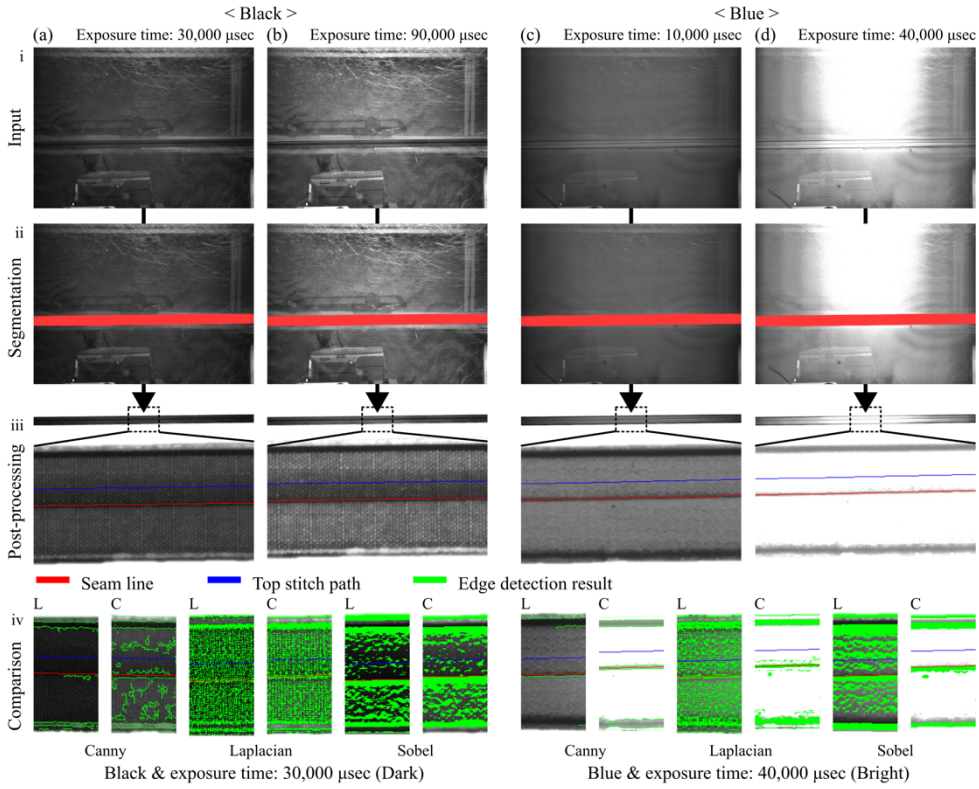

Fig. 2. 9. Sequence and result of seam line detection and top stitch path generation. Black fabric with exposure time of (a) 30,000 and (b) 90,000 μsec., and blue fabric with exposure time of (c) 10,000 and (d) 40,000 μsec. The sequence consists of i. input and preprocessing, ii. segmentation of template window, iii. post-processing: masking the template window, smoothing, and top stitch path generation. iv. Comparison with conventional edge detection algorithms. L and C represent left-end and center of the image, respectively.

2.4.2 Seam line detection and top stitch path generation

I conduct an experiment to determine whether the seam line is detected, and the top stitch path is appropriately generated through the proposed algorithm, comparing the result with the outcome from conventional edge detection algorithms. Using the segmented area as a mask, only the template window is isolated from the image and becomes the region of interest (ROI). By setting the ROI, seam line detection and post-processing are simplified. The result of applying the seam line detection algorithm and the generated top stitch path can be seen in Fig. 2. 9-iii. I compare the result with that of conventional edge detection algorithms. Canny [97] edge detector, Laplacian [98], and Sobel [99] operators are applied to the ROI of both the dark black (exposure time 30,000 μsec.) and the bright blue (exposure time 40,000 μsec.) patterns (Fig. 2. 9-iv). In the dark black pattern, the seam line is not found by the Canny edge detector and Laplacian operators. In the case of the Sobel operator, as expressed in green, the red seam line found by the proposed algorithm overlaps the green area. For the bright blue pattern, the result of the detected seam line by the proposed algorithm is similar to those of the edge detection algorithms. All the conventional algorithms are affected by the image's brightness and require complex image processing before and after applying the algorithms to detect the seam line.

The proposed detection algorithm is possible to detect the seam line on the embossed fabric (Fig. 2. 10-(a)), the curved-shaped seam line on the fabric with horizontal stripes (Fig. 2. 10-(b)), and diagonal-shaped seam line (Fig. 2. 10-(c) and 2. 10-(d)).

To quantitatively evaluate the performance of the proposed

detection algorithm, a piece of white paper is inserted into the gaps between the patterns (Fig. 2. 10-(e)). Since the white color is highly reflective, it has high pixel intensities when photographed, making it easier to find the ground truth with contrast near the seam line (Fig. 2. 10-(f)). Image processing is used to find the seam line boundaries (Fig. 2. 10-(g)). I find the ground truth for the black, the blue, and the orange-colored patterns and compare it with the result of applying the proposed algorithm. The average position errors for the black, the blue, and the orange-colored patterns are 0.05, 0.05, and 0.09 mm, respectively, with the standard deviations of 0.04, 0.04, and 0.09 mm.

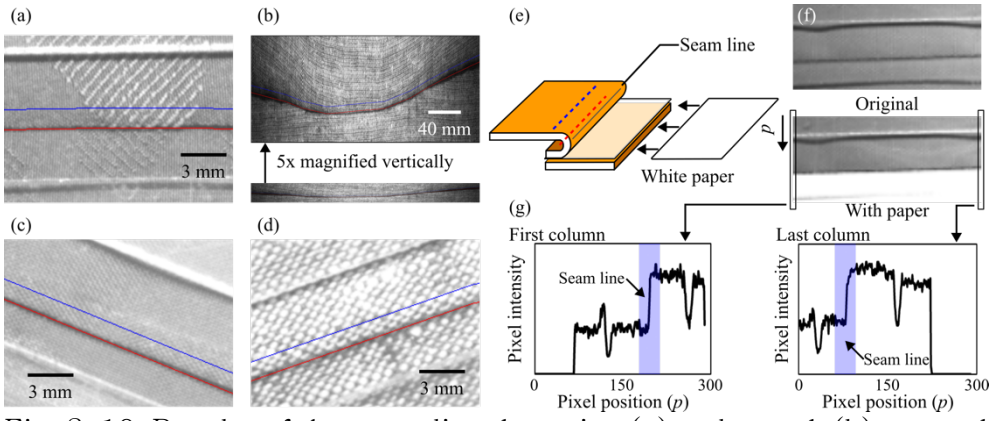

Fig. 2. 10. Results of the seam line detection (a) embossed, (b) weaved pattern and curved, (c) and (d) diagonal. (e) White paper insertion for quantifying performance. (f) Photos of with and without paper. (g) Intensity plots of reflected light for the first and the last column, respectively.

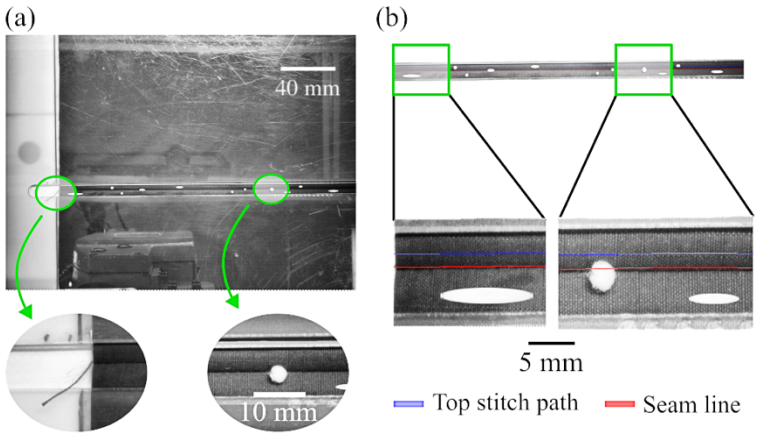

Fig. 2. 11. Robustness test for the proposed algorithm. (a) A single strand of the edge thread is unwound (Left) and a large dirt is place on the seam line (Right) within the template window. (b) Result of segmentation, seam line detection, and top stitch path generation.

I evaluate the robustness of the segmentation model and the proposed algorithm for seam line detection (Fig. 2. 11-(a)). An unwound thread at the pattern's edge makes the starting point for sewing inconsistent, and the dirt on the seam line makes the top stitch path jagged. The unwound thread is rejected by the trained segmentation model, and the generated top stitch path is smooth with the proposed algorithm, even in the presence of dirt on the seam line (Fig. 2. 11-(b)). The experimental results demonstrate that the developed sewing machine plays a crucial role in the pattern former, while precisely operating with the sewing path generated by the vision system.

2.4.3 Top stitching with automated sewing machine

I conduct an experiment to assess the performance of the custom-

built sewing machine in terms of spatial resolution, maximum translation velocity, and stitching interval. The sewing machine is controlled to move 1 mm in the x and the y directions by taking 100 steps in 10 μm increments, with the simultaneous measurement using an absolute encoder (Fig. 2. 12-(a) and 2. 12-(b)). The inset plots indicate that when the measured position of the x-y stage reaches the target position, the next goal position is given to the x-y stage. This sequence is repeated 100 times to move 1 mm in the x and the y directions. As a result of analyzing the images captured by the vision system before and after the operation, the pattern moves 1 mm in each axis and shows a spatial resolution of approximately 10 μm (Fig. 2. 12-(c) and 2. 12-(d)). Next, I test the maximum translation speed under stitching conditions. I make the stage move 100 mm in the x direction under the maximum RPM (600) of the sewing needle, and the result is shown in Fig. 2. 12-(e). The black and blue curves indicate the position on the x-axis and speed, respectively. The stage moves 100 mm for 1.67 sec., with an average speed of 60 mm/s.

Since the optimal stitching interval varies with the fabrics, this length must be adjusted by the operator. I sew the pattern by changing the stitching interval from 1 mm to 5 mm, and the results are captured with the vision system (Fig. 2. 12-(f)). The actual stitching interval is similar to the input value.

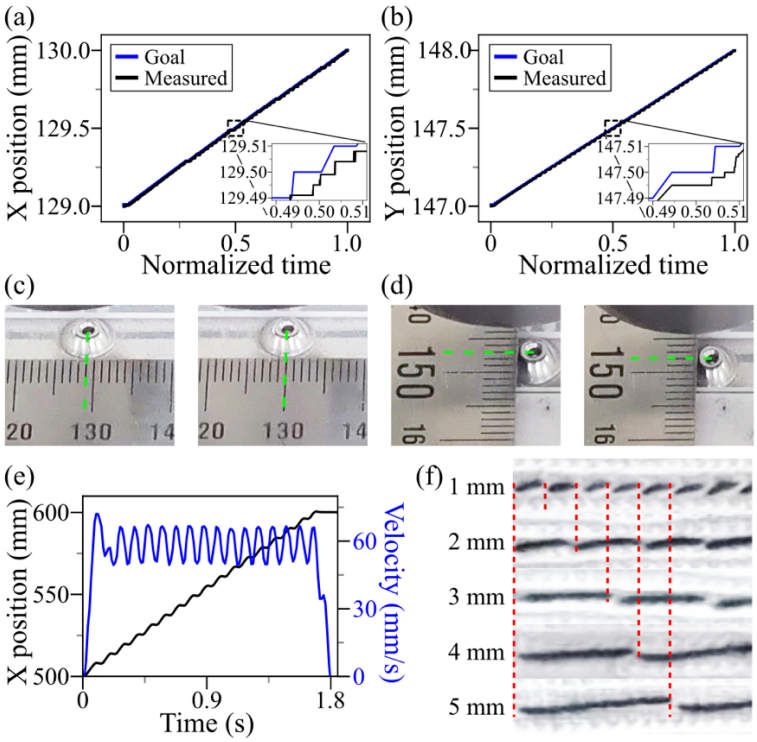

Fig. 2. 12. Automatic sewing machine basic performances. The goal and the current measured position by the absolute encoder in (a) x-axis and (b) y-axis and the corresponding visual result in (c) x-axis and (d) y-axis. (e) Position and velocity measurement in x-axis. (f) Sewing results with stitching intervals from 1 mm to 5 mm.

Furthermore, I sew the pattern along the top stitch path, which is generated by the proposed algorithm, and analyze the results. To evaluate the stitching quality of the developed sewing machine, first I detect a line marked on a single layer of fabric with the proposed algorithm and generate a top stitch path (Fig. 2. 13-(a) and 2. 13-(b)). Then, I sew along the generated path without providing an offset. After sewing, the image is captured with the vision system to evaluate whether the top stitching result matches the marked line. The result of the top stitching is shown in Fig. 2. 13-(c), and the magnified image demonstrates that the top stitching line followed the marked line.

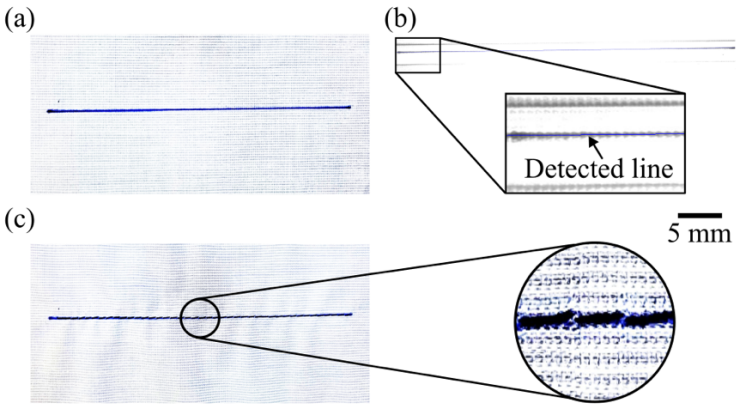

Fig. 2. 13. Top stitching result using the custom-built sewing machine. (a) Fabric with marked line. (b) Detection result. (c) Top stitching result. Magnified image shows the exact match of the top stitch line with the marked one.

2.5 Demonstration

I establish an automated sewing system by integrating the vision system with the sewing machine and connecting components through the ROS. The integrated system autonomously generates the top stitch path based on the captured template image and sews along the path without human operator intervention. I demonstrate automated stitching using the integrated system. First, each part of the pattern is captured (Fig. 2. 14-(a)), and the top stitch path is generated using the proposed algorithm. Image merging is required since patterns used to make clothes would be longer than a single capture. The top stitch path is generated 1.58 mm (1/16 inch) from the seam line in the merged image, and the custom-built machine sews along the path. 1.58 mm gap is the smallest distance between the seam line and the top stitch typically used in garment production [94], [95]. Images before and after sewing are shown in Fig. 2. 14-(b) and 2. 14-(c). In addition, the

curved seam line is able to be detected by the proposed algorithm (Fig. 2. 14-(d)) and top stitching along the generated curved path is possible (Fig. 2. 14-(e))

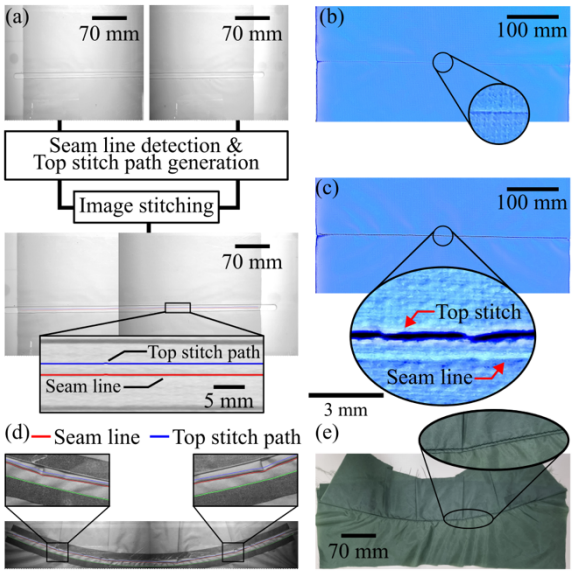

Fig. 2. 14. Automation procedure for stitching. (a) Left and right images of template (top) and stitched image with detected seam line and generated top stitch path (bottom). (b) Before and (c) after sewing. Magnified image shows the consistent distance (1.58 mm) between the top stitch and the seam line. (d) Detected curved seam line and (e) the result of the top stitching.

2.6 Discussion

I develop an automated sewing system by integrating a custom-built sewing device with a machine vision system, which does not require any human operator intervention or assistance. All components are systematically connected through the ROS. In the vision system, a trained deep learning model and the proposed algorithms are executed

sequentially. A template window is detected and segmented by the trained deep-learning model in the captured image, and the top stitch path is generated based on the seam line by the proposed algorithms. The custom-built sewing machine is controlled by an external PC and shows a spatial resolution of 10 μm, a maximum translation speed of 60 mm/s, and an adjustable stitching interval from 1 mm to 5 mm. Through this integrated system, automated pattern sewing, and simultaneous monitoring are possible. By repeating the process of capturing the image after top stitching, the quality of the stitched path is evaluated, and the resulting data are generated. The automation of the sewing machine, the quality assessment of the output through the vision system, and the generated data for use in subsequent processes will enable seamless production by significantly increasing the connectivity of multiple processes in garment manufacturing. Consequently, I expect my system to play a critical role in achieving a basic level of smart manufacturing in the future garment industry.

Chapter 3. Part I. A Microneedle-Assisted Soft Gripper for Delicate Robotic Manipulation of Fabric

3.1 Backgrounds

Industry 4.0 is a technological innovation in which advancements in robotics, artificial intelligence (AI), and the internet of things (IoT) facilitate automation and data exchanges in manufacturing, leading to the realization of "smart factories" or smart manufacturing [67]. The transformation of traditional manufacturing factories into smart factories is expected to result in increased productivity and efficiency as human labor is replaced by robots and machines through automation [100]. The garment industry significantly benefits from smart manufacturing [101] due to its labor-intensive and heavy reliance on human workers. However, a lack of automated robotic systems that can handle different types of fabrics with high precision and delicacy makes automation difficult. Even simple manipulation tasks, such as "pick and place," require dexterity when handling fabrics due to their thin and flexible properties and tendency not to return to their original shapes when deformed.

To enhance dexterity and adaptability, robotic grippers made of soft materials and structures have been developed. The mechanical compliance of these soft grippers allows them to deform and adapt

their shapes to objects with varying shapes. Actuation mechanisms for soft grippers include tendon-driven [43], [44], [102] and fluidic [45]–[48] actuators for flexion or extension motions, stiffness control by particle jamming [49], and simple vacuum suction [50], [51]. These mechanisms have successfully demonstrated the ability to pick up and manipulate objects with different shapes. However, fabrics are known for their complex morphological and mechanical properties and their nonlinear static and dynamic behaviors [52]–[54]. These characteristics make it challenging to perform even basic manipulation tasks in garment manufacturing, such as separating a single sheet of fabric from a stack using the soft gripper mechanisms. Consequently, I propose a soft robotic pinching gripper capable of delicately handling various types of fabrics, as illustrated in Fig. 3. 1.

Fabric-handling grippers were initially proposed in the early 1980s [103]. Since then, various gripping mechanisms, including pinching, vacuum suction, needles, and electroadhesion, have been studied [104].

Pinch grippers, equipped with two jaws, buckle fabric by pressing it between the jaws as they are brought together [105], [106]. Despite simple mechanism and cost efficiency, separating a single sheet from a stack by sliding it with pressure is difficult when dealing with multiple sheets of fabric with rough surfaces due to the high friction between the sheets.

Suction grippers use a simple mechanism of negative pressure [107]. However, most fabrics have a porous structure that does not create negative pressure and may not hold a single fabric, or may hold more than one piece of fabric at a time.

To address this issue, needle-based grippers have been proposed. These grippers can effectively hold porous objects, which are difficult

to grip using vacuum suction, using penetration and interlocking. Nevertheless, previously developed needle grippers [108], [109] are unsuitable for soft fabrics since they were designed for objects made from specific materials, such as sponges and rubber. Moreover, thick needles (over 700 μm in diameter) can sometimes leave permanent penetration marks on the objects.

Electroadhesion is an alternative gripping method that holds planar objects. It relies on the electrostatic effect between the gripper surface and the fabric subjected to an electrical field [110]. However, it takes longer than one second to charge nonmetallic fabrics (5 msec. for metallic fabrics), which may significantly slow down textile handling processes [111]. Also, the electroadhesion mechanism is not suitable for a fabric handling gripper, as studies have shown that it leaves damage to the fabric surface [112].

To overcome these limitations, I propose a hybrid method that combines several advantages of the fabric grippers. The proposed gripper employs a soft structure made of elastomer materials, which can be quickly and easily actuated by vacuum pressure. Another crucial design feature is the embedded microneedles, which engage with fabric to assist gripping while do not damage the fabric. The design is inspired by the parasitic fish called lamprey [113] that can attach itself to the host body's skin with a strong holding force (Fig. 3. 1-(a)). The fish's unique oral structure and adhesion mechanism serve as the key ideas for our gripping system.

In this research, I first introduce mechanism and design features of the soft gripper and analytical model to predict the holding force. Then, I experimentally evaluate the performance of the gripper, including holding forces by measuring with different fabrics, comparison with a commercial suction pad, and a single sheet

separation. Lastly, I demonstrate a robotic manipulation using the proposed gripper and robotic systems. I expect the proposed soft gripper to compensate for the physical distance between processes by feeding the fabric to each production machine.

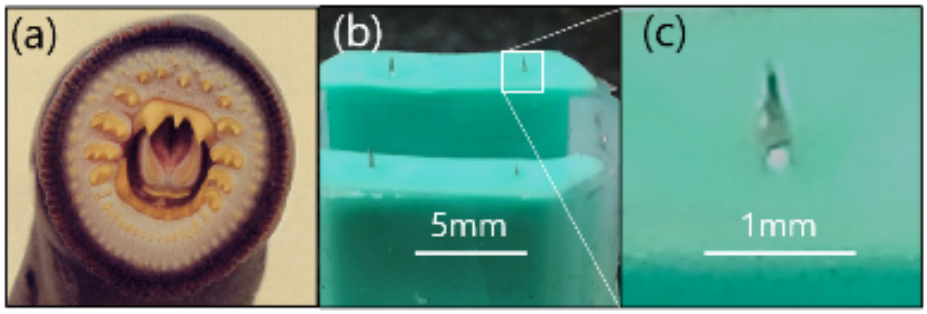

Fig. 3. 1. (a) Oral disc with sharp teeth of Pacific lamprey (Lampetratridentata). (b) Top view of microneedle-embedded soft gripper. (c) Enlarged image of embedded microneedle.

3.2 Design

3.2.1 Gripper design

Finding gripping mechanisms in nature that outperform human hands in specific tasks is not difficult. Among them, I focus on a particular type of parasitic fish called lamprey, known for its strong adhesion force to the surface it clings to. Lampreys achieve mechanical adhesion to their host's body using an oral disc equipped with intrusive teeth. The proposed gripper is designed to have two different silicone elastomers and embedded microneedles, by mimicking the lamprey's buccal flesh and unique dentition (Fig. 3. 1-(b) and 3. 1-(c)). The actuation mechanism is then developed following

the two attachment phases of lampreys: an intrusive phase of tooth penetration and a suctorial phase of adhesion enhancement and retention. The proposed gripper first engages the porous structure of the fabric with the microneedles, like the intrusive phase of lampreys. Vacuum suction is then responsible for operating the rest of the gripping mechanism for stable grasping, like the suctorial phase.

Two main forces are used to hold fabric: friction and suction. The microneedles on the gripper's tip are used only for engaging the fabric, not for holding. The friction is proportional to the coefficient of friction and the normal force applied to two surfaces, and the normal force, in the proposed gripper case, is determined by the contact area between the gripper wall and the fabric and by the pressure difference between the inside and outside of the gripper. Therefore, the proposed gripper can hold the fabric with friction by maximizing the contact area and minimizing air leakage during operation. However, there is a constraint in the practical dimension of the gripper for actual garment manufacturing, in which sewing is one of the most critical processes. Generally, sewing connects two fabric pieces, requiring a margin of 7 mm from the edge of each piece. Hence, no contact should be made beyond the 7 mm margin to prevent any contamination or damage to the fabric, which determines the distance of 6 mm between the two pinching walls of the end-effector (Fig. 3. 2-(a)-left).

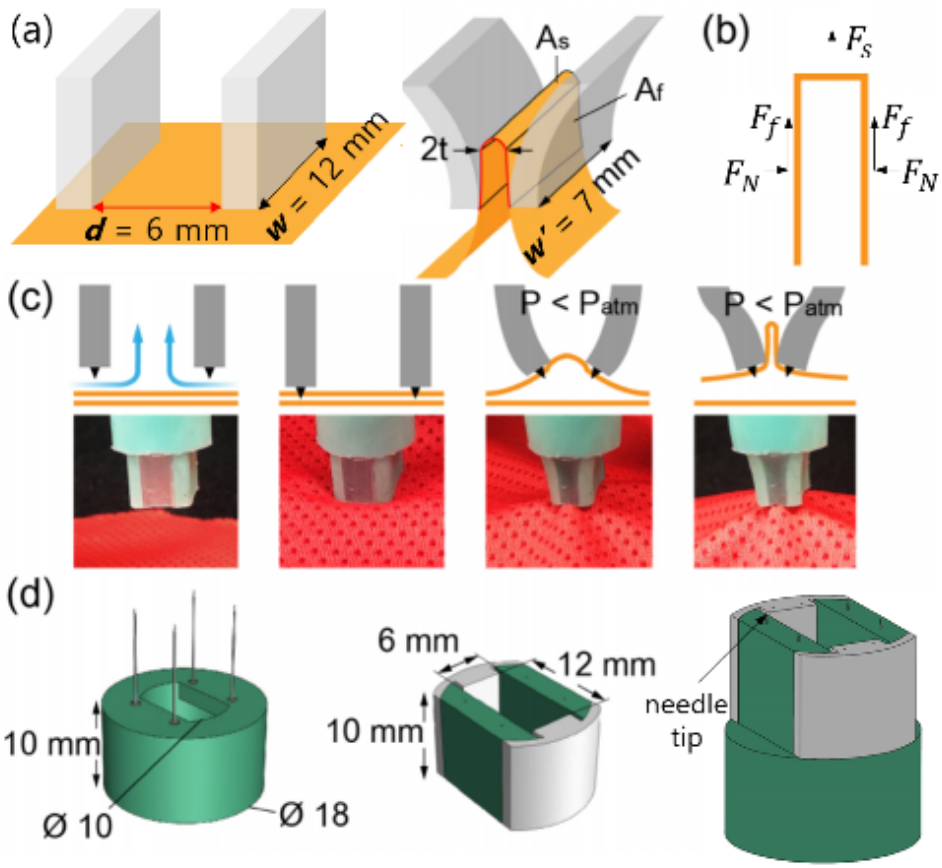

Fig. 3. 2. (a) Schematic of the proposed gripping mechanism. A_s and A_f are the areas of suction $(2t \times w')$ and pinching $((6-2t)/2 \times w')$, respectively. Where t is the thickness of the fabric. (b) Simple free-body diagram with forces applied to the fabric. (c) Schematics (top) and actual photos (bottom) of gripper operation. The pressure inside the gripper, P, is lower than the atmospheric pressure. (d) Gripper base with embedded needles (left), deformable end-effector (middle), and assembled gripper (right).

3.2.2 Analysis

To determine the gripping force, it is essential to first establish

the shape of the contact area. When the gripper contacts with the fabric, it covers a 6 × 12 mm^2 rectangular area. The gripper then deforms as negative air pressure is applied, causing it to fold the fabric in half. During this process, microneedles play a role in the initial sliding and folding of the fabric but lose their engagement once the minimum vacuum pressure is reached. Thus, the holding force is primarily governed by friction and suction forces.

As the gripper holds the fabric due to negative pressure, the width of the pinching wall narrows from 12 mm to 7 mm. The forces exerted on the gripper during this process include the suction force (F_s), friction force (F_f), and normal force (F_N). The contact area due to pinching, A_s, is then calculated as $2t \times w'$. Considering the porous structure of the fabric, the areal ratio of the weaving pattern to the entire fabric including pores, covered by the end-effector, is $a = 1 - N \times \pi \times r^2$, where r is the average radius of the pores, and N is the number of pores in a unit area (1 mm^2). There values are measured using microscopic images for two types of fabric (Table 3. 1), and the suction force acting on the porous fabric can be expressed as:

$$F_s = a \times A_s \times \Delta P = 14(1 - N\pi r^2)t\Delta P, \quad (1)$$

where ΔP is the pressure difference between the inside and the outside of the gripper.

To calculate the friction force (F_f), the contact area between the pinching wall and the fabric (A_f) is $(d - 2t)/2 \times w'$. The friction force can then be determined as:

$$F_f = \mu \times A_f \times \Delta P = 7\mu(3 - t)\Delta P, \quad (2)$$

here, μ represents the friction coefficient between the pinching wall and the fabric, which can be measured using an inclined friction test. The total holding force, accounting for both suction and friction forces, can be calculated as:

$$F_h = F_s + 2 \times F_f = 14[(1 - N\pi r^2)t + \mu(3 - t)]\Delta P. \quad (3)$$

This equation demonstrates that the holding force is directly proportional to the pressure difference (ΔP) and in affected by the fabric's structural and geometric characteristics. As a result, the holding force differs with fabric types.

Table 3. 1. Information on the fabrics used in model calculation

Fabric type	1-1	1-2
Number per unit area [1/mm^2]	4	6
Average radius [mm]	0.15	0.11
Coefficient of friction	1.06	0.92

3.2.3 Operation procedure

The operation procedure of the gripper is depicted in Fig. 3. 2-(c). It begins with the gripper approaching the stack of fabric. After contact with the fabric, the microneedles engage the top sheet. Vacuum pressure is then applied, creating a pressure difference between the gripper's inside and outside, causing the two pinching walls to move toward each other. During this process, the fabric is secured and held by the pinching walls.

3.2.4 Fabrication

The gripper's base (Fig. 3. 2-(d)-left) is made from a relatively rigid elastomer (Smooth-Sil 960, Smooth-On) to provide structural support and connect a pneumatic line. The base is designed as a thick-

walled cylinder with embedded microneedles. Commercially available, thin acupuncture needles (diameter: 200 μm) are used to avoid damaging the fabric.

The actuation part (Fig. 3. 2-(d)-middle) is composed of two distinct materials to enable pinching motion through structural deformation. The same rigid elastomer is used for the pinching walls as the base, while the sidewalls, which are shorter than the pinching walls, are made from a softer elastomer (Ecoflex 0030, Smooth-On). When the actuation part is assembled with the base, the microneedles protrude approximately 0.5 mm from the top surface.

3.3 Experiments and results

Fabrics used in the garment industry show a wide range of structural features, and the gripper's performance varies depending on these characteristics. To evaluate the performance of the gripper, I use various fabrics for testing and classify them into three types: Type 1 - porous, lightweight, and thin; Type 2 - densely woven, stiff, and thick; and Type 3 - coated fabrics (Fig. 3. 3 and Table 3. 2).

Table 3. 2. Information on the fabrics used in the experiments

	Type 1		Type 2		Type 3	
Fabric type	1-1	1-2	2-1	2-2	3-1	3-2
Thickness [mm]	0.75	0.62	1.02	1.43	0.33	0.36
Weight [N/mm^2]	2.28	1.47	3.26	3.13	1.35	1.91
Air permeability [cm^3/cm^2/s]	82	160	7.14	0.15	0	0

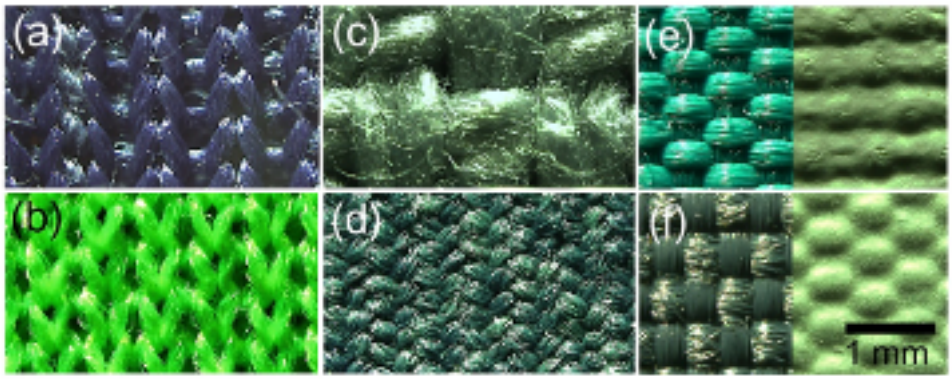

Fig. 3. 3. Magnified photos of the tested fabrics: (a) Type 1-1: Double-mesh French terry, (b) Type 1-2: Coolmax, (c) Type 2-1: Canvas, (d) Type 2-2: Soft-shell, (e) Type 3-1: PU-coated nylon, and (f) Type 3-2: PU-coated polyester. (e) and (f) show one side of woven yarn (left) and the other side with polyurethane coating (right).

The experimental setup to measure holding force is shown in Fig. 3. 4. In all experiments, the gripper is attached to a six-axis industrial robot arm (UR3, Universal Robots). A fabric test piece (60 × 70 mm^2) is placed on a precision balance (PioneerPAG4102, OHAUS), with one end fixed. The gripper moves down to the free end of the fabric, applies vacuum pressure, pinches, and holds the fabric, then moves up along a predetermined path. Weight data and vacuum pressure are recorded simultaneously. In addition, I conduct an experiment to measure the response time of the gripper actuated by the vacuum pump.

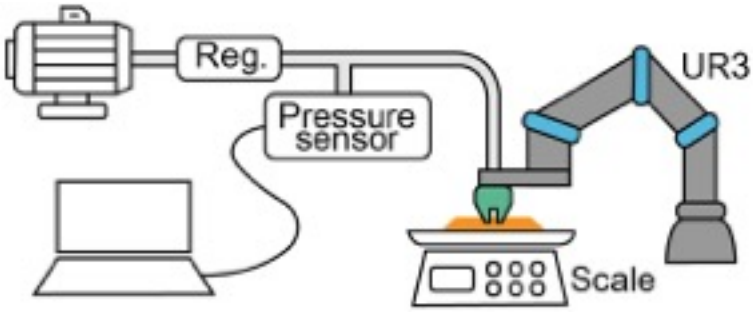

Fig. 3. 4. Schematic of the experimental setup

To evaluate the gripper's response time, first I analyze the pressure response of the vacuum pump. The pump takes approximately 0.61 seconds to reach maximum vacuum power (Fig. 3. 5-(a)), and the gripper takes around 0.93 seconds to reach maximum pressure (Fig. 3. 5-(b)). The actual actuation time of the gripper takes approximately 0.6 seconds, shorter than electrostatic grippers (up to 1 second).

3.3.1 Model evaluation

I input the vacuum pump power at six levels and measure ΔP and holding force for each level. Experiments are conducted on Type 1-1 and Type 1-2 air-permeable porous fabrics, with 10 trials per power level. The model's assumptions are validated by calculating the gripper's effective contact area with the fabric. The holding force is also measured using a gripper without embedding microneedles, and all three fabric types are tested.

The holding force is measured using the precision balance, with the maximum measured weight defined as the gripper's holding force,

which is 1.12 N (Fig. 3. 5-(c)). The holding force is linearly proportional to the ΔP, with slopes determined by the fabric's structural characteristics (Fig. 3. 5-(d)). The actual contact area on the fabric is smaller than calculated in the model, causing a slight overestimation of experimental data. The actual contact area is measured using a fabric sheet with black ink, resulting in a trapezoidal stain (Fig. 3. 5-(g)). The predicted force response based on the actual contact area matches experimental data better than the prediction without adjustment.

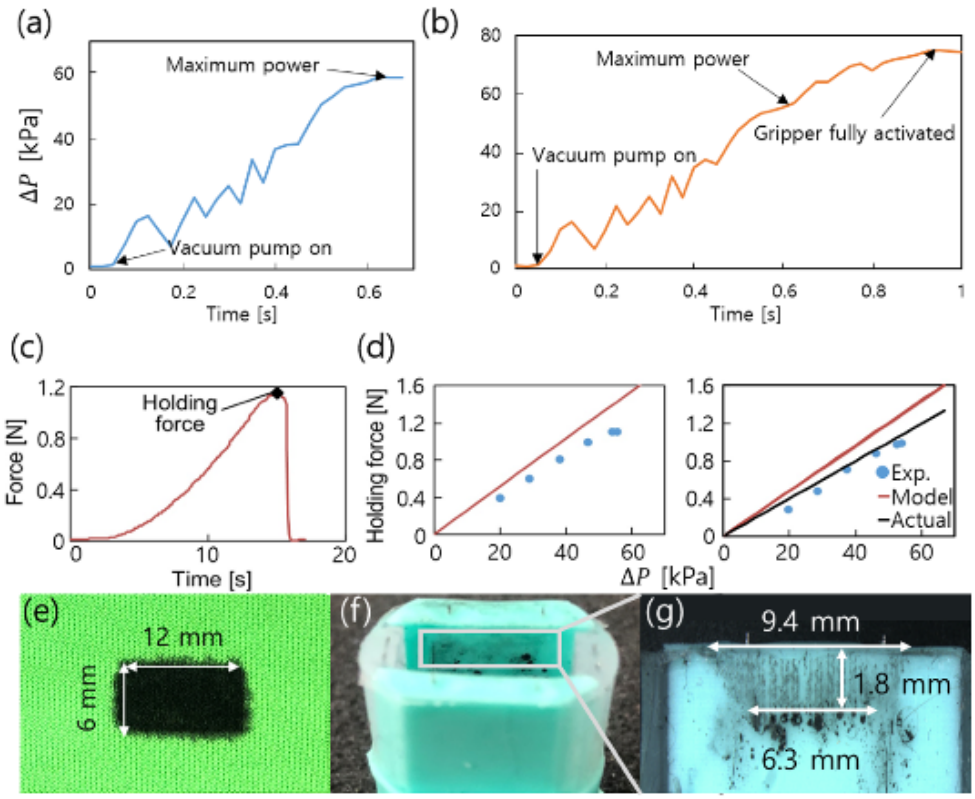

Fig. 3. 5. (a) Pressure response of the vacuum pump. (b) Pressure response of the gripper. (c) Vertical force measured when the gripper picks up fabric. The maximum force, 1.12 N, is the holding force. Type 1-1 fabric was tested with the maximum vacuum power (−60 kPa, sampling frequency: 12 Hz). (d) Holding force as a function of ΔP

showing a comparison between the experimental data (blue dots) and the model prediction (red lines) for Type 1-1 (left) and Type 1-2 (right) fabrics. (e) Mark of black ink on Type 1-2 fabric with the size of the area covered by the gripper before pinching. (f) Mark of the black ink from the fabric on the inside of the pinching wall after one-time gripping. (g) Enlarged image of the inside of the pinching wall showing the size of the black mark.

3.3.2 Comparison test

I conduct an experiment on the effect of the embedded microneedles to the changes in internal pressure and the holding force. In addition, damage to fabrics by microneedles of varying diameters is compared, as even minor damage can impact the final product's quality. Penetration marks made by needles with diameters of 200, 500, and 900 μm are visually inspected by the microscope. Furthermore, I compare the proposed gripper to that of a commercial vacuum pad (VPC10R6J, Pisco) with 10 mm diameter using all three Types of the fabrics since both the gripper and the suction pad have similar cross-sectional area of inlet (proposed gripper: 72 mm^2, suction pad: 78.5 mm^2).

Tips of the embedded microneedles on the gripper surface are highly effective in holding the fabric during initial buckling and pinching motion. The gripper is tested with and without microneedles for different fabric types, and it effectively buckles and pinches all fabrics when microneedles are present. However, without needles, the gripper could not hold the Types 2 and 3 fabrics. I compare ΔP for

grippers with and without microneedles tested on different fabrics (Fig. 3. 6-(a)-top). There is no significant difference in performance for Type 1 fabrics, while ΔP was much smaller for the Types 2 and Types 3 without microneedles. The measured holding forces are higher for all fabric types when microneedles are used (Fig. 3. 6-(a)-bottom).

I compare the proposed gripper with the commercial vacuum pad. The proposed gripper shows a significant change in pressure for Type 1 fabrics (Fig. 3. 6-(b)-top). The proposed soft gripper generates 4.4 and 7.1 times larger the holding force than the suction pad, for Type 1-1 and Type 1-2 fabrics, respectively (Fig. 3. 6-(b)-bottom). This indicates that the soft gripper outperforms the suction pad when gripping the air-permeable porous fabrics. Since the proposed soft gripper can handle a wider range of fabrics than the suction pad, the soft gripper can be used more flexible.

I conduct an experiment to compare damage caused by the penetration of needles with different diameters. The diameter of 200 μm microneedle does not damage the fabric, while needles with diameter of 500 μm and 900 μm leaves unrecoverable holes and damages the fabric structure (Fig. 3. 6-(c)). Microneedles with diameters exceeding 500 μm are not suitable for practical applications due to the permanent damage.

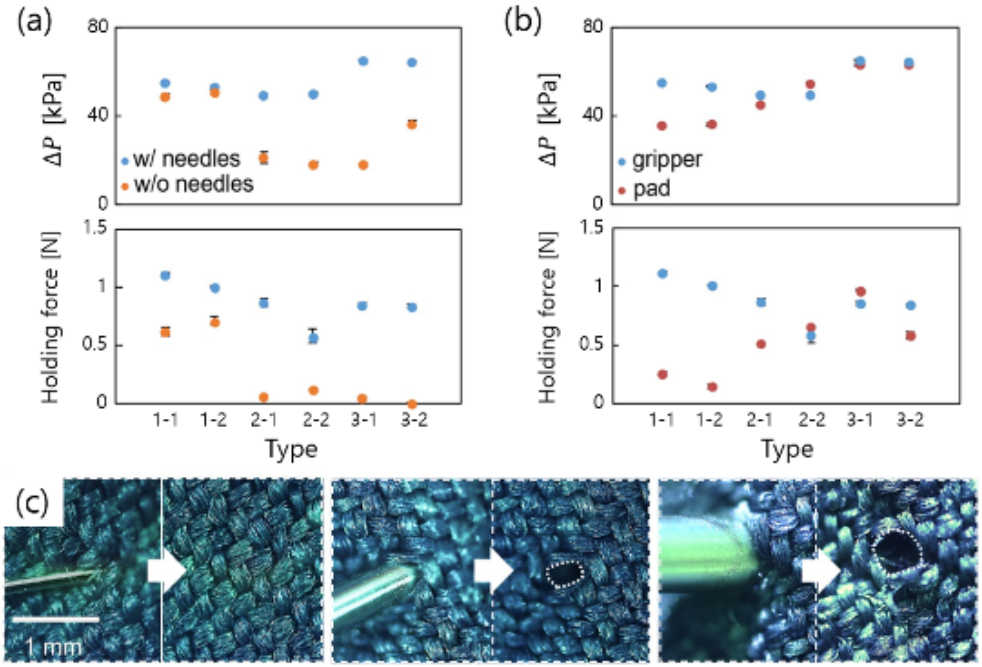

Fig. 3. 6. (a) Performance comparison between grippers with and without needles: pressure difference between the inside and the outside of the gripper (top) and holding force (bottom). (b) Performance comparison between the soft gripper and the vacuum pad. (c) Microscopic images of Type 2-2 fabric after being punctured by microneedles with different diameters (200 μm, 500 μm and 900 μm from left to right).

3.3.3 Durability test

I conduct an experiment of the durability of the proposed gripper by gripping and releasing a single Type 1-2 fabric sheet on a flat surface over 20,000 cycles. I collect the changes in ΔP during the cycles to inspect the structural reliability of the proposed gripper.

Since ΔP has a direct relationship to determine the holding force,

I measure ΔP during cyclic gripping and releasing tests to investigate the durability of the proposed gripper under repeated actuation. The gripper is experienced gripping and releasing pressure profile and reaching maximum ΔP, as shown in Fig. 3. 7-(a). Even after 10,000 actuations, ΔP remains consistent without noticeable change. The average maximum ΔP value is 55 kPa, with a standard deviation of 0.2 kPa (Fig. 3. 7-(b)). The trend line slope of the tests is 1×10^{-8}, confirming that there is no decrease in ΔP over 20,000 cycles.

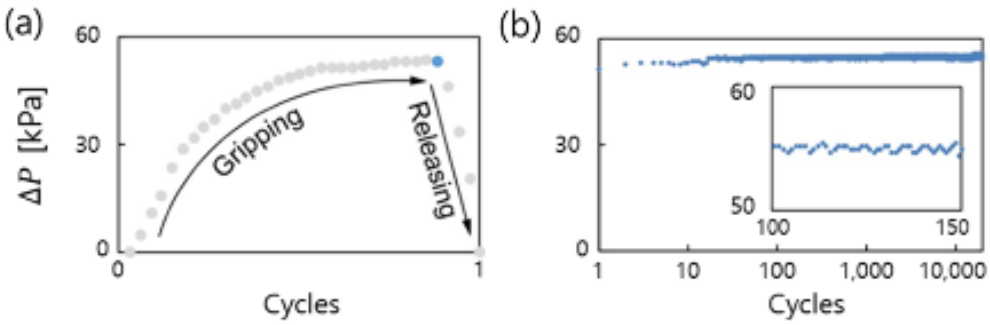

Fig. 3. 7. Results of durability test: (a) change in the pressure difference during a single cycle of gripping and releasing with ΔP defined by blue dot and (b) ΔP for the same tests over 10,000 cycles with enlarged view between 100 and 150 cycles (right).

3.3.4 Single-sheet handling

Lifting only a single fabric sheet from a stack is crucial for the gripper in garment production. Since 60 to 100 sheets of fabric per batch are typically used in garment production, I place 80 fabric sheets on the precision balance. The gripper moves down to the stack, picks

up the top sheet, and moves up from the surface. By comparing weight reduction before and after picking up the fabric, it is possible to determine the number of picked up sheets lifted out. Success is defined as picking up only the top sheet, while failure is defined otherwise. The success rate is calculated as the number of successful grips divided by the number of total trials for each fabric. This experiment is conducted with all three fabric types.

As summarized in Table 3. 3, the proposed soft gripper achieves success rates over 70% for Type 1 and Type 2 fabrics and 100% for Type 3. Type 1-2 and Type 2-2 fabrics have higher success rates than Type 1-1 and Type 2-1, respectively, due to higher air permeability in Type 1-1 and Type 2-1 that occasionally result in picking up two or more sheets simultaneously.

The suction pad does not pick up a single sheet for Type 1 and Type 2 air-permeable porous fabrics but achieves a 100% success rate for Type 3. The suction pad consistently picks up around 10 fabric sheets at a time for Type 1 and Type 2. However, coating on the Type 3 fabric prevents the vacuum from affecting sheets below the top one.

Table 3. 3. Results of single-sheet handling test with the numbers of successful trials (success rate)

Fabric type	1-1	1-2	2-1	2-2	3-1	3-2
Soft gripper	58 (72.5%)	69 (86.3%)	65 (81.3%)	71 (88.8%)	80 (100%)	80 (100%)
Suction pad	0 (0%)	0 (0%)	0 (0%)	0 (0%)	80 (100%)	80 (100%)

3.4 Demonstration

3.4.1 Task performs based on the number of gripped sheets

Since it is important for the gripper to separate a single sheet from a stack, I propose a method to estimate the number of gripped sheets using capacitance measurements. The capacitance C is expressed as:

$$C = \epsilon_0 \epsilon_f \frac{A}{d}, \tag{4}$$

where, C is the capacitance, ϵ_0 is the dielectric constant in free space, ϵ_f the dielectric constant of fabric, A is the area of the electrodes, and d is the distance between electrodes (Fig. 3. 8-(a)). Since the capacitance is inversely proportional to the distance between parallel electrodes, it is possible to estimate the distance by measuring the capacitance when other conditions remain constant. I attach each electrode to both pinching wall of the gripper and connect the electric wires (Fig. 3. 8-(b)).

I conduct an experiment with measuring capacitance by varying the distance between the fingers of the gripper by 0.1 mm. The results show that the measured capacitance is inversely proportional to the distance between fingers, thus the estimation of the number of gripped sheets is possible (Fig. 3. 8-(c)). Monitoring the gripping process and performing tasks based on the number of gripped sheets are possible (Fig. 3. 8-(d)).

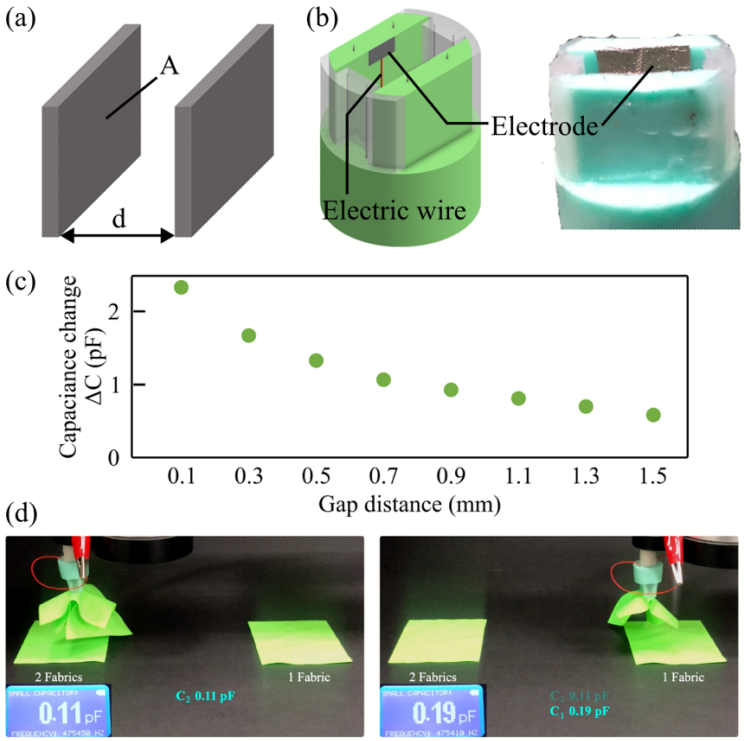

Fig. 3. 8. (a) Capacitance between parallel electrodes. (b) Schematic and actual prototype of electrodes-integrated gripper. (c) Result of capacitance measurements. (d) Task performing based on the number of gripped sheets.

3.4.2 Handling high air permeability fabric

To enhance performance of the gripper for a high air-permeable fabric with a loosely woven structure (Fig. 3. 9-(a)), I add a membrane to the tip of the gripper to remove exposure to the air (Fig. 3. 9-(b) and 3. 9-(c)). This design fully separates the gripping task into two substasks: pinching and locking. The microneedles first engage the fabric, and then the applied vacuum deforms the gripper for pinching. After fully pinched, the gripper locks the structure and securely holds

the fabric. This makes the gripping performance no longer dependent on the air permeability of the fabric, but solely on the pinching and locking mechanism (Fig. 3. 9-(d)).

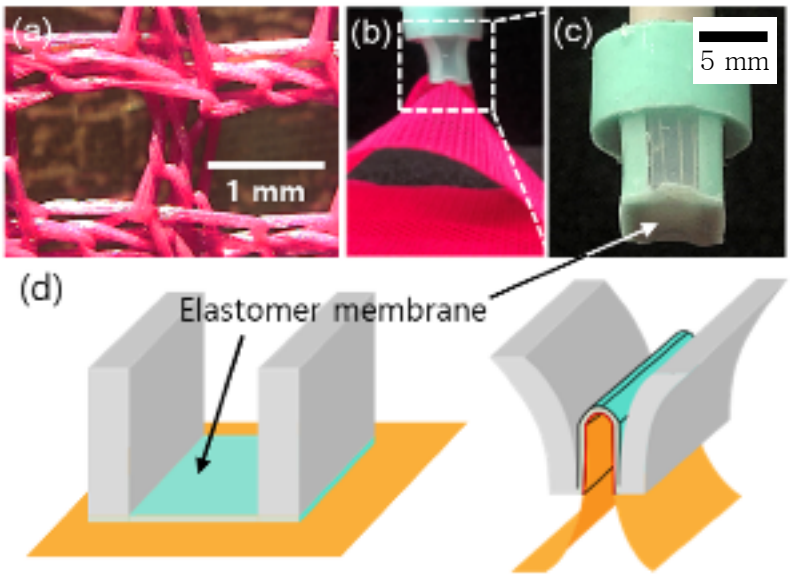

Fig. 3. 9. (a) Fabric with high air permeability. (b) Modified gripper prototype holding the fabric shown in (a). (c) Magnified image of the Modified gripper showing the closed tip with an elastomer membrane. (d) Gripping mechanism of the modified gripper.

3.4.3 Automatic stamping device

A process called numbering or stamping is a part of the production process of clothing that involves stamping the fabric to control the quality of intermediate parts and final products. Simple process of stamping the fabric, picking up, and flipping it over, but this process is not automated and done manually. I incorporate the proposed gripper into a preliminary prototype of a pattern-numbering machine (I and

Hojeon Ltd. developed) to assess the applicability of the gripper (Fig. 3. 10-(a) and 3. 10-(b)). The soft gripper displays reliable performance in the number task, which involved repeated motions of stamping a serial number and separating a fabric sheet from a stack at a relatively high speed (approximately 1 Hz).

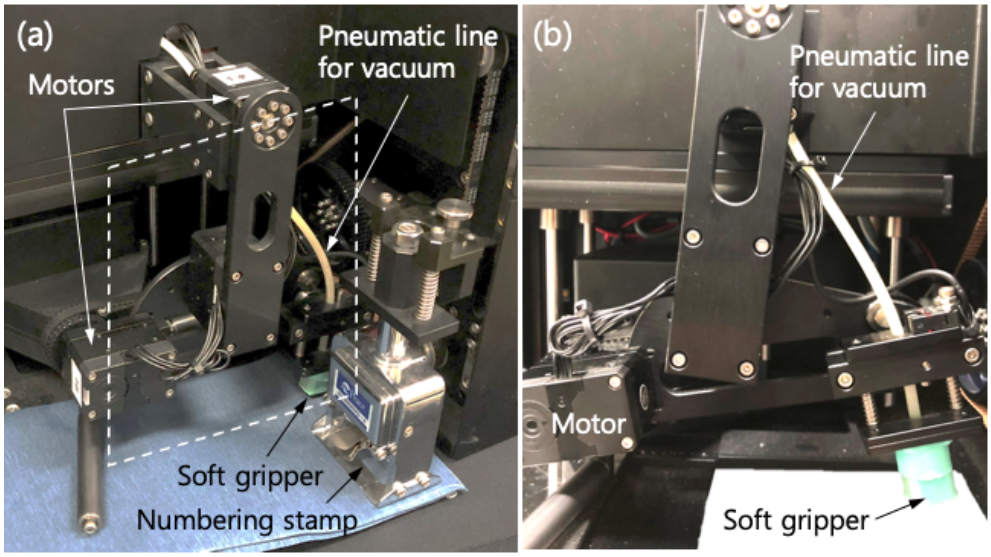

Fig. 3. 10. (a) Prototype of pattern-numbering machine composed of soft gripper, three degrees-of-freedom robotic arm, and stamp for numbering. (b) Magnified image of dotted box in (a).

3.4.4 Fabric handling with mobile platform

Smart garment manufacturing environments involve not only automating individual production equipment (Chapter 2), but also automating related processes. Since this requires physically connecting each production machine, I propose a mobile platform system for handling fabrics (Fig. 3. 11). Since rotation in a small space

is difficult, I adopt a mecanum wheel, make an interface for connecting the soft grippers, and mount an industrial robotic arm (UR5e, Universal Robots). The mounted LiDAR (URG-94LX-UG01, Hokuyo) and depth camera (RealSense L515, Intel) allow for spatial positioning and navigation, as well as the ability to recognize and respond to obstacles ahead. It can drive autonomously to a target location, recognize and pick up fabric by vision, and transport the fabric to a location with a pattern former.

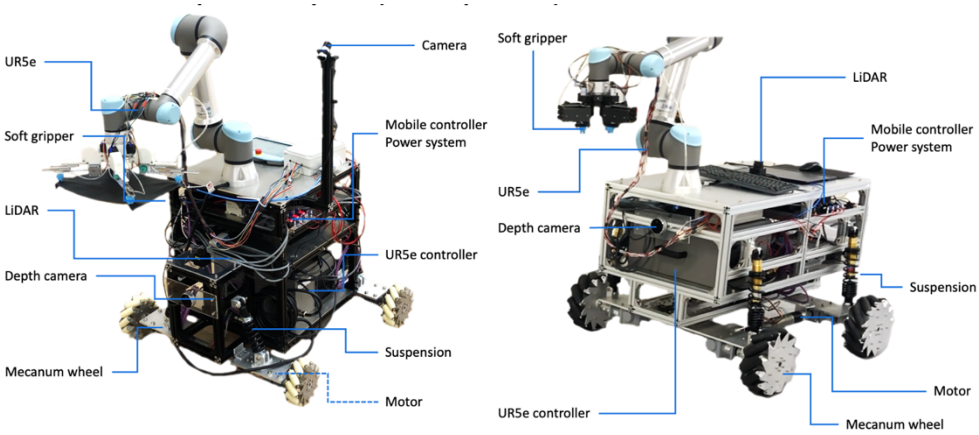

Fig. 3. 11. Developed mobile platforms. Version 1 for left and Version 2 for right.

3.5 Discussion

I develop a soft gripper for handling delicate fabrics, inspired by the adhesion mechanism of a parasitic fish called “lamprey.” The proposed gripper can pick up and hold a single sheet from a stack and does not cause any damage to the fabric. I first model the holding force and experimentally assess the performance of the gripper with various

fabrics. The maximum holding force is 1.12 N. I demonstrate high success rates in picking up a single sheet of air-permeable fabric, which is impossible with a commercial suction pad. In addition, I display durability in repeated actuation over 20,000 cycles. I believe the proposed gripper has significant potential for enabling smart garment manufacturing.

Chapter 3. Part II. Multi-Functional Soft Gripper with Microneedles and Integrated Sensing for Robotic Fabric Handling

3.6 Backgrounds

The demand for automated fabric handling systems continues to grow in labor-intensive garment manufacturing industries. Despite recent advances in robotics and gripper technologies, automation in garment production remains limited due to the complex and unpredictable behaviors of fabrics, which comes from characteristics such as air permeability, thickness, friction between the gripper and the fabric, and stiffness [52]–[54], [104]. To address this issue, soft grippers with improve adaptability have been proposed as alternatives to conventional grippers. The actuation mechanisms of the soft grippers include, pneumatic [45], [47], [48], tendon-driven [42], [43], [114], vacuum jamming [49], and vacuum suction [50], [51], [115], [116]. However, these grippers typically specialize in only a few specific fabric properties and lack the versatility required to handle a wide range of fabrics with different characteristics. Studies have been conducted on grippers that utilize the properties of soft materials. The soft spiral gripper was able to grasp objects with various shapes but was unable to hold fabric without crumpling it [117].

The self-sealing suction gripper could change the volume of the suction cavity and grasping different sizes and shapes objects but was not suitable for handling air-permeable porous fabric [118]. The microneedle-embedded pinching gripper was effective in gripping both porous and non-porous coated fabrics but had difficulties when separating a single sheet of porous fabric from a stack due to undesired vacuum force acting underneath the top sheet [72]. Studies have been conducted to implement multi-actuation or multi-functional using grippers made of soft materials. Stiffening through electrostatic adhesion and layer jamming has been studied to assist the grasping force [119], [120]. Studies have also been conducted on soft grippers that conform to the shape of objects to grasp of varying sizes and stiffness [121]–[123]. Studies have been conducted to add functionality to vacuum grippers by changing the inlet area to maintain vacuum pressure between the object and the gripper [118], [124]. However, the presented studies are not suitable for handling porous sheet-like objects such as fabrics. Vacuum suction has the problem of picking up multiple sheets of porous fabric at once, and electroadhesion causes damage to the contact surface. For grippers that implement the pinching method, the stroke is larger than the seam allowance.

Key requirements for a gripper for handling delicate fabrics are multi-modes actuation for fabrics with different air permeability [125], [126], single sheet separation from a stack [127]–[129], the adaptable capability to grip fabrics with different surfaces without damaging them [52]–[54], [104], [130], and compliance for safety and compensation for non-ideal contact. In addition, the gripper requires sensing capability for automation of fabric handling. This is important since the performance of single sheet separation is

significantly relying on the normal force applied to the fabric by the gripper. There also exists the minimum normal pressing force by the gripper to buckle and grip the fabric. These forces are different from each fabric type and depending on its frictional coefficient and flexural rigidity [105], [131]. For practical use, gripper needs easy fabrication process and maintenance. Therefore, I propose a multi-functional soft robotic gripper that satisfies the key requirements and overcomes the limitations of the conventional grippers.

I apply multi-actuation of both pinching and suction in a single structure using the properties of soft material. Fabric handling grippers mainly use operating principles such as pinching, intrusion, adhesion, electrostatic, and pneumatic actuation, each mechanisms have its own benefits [112]. However, there is no generalized mechanism to handle unstructured and flexible fabrics. Therefore, to use the gripper flexibly and handles a variety of fabrics, a combination of mechanisms must be applied. First, I choose pinching mechanism due to easy deformation of the soft material. Since pinching cannot handle most of non-air-permeable coated fabrics, I choose a suction mechanism to compensate for pinching actuation. I integrate two distinct principles –suction and structural deformation-based pinching within one structure, targeting both fabric types with and without air permeability (Fig. 3. 12-(a), 3. 12-(b), and 3. 12-(c)). Using soft material characteristics with a high degree of freedom, I develop a structure capable of both pinching and suction. In addition, a multi-functional compliant structure is proposed to handle the fabric with non-ideal contacts and provide tolerance for excessive loads during gripping. Additionally, a sensor is integrated with an air chamber created by sealing the compliant bellow-shaped posts to measure the internal pressure during contact with the fabric.

The actuation part of the gripper has composite structure for multi-actuation, and the compliant structure is added for multi-functionality, so the overall gripper structure is complex. To simplify the production process, I apply stereolithography apparatus (SLA) 3D printing. Recent advancements in 3D printing technologies enable direct printing and assemble of soft grippers and their components that previously required multiple molds [27], [112], [132]–[134]. By using 3D printing technologies instead of manual fabrication, which is prone to human error, the gripper can be fabricated with consistent performance, uniform quality, and complex structures, enabling multi-functionality of the grippers (Fig. 3. 12-(d)).

An important factor affecting success of single sheet separation during pinching is pressing force [128], [129]. Since the required pressing force range varies with fabrics, a sensor is integrated into the gripper to measure and control the pressing force. By integrating a commercial air pressure sensor that measures change internal pressure of the gripper, pressing force can be estimated and controlled maintaining compact form factor of the gripper. This is crucial since the contact area on the fabric allowed for quality control in garment production must be at most 6.34 mm from the edge [135], making a bulky system for handling and sensing unsuitable.

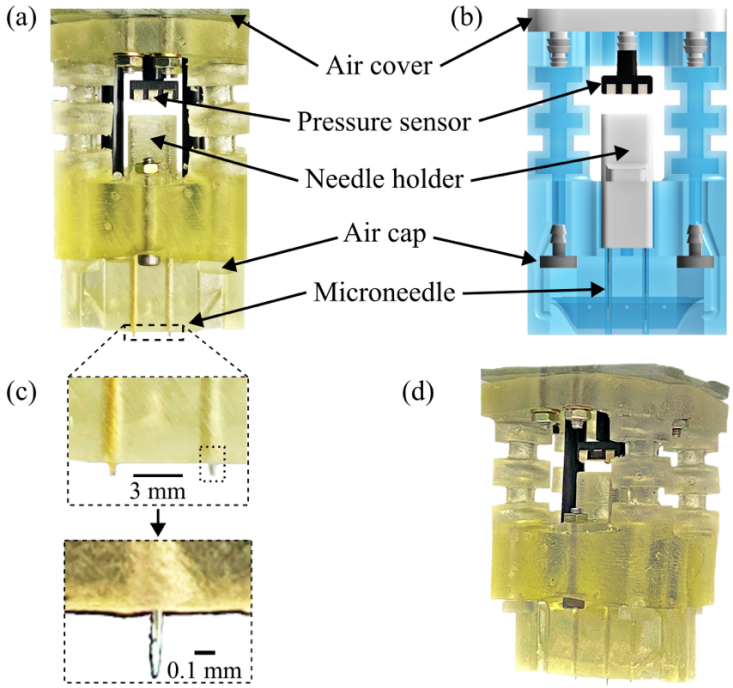

Fig. 3. 12. (a) Photo and (b) schematic front view of the proposed gripper showing the main components. (c) Magnified views of the embedded microneedles. (d) 3D view of the gripper.

3.7 Design

3.7.1 Operation procedure

Grasping begins with approaching the target fabric and sensing contact (Fig. 3. 13-(a) and 3. 13-(b)). For suction mode, vacuum pressure is applied between the membrane and the fabric (Fig. 3. 13-(c)). For pinching mode, vacuum pressure is applied within the membrane to deform the fingers for pinching (Fig. 3. 13-(d)).

3.7.2 Integrated pressure sensor and multi-functional structure

The proposed gripper has four features of main design elements: multi-actuation of pinching and suction, easy assembly and replacement of microneedles, structural compliance for stable gripping, and an integrated pressure sensor. The dimensions of the gripper are determined based on the length of a commercial microneedle, 35 mm (HL-001 Series, HLMedical), and the seam allowance (6.34 mm). The overall shape and components of the gripper are depicted in Fig. 3. 13-(e). Total height of the gripper, including its cover, is 53mm, with a width of 42 mm. This configuration and compliant structure enable the tip position horizontally up to ±3.7 mm on the xy-plane.

The gripper is designed to offer structural compliance and contact sensing capability. A pneumatic pressure sensor is connected to a 3D-printed air cover, acting as a mechanical connector to a robot manipulator (Fig. 3. 13-(f)-i). Pressure sensing is possible by four compliant posts that deform, generating changes in internal pressure. The air cover has five barbed air ports, each connected to the compliant post and the pneumatic pressure sensor is connected to the center port. Air chambers of each chamber are interconnected through pipes, and their total pressure is measured by the pressure sensor at the center of pipe. The inner diameter of the pipe and port are chosen to be 1.4 mm, the smallest dimension that can be made by 3D printing without clogging, to minimize passive volume.

The four bellow-shaped posts, positioned at the corners of the gripper, provide structural compliance, which distributing excessive load during contact with fabrics (Fig. 3. 13-(f)-ii). Each post can bend

according to the orientation and contact force, stabilizing the position of the fingertips and aligning normal to the fabric.

3.7.3 Soft gripper with multi-modes actuation

The actuation part of the gripper (Fig. 3. 13-(e)) is designed to perform two independent actuation modes. During contact with fabric, a cavity forms, enclosed by the V-shaped membrane, fingertips, and fabric (Fig. 3. 13-(c)). Vacuum pressure applied in this cavity activates the suction mode to grasp non-air-permeable coated fabrics. Vacuum pressure applied inside of the membrane activates the pinching mode (Fig. 3. 13-(d)), pulling the membrane upwards and closing fingertips, enabling the pinching motion. As the whole structure is 3D printed at once, the pinching fingers and sidewalls share the same material properties. However, since the fingers need to be flexible to bend easily toward the center of the gripper under vacuum without buckling or collapsing, the sidewalls are angled to guide fingers towards the center (Fig. 3. 13-(f)-iii)

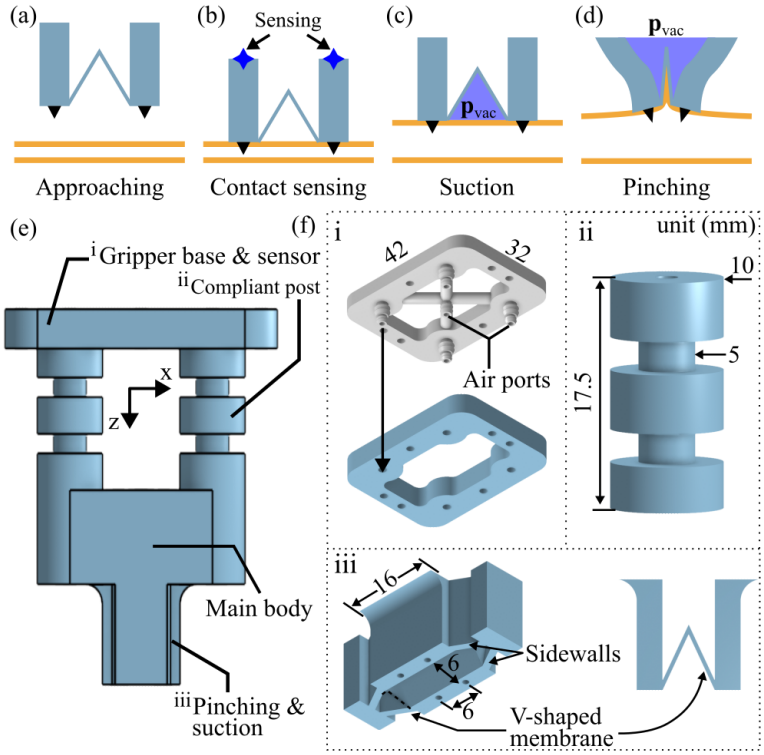

Fig. 3. 13. (a)-(d) Gripper operation procedure corresponding to combined suction and pinching working principles. (e) Overall design and main components of the gripper. (f) Details of the components. i. Air cover and gripper base for integration of barometric pressure sensor. ii. Bellow-shaped compliant post. iii. Gripper fingers and a membrane for pinching and suction modes.

3.7.4 Analysis

The force applied to the fabric by the gripper differs based on the actuation modes. These relationships are expressed as:

$$F_{suction} = A_{eff} \times p_{vac}, \tag{5}$$

$$F_{pinching} = 2 \cdot F_f = 2 \cdot \mu \times F_n = 2 \cdot \mu \cdot A_f \cdot (p_{vac} - p_0), \tag{6}$$

where $F_{suction}$ and $F_{pinching}$ are the suction and pinching forces of the

gripper, respectively, A_{eff} is the effective suction area under vacuum, p_{vac} is the vacuum pressure applied between the fabric and the membrane and inside of the membrane, F_f is the frictional force, μ is the friction coefficient between the gripper and the fabric, F_n is the normal force generated by the pinching motion, and A_f is the pinching area, p_0 is the pressure at initial contact, which is unique to each fabric (Fig. 3. 14-(a) and 3. 14-(b)).

In both actuation modes, the exerted force is affected by the contact area (Eqns. 5 and 6). For the suction mode, the effective area A_{eff} is determined experimentally rather than using the designed area, due to the characteristics of the soft elastomer-based vacuum pad [136]. For the proposed gripper, A_{eff} is 40 mm^2. In pinching mode, the area A_f, which is affected by thickness of the fabric, is determined through simulation analysis.

To separate a single sheet of fabric from a stack, the gripper must press the fabric by an appropriate force, which will be introduced later. Therefore, a sensor is required to measure and control the pressing force for proper operation. The gripper experiences internal volume changes as the compliant posts deform during pressing. According to Boyle's law, pressure increases as volume decreases in a closed system. The closed system of the gripper consists of the active volume (V_a), which changes when external force is applied, and the passive volumes (V_p) that remain constant (Fig 3. 14-(c)). By the design, V_p is 213.91 mm^3, independent of the external force.

Using the indicated parameters in Fig. 3. 14-(d), the relationships between the initial and the final pressures and the volumes are expressed as:

$$p_1 \cdot V_1 = p_1 \cdot (V_p + V_a) = p_2 \cdot V_2, \quad (7)$$

$$V_2 = 4A_{eq} \times (h_1 + \Delta h) + V_p, \quad (8)$$

where p_1 is the initial pressure inside of the gripper when the external force is zero and is equivalent to the ambient pressure of 100.6 kPa, p_2 is the final internal pressure when the external force is applied, V_1 and V_2 are the corresponding volumes, A_{eq} is the equivalent cross sectional area of the bellow-shaped post approximated to a cylinder (5.31 mm^2), h_1 is the initial height of the bellow-shape post (18.7 mm), and Δh is the height change due to the pressing force. Using these equations, p_2 can be expressed as:

$$p_2 = \frac{p_1 \cdot (V_p + V_a)}{4A_{eq} \times (h_1 + \Delta h) + V_p}. \tag{9}$$

Given the pressure p_2, the change in height Δh can be determined. By finding relationship between the Δh and the pressing force, the contact force can be obtained from the measurements of p_2. I use a pneumatic pressure sensor (XGZP6847-040KPGPN, CFSensor) to measure the internal pressure of the bellow-shaped compliant posts. By conducting a tensile test, relationship between Δh and the pressing force can be determined.

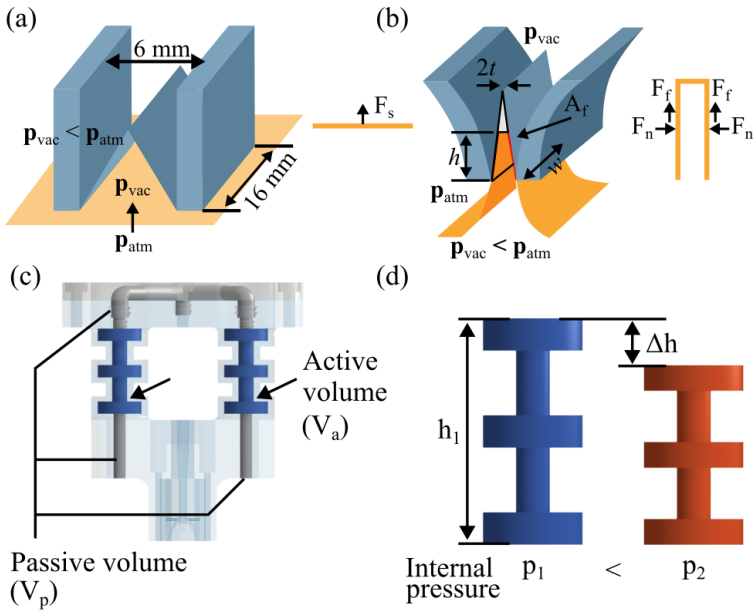

Fig. 3. 14. (a) Suction mode and free body diagram. (b) Pinching mode and free body diagram. (c) Closed pneumatic system schematic composed of passive and active volumes. (d) Initial state (Left) and compressed state (Right).

3.7.5 Simulations

Finite element analysis (FEA) is conducted using COMSOL Multiphysics® (COMSOL) to optimize the gripper design features. The gripper is made from a soft photopolymer resin (Elastic 50A, Formlabs) for stereolithography (SLA) 3D printing. Before conducting simulation, I perform a tensile test with a motorized test stand (Mark-10, Mark-10 Corporation) on a printed elastomer specimen to obtain the material's Neohookian parameter (Fig. 3. 15-(a)). The Neohookian model is suitable for small strains [137], and the result is shown in Fig. 3. 14-(b).

The pinching force is determined by the coefficient of friction and the normal force (Eqn. 6). As the normal force is affected by the gripper tip structure, I optimize the finger design to maximize the normal force (Fig. 3. 15-(c) and 3. 15-(d)). I first compare the normal force between different shapes of sidewalls (flat and curved) and the membrane (flat and V-shaped). The normal force is higher with flat sidewalls (Shape 2) than with curved ones (Shape 1) since two angled flat sidewalls are easier to fold than curved one. Similarly, the V-shaped membrane (Shape 3) shows a higher normal force than the flat one (Shape 2) and is used in the final design of the gripper.

Next, three design variables are chosen through simulation, affecting the suction cavity volume and the normal force based on Shape 3 (Fig. 3. 15-(e)). The suction cavity represents the space enclosed by the fabric and the V-shaped membrane where vacuum pressure is applied, and its volume is determined by the angle of the V-shaped membrane (θ) and the offset (d_{offset}). As pinching occurs by folding the membrane, The membrane thickness ($t_{membrane}$) would affect the normal force. Therefore, I first simulate the normal force to input pressure for different d_{offset} and $t_{membrane}$ values with a fixed θ of 35°. The result in Fig. 3. 15-(f) shows that the normal force increases as $t_{membrane}$ and d_{offset} decrease. With a thickness and offset of 0.5 mm and 0 mm, respectively, I conduct simulation to predict the normal force with varying θ from 25° to 70° (Fig. 3. 15-(g)). The normal force reaches its maximum value at an angle of 45°, decreasing significantly as the angle became smaller. Although higher normal forces can be achieved with $t_{membrane}$ of 0.4 mm or less, I choose a thickness of 0.5 mm for stable 3D printing. Experimentally, a membrane thickness of 0.4 mm does not maintain its structure during printing. The angle θ is selected as 35° to balance the normal force

and suction cavity volume.

As delineated in Chapter 3.7.4 and Eq. 6, the pinching force exhibits a direct proportionality to the contact area, denoted as A_f. This area varies based on the specific fabrics in question and was ascertained via simulation. For simplicity, I simulate by only altering the thickness parameter, while maintaining the properties of all simulated fabric consistent with rubber (Young's modulus 100 MPa). The simulations are conducted for all air-permeable fabrics, with visualized outcomes present for fabrics 1-6 and 1-7 from Table 3. 4 in Fig. 3. 15-(h). These specific fabrics are chosen to visualize the effect of thickness on the contact area, given their similar coefficients of friction but substantial thickness disparity. The computed average contact areas are 7.53 mm^2 and 8.54 mm^2 for fabrics 1-6 and 1-7, respectively. The comprehensive results indicate a trend of decreasing average contact area with increasing fabric thickness.

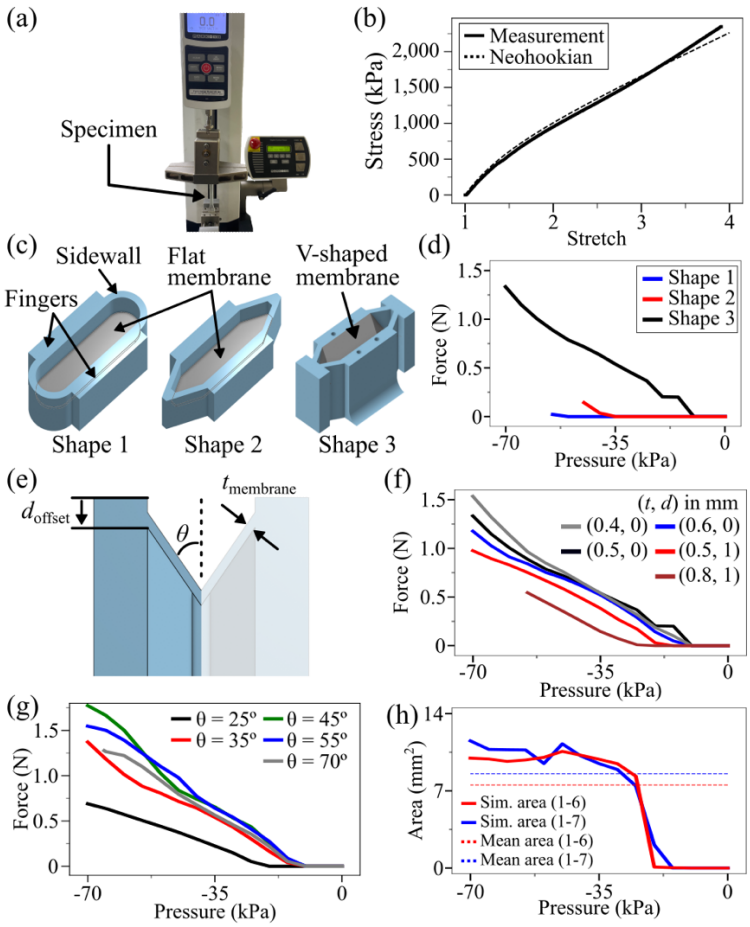

Fig. 3. 15. Simulation results of normal force in pinching. Tensile test setup (a) and result (b). (c) Membrane shapes for simulation. (d) Normal force in response to input pressure for different membrane shapes. (e) Optimization parameters of the V-shaped membrane. (f) Normal force in response to input pressure for different thicknesses and offsets of the V-shaped membrane. (g) Normal force in response to input pressure for different angles θ. (h) Contact area change in response to input pressure for two types of fabrics: thick and air-permeable fabric (Type 1-6, red) and thin and air-permeable fabric (Type 1-7, blue). Refer to Table 3. 4 for the fabric.

Table 3. 4. Information on the fabrics used in experiments

Fabric label	1-1	1-2	1-3	1-4	1-5	1-6	1-7	2-1	2-2	2-3
Air permeability [mm/s]	32.8	255	872	628	56.9	15.3	49.8	0	0	0
Flexural rigidity [10^{-4} Nm]	3.89	6.41	13.2	6.13	3.88	2.96	13.6	3.91	6.34	12.0
Thickness [mm]	0.25	0.32	0.58	0.31	0.23	0.35	0.15	0.07	0.2	0.46
Coefficient of friction	2.48	3.73	2.14	3.27	2.36	1.15	1.33	1.37	1.73	1.54

3.7.6 Fabrication

The proposed gripper is fabricated using an SLA 3D printer (Form3, Formlabs) with soft photopolymer resin (Elastic 50A, Formlabs) (Fig. 3. 16-(a)). Postprocessing is done by washing the printed part with isopropyl alcohol and curing under UV (Form Cure, Formlabs), the gripper can be actuated.

The air cover and the needle holder are also fabricated by 3D printing using another photopolymer resin (Clear, Formlabs). The needle holder is designed to enable easy integration and replacement of the microneedles rather than direct embedding in the elastomer (Fig. 3. 16-(b)), not requiring any additional alteration and facilitating easy replacement when damaged. The final assembly of the proposed gripper is depicted in Fig. 3. 16-(c).

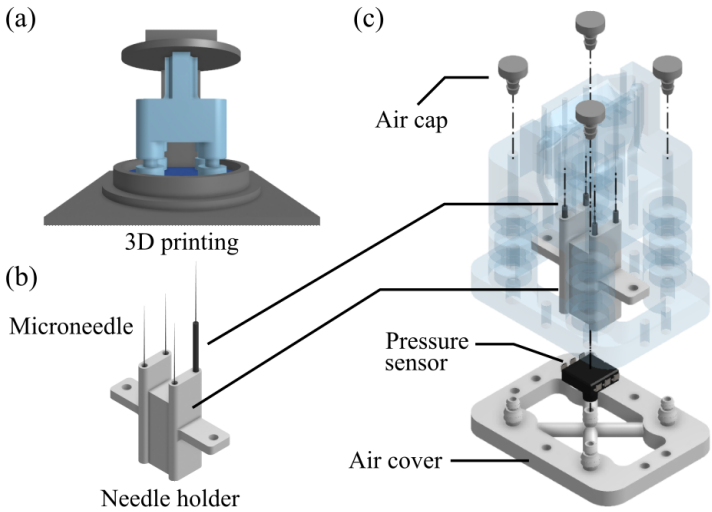

Fig. 3. 16. Fabrication process. (a) 3D printing of the gripper body. (b) Microneedles and its holder. (c) Final assembly.

3.8 Experiments and results

I first conduct experiments to show the feasibility of the two actuation modes in a single gripper structure. Then the pinching and the suction performances are examined. The experiments are conducted with seven types of air-permeable fabrics and three types of coated fabrics with no air permeability.

The gripper is mounted at the end of an industrial robotic arm (UR5e, Universal Robots), and the holding force is measured using a precision scale (Pioneer PAG4102, OHAUS). A test fabric (60 × 70 mm^2) is placed on the scale with one edge fixed and lifted by the gripper while measuring the weight simultaneously to find the maximum pinching force. To determine the maximum lifting force by suction, a stainless-steel container is used for added weights and lifted by the suction mode of the gripper. In the following experiments,

I use seven types of air-permeable and three types of non-air-permeable fabrics. Experiments are conducted to determine the air permeability and the flexural rigidity of the fabric, which are basic properties related to vacuum suction and pinching, respectively. I use an air permeability tester (FX 3300-IV, TEXTEST) to measure the air flow rate based on ISO 9237 and find the flexural rigidity based on ASTM D1388 of the fabrics [138]. The properties and the labels of the fabrics tested are summarized in Table 3. 4. Images of test fabrics are shown in Fig. 3. 17 (from (a) to (l)), and the experimental setup is shown in Fig. 3. 18.

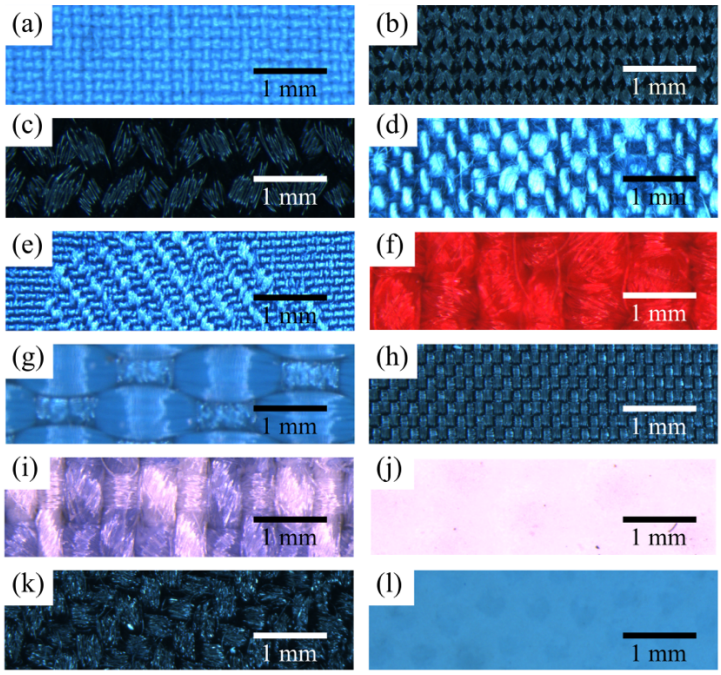

Fig. 3. 17. (a) – (g), air-permeable fabrics. (h) – (l), non-air-permeable fabrics. (i) – (l) indicate that front and back of the fabrics.

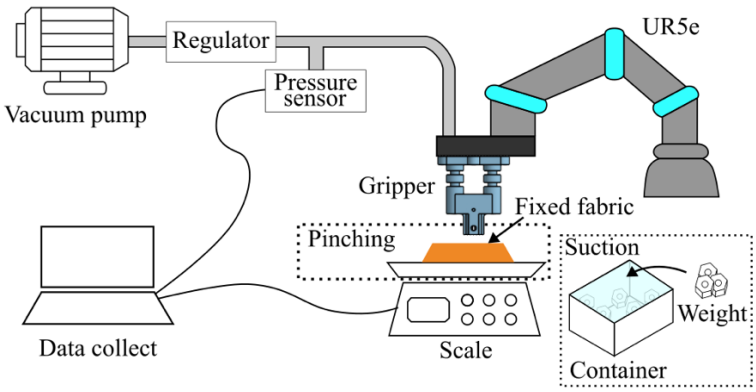

Fig. 3. 18. Experimental setup to determine characteristics of the gripper.

3.8.1 Multi-modes actuation in single structure

Upon contacting the target fabric, the proposed gripper operates either pinching or vacuum suction depending on the type of the fabric (air-permeable or not). For the pinching mode, the two fingers of the gripper buckle the fabric with friction for gripping. If the gripper returns to its original state, the folded part of the fabric stretches, and the fabric is naturally separated from the needles (Fig. 3. 19-(a)).

To verify the damage-free operation of the gripper, I conduct an examination using the fabric samples and a microscope after each actuation. There are no noticeable damages, such as penetration holes by the microneedles or folded lines of buckling fabrics (Fig. 3. 19-(b)-left and 3. 19-(b)-right).

An air-permeable porous fabric (1-1) is placed on top of a non-air-permeable coated fabric (2-2) and separates a single sheet of fabric using both suction and pinching (Fig. 3. 19-(c)-top). The gripper

successfully separates and picks up the air-permeable fabric through pinching. However, suction gripping case, separating the single sheet is not possible because the vacuum pressure is applied to the below non-air-permeable sheet by passing through the mesh of the air-permeable fabric on top. Other air-permeable fabrics (from 1-2 to 1-7) shows same results. When the non-air-permeable fabric is placed on top (Fig. 3. 19-(c)-bottom), single sheet separation is successful with suction but not with pinching. The fingertips slip on the surface of the coated fabric, which leads to the fabric cannot buckle. Pinching is ineffective for all other non-air-permeable fabrics (2-2 and 2-3).

This experiment demonstrates that different gripping mechanisms are required depending on the air permeability of the fabric and capability of multi-actuation modes in the single structure.

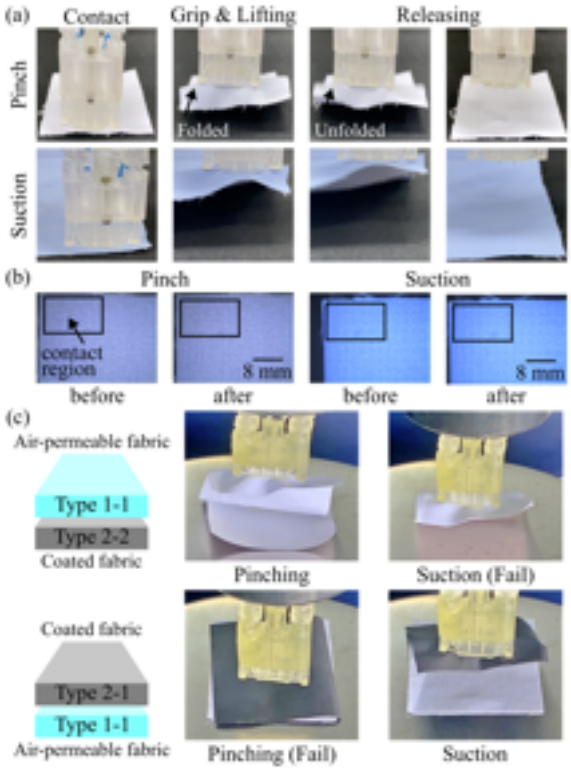

Fig. 3. 19. (a) Operational sequence of the two actuation modes. (b) Comparison of the fabric surfaces before and after gripping showing no noticeable damages for both modes. (c) Results of multi-modes actuation tests with air-permeable and non-air-permeable fabric types.

3.8.2 Pressure response

The pressure response of the gripper is evaluated by measuring the pinching and suction forces as the input pressure increased from -80 kPa to -30 kPa. The repeatability of the gripper structure is assessed by recording pressure changes during repeated cyclic actuation of applying vacuum pressure and releasing inside and outside the membrane. The compensation of the attack angle by compliance of the gripper is demonstrated by positioning the gripper and fabric at various angles from the vertical axis. Lastly, single sheet separation from a stack and picking up only the top sheet are tested.

The time taken to reach the minimum vacuum pressure for each actuation mode is presented in Fig. 3. 20-(a)-top and 3. 20-(a)-bottom. Suction requires 0.67 seconds, while pinching takes 0.65 seconds to reach the minimum vacuum pressure of -80 kPa. To reach -72 kPa, 90% of the minimum pressure, suction and pinching take 0.43 and 0.44 seconds, respectively.

I analyze the hysteresis of the pinching mode, which shows a large deformation of the soft structure compared to the suction mode. The hysteresis phenomenon is inevitable due to using of the compressible fluid for actuation and the elastomer material of the gripper body. I

place red markers in the middle of both fingers at the top of the gripper and track their displacements over time using a motion analysis software (ProAnalyst, Xcitex). Hysteresis phenomenon is observed during operation (Fig. 3. 20-(b)), which however does not lower the performance of the gripper since I use the on-off control between the minimum vacuum pressure (-80 kPa) and zero pressure for pinching.

To determine the maximum suction force, the gripper lifts an object using suction at various pressure inputs. The weight of the object is increased until the gripper could no longer lift it. During the experiment, the gripper approaches, presses, and grasps the object using either actuation mode before lifting it. The relationship between suction force and input pressure is depicted in Fig. 3. 20-(c). The effective area for each pressure is calculated using pressure and weight, and a force prediction model is derived using an average area of 40 mm^2, represented by a dotted line in Fig. 3. 20-(c). The gripper shows the maximum suction force of 3.1 N at the vacuum pressure of -75 kPa, which decreases linearly as vacuum pressure decreases.

The average pinching forces with error bars for different input pressures for fabrics 1-6 and 1-7 are shown in Fig. 3. 20-(d) and 3. 20-(e), respectively. The force is computed using the contact area obtained from the Chapter 3.7.5, the friction coefficient (Table. 3. 4), and initial contact starting pressure (p_0). Two initial pressure values obtained from simulations and experiments are used to calculate the force, represented by blue and black solid lines, respectively. Experimental p_0 values for seven types of air-permeable fabrics ranges between -40 kPa and -35 kPa (between -20 kPa and -15 kPa in simulations). The force calculated using experimental p_0 values shows high correspondence with measured values. Both simulation and experimental results indicate that pinching force is proportional to the

pressure difference. However, there is a significant discrepancy between the two results, as the simulation does not account for the external force acting between the fabric and the floor or the below fabric (Fig. 3. 20-(f)). The friction force increases as the gripper presses the fabric down, interfering with the pinching motion. Thus, pinching occurs at a lower p_0 in the actual experiment than in the simulation.

Fig. 3. 20-(g) shows the maximum holding forces for the seven air-permeable fabrics, obtained from ten trials using a vacuum pressure of -80 kPa. Overall, the experimental values are highly consistent with the theoretical values, except for the fabric 1-3. For the 1-3 fabric, discrepancy occurs since the thickness of the 1-3 fabric (0.58 mm) is thicker than the protruding length of the microneedle (0.25 mm), preventing the needles from fully penetrating and engaging the fabric. In this case, the microneedles could not effectively engage and buckle the fabric, resulting in a lower pinching force. The role of the microneedle is further investigated in an additional experiment.

To evaluate the repeatability of the gripper, 10,000 cycles of applying and releasing vacuum pressures in both suction and pinching modes are conducted (Fig. 3. 20-(h)-left and 3. 20-(h)-right). Each inset plot shows the pressure change of the 5,000-th cycle. In both modes, the minimum pressures are consistent, confirming structural robustness of the gripper finger and the membrane. From the results of the additional experiments, there is no damages at the tip of the microneedles, such as bending or wear, even after 5,000 cycles of actuation (Fig. 3. 20-(i)).

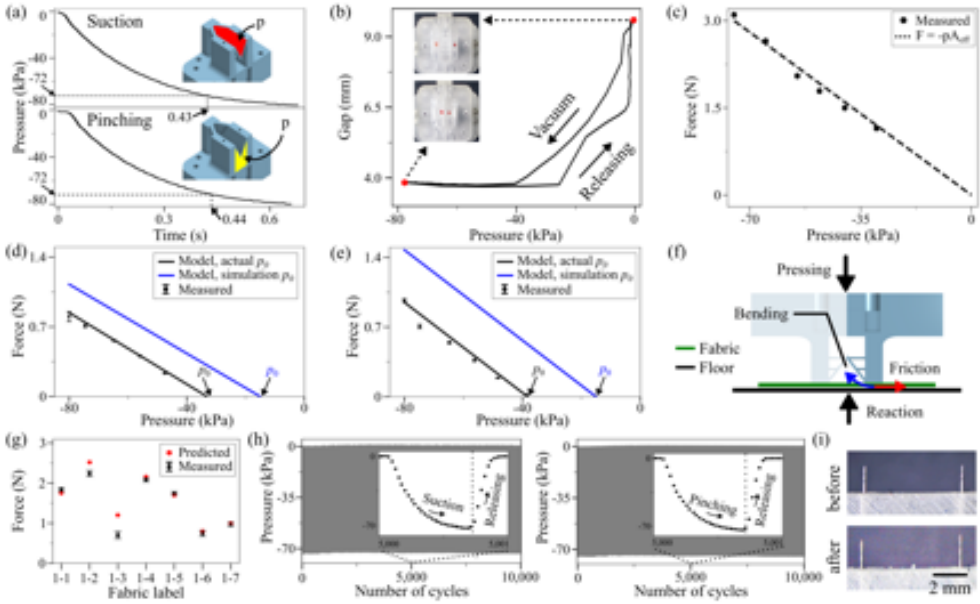

Fig. 3. 20. Experimental results. (a) Pressure responses of suction and pinching. (b) Hysteresis during pinching. (c) Holding force measurements in comparison with model prediction for suction of fabric Type 2. (d) Pinching force measurements in comparison with model prediction for pinching of 1-6 and (e) 1-7 fabrics. (f) External forces during pinching. Friction (Red) hinders bending motion (Blue) of fingertips. (g) Maximum holding force of each air-permeable fabrics. (h) Repeatability test results of suction (left) and pinching (right). (i) Microscopic images of the embedded microneedles before and after 5,000 actuation cycles.

The effect of microneedles on pinching force with fabric 1-7 is investigated (Fig. 3. 21-(a), 3. 21-(b), and 3. 21-(c)). Three conditions are tested: no microneedles, completely embedded needles, and needles protruding 0.25 mm. In all cases, the tip is pressed with a force of 2.5 N, and a vacuum pressure of -80 kPa is applied. The average holding forces measured are 0.53 N, 0.64 N, and 0.97 N for the three

cases, respectively. This demonstrates that microneedles generate larger holding forces, which further increase with needle protrusion.

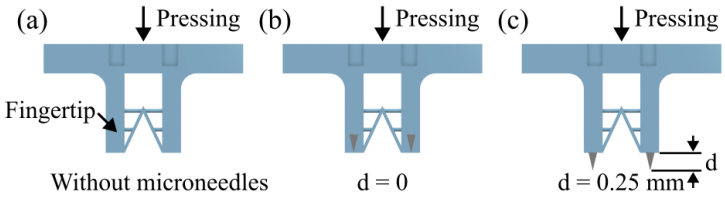

Fig. 3. 21. Simplified schematics of the gripper tip and microneedles. (a) Without microneedles. (b) With microneedles completely embedded and (c) 0.25 mm protrusion.

3.8.3 Single sheet separation

The force exerted by the gripper on the fabric before gripping is a crucial factor for determining successful gripping. Since the appropriate force range for single-sheet separation varies for each fabric, an experiment is conducted to identify this range for air-permeable fabrics (Fig. 3. 22-(a)). For all tested fabrics, single-sheet separation is possible within the 0-3 N range. For the 1-1 fabric, a pinching experiment is performed with different pressing forces (Fig. 3. 22-(b)-i, 3. 22-(b)-ii, and 3. 22-(b)-iii). The fabric cannot be picked up with pressing force below the suggested range, and multiple fabric sheets are lifted if the force exceeded the range.

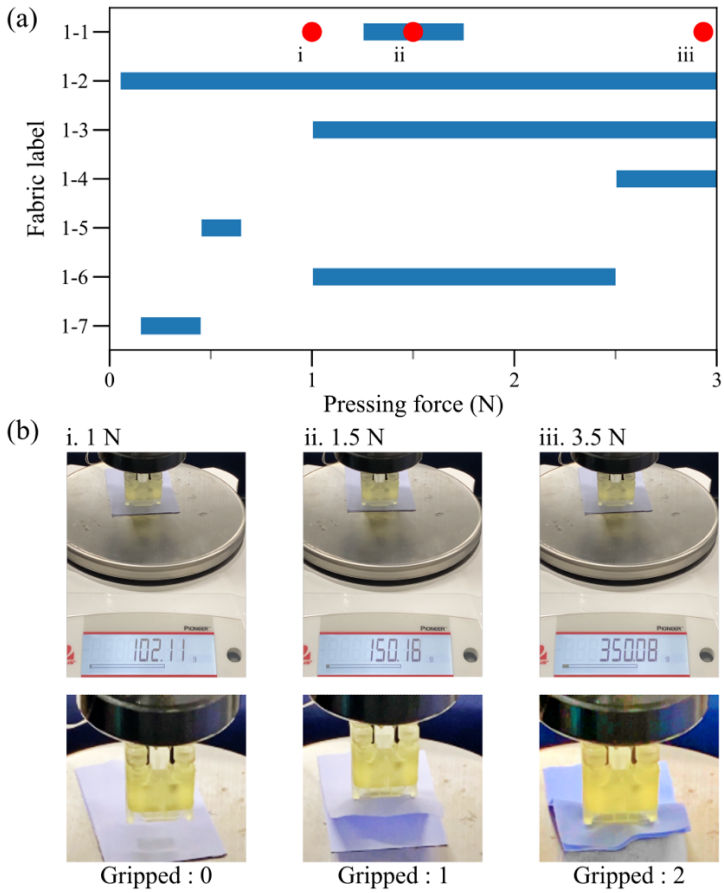

Fig. 3. 22. (a) Force range to separate single sheet of air-permeable fabric. (b) Gripping results with pressing force of i. 1 N, ii. 1.5 N, and iii. 3.5 N.

Based on these specific pressing force ranges, single-sheet separation is conducted for all fabric types, including both the air-permeable and the non-air-permeable fabrics, and the results are shown in Fig. 3. 23. With suction, single-sheet separation is successful in all 50 trials without failures. However, pinching the air-permeable fabrics results in success rates ranging from 70% to 100%. The primary causes of failures are microneedles penetrating multiple fabric sheets and entanglement on the edge of the fabric. Since the second

case depends on fabric quality of processing rather than gripper performance, only the first case is considered a functional failure. Other factors influencing the success rate included fabric thickness and pressing force range. The thicker the fabric and the larger the pressing force range, the higher the success rate. The 1-5 and 1-7 fabrics, which display the lowest success rates, have failures 15 and 8 times out of 50 trials, respectively. However, 12 out of the 15 failures for the 1-5 fabric and 6 out of the 8 failures for the 1-7 fabric are functional failures due to the penetration of the microneedles. The other fabrics show higher success rates, averaging 93%.

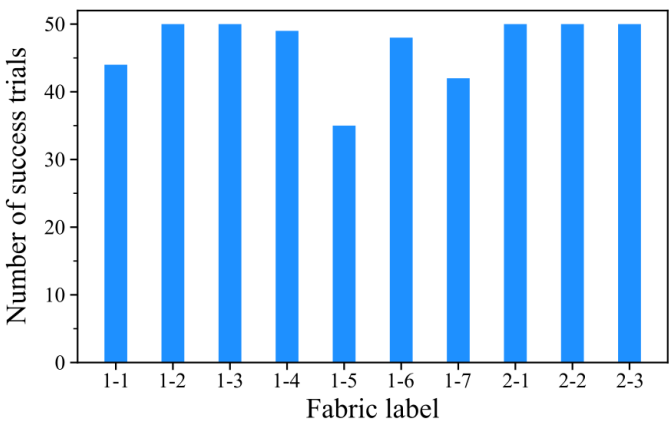

Fig. 3. 23. Single sheet separation result. Pinching and suction modes are used for Type 1 and Type 2 fabrics, respectively. Each represents the number of successes out of 50 trials.

3.8.4 Compliant structure

Compensation of an attack angle by compliant structure of the gripper is tested with different attack angles from −15° to +15°

along the x- and y-axes in increments of 2.5° (Fig. 3. 24-(a)). The gripper can successfully lift the fabric to an inclination of ±10°, as shown in Fig. 3. 24-(b) and 3. 24-(c). This indicates that the integrated compliant structure of the gripper offers stable contact under load and permits gripping even when the contact is not perfectly perpendicular to the fabric. When the same experiment is conducted a gripper without the compliant structure, pinching is successful only within a range of ±2°.

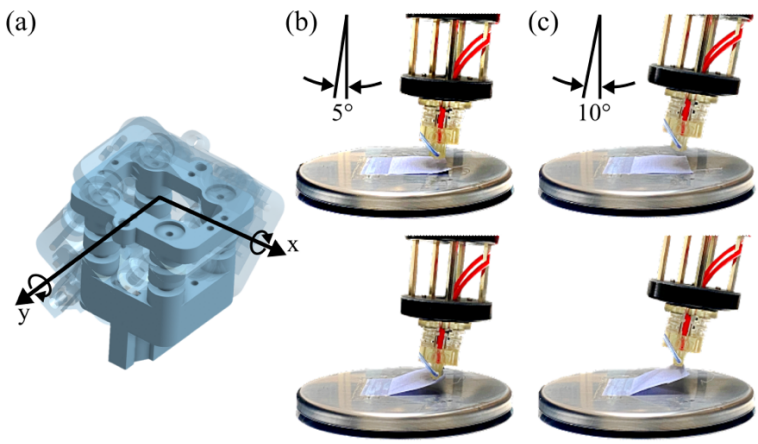

Fig. 3. 24. (a) Contact experiment with angles. (b) Picking up fabric at attack angles of 5° and (c) 10° from the vertical axis.

Additionally, the compliance of the gripper body protects the fingertips from damage or deformation under excessive load. Since the gripper typically operates with pressing forces below 3 N, forces greater than this are considered excessive. Deformation in the fingertips of the gripper is observed while applying forces up to 50 N (16 times the normal pressing force), as shown in Fig. 3. 25-(a) through 3. 25-(d). Due to the compliant structure, no significant bending or tearing is observed, and the gripper tip maintains stable

vertical contact with the surface of the fabric. Further investigation is conducted to find the functional boundary of the compliant structure. I apply the vertical loads using a tensile tester (Mark-10) and a flat indenter, imitating the pressing force. When the pressing force of larger than 55 N is applied, the fingers of the gripper is significantly deformed (Fig. 3. 25-(e)), making the gripper not functional properly for pinching. However, after releasing from the pressing, the gripper returns to its original state without any damages or deformations (Fig. 3. 25-(f)). In contrast, the gripper without compliant structure shows considerable fingertip deformation when subjected to pressing forces of 20 N or higher. This value becomes smaller if the contact with the surface is not vertical, causing structural deformation even below 10 N.

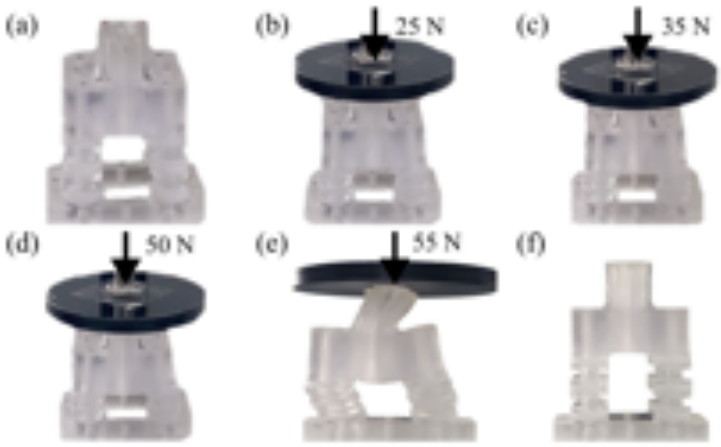

Fig. 3. 25. Proposed soft gripper (a) before being pressed, with pressing forces of (b) 25 N and (c) 35 N, (d) 50 N. (e) Pressing force of 55 N and (f) released from the pressing.

3.8.5 Characterization of pressure sensor

A barometric pressure sensor is connected to the air cover for contact detection and pressing force control. As discussed in Chapter 3.7.4, an experiment is conducted to determine the relationship between the pressing force and the change in height of the gripper. The sensor is characterized by its response to continuous force inputs, and its repeatability is assessed through a cyclic test.

The gripper is placed on the tensile tester (Mark-10) and pressed with a flat indenter by 2 mm. This travel distance generates a pressing force up to 5 N, covering the range of pressing force (3 N) required for single-sheet separation. The relationship between pressing force and gripper height change is depicted in Fig. 3. 26-(a), with corresponding pressure measurements shown in Fig. 3. 26-(b). The force measurement shows higher hysteresis during loading and unloading processes than the pressure readings. Consequently, Δh is estimated based on measured pressure readings using the relationship presented in Eqn. 9 and compared to experimental results (Fig. 3. 26-(b)). The model, based on Boyle's law, offers a reliable estimation of actual pressure readings. Moreover, pressing force can be estimated using pressure sensor measurements and the results of Fig. 3. 26-(a).

The repeatability of the sensor is also evaluated by cyclic tests. Starting from a no-load initial state, the gripper tip is pressed down by 2 mm and released over 1,000 cycles (Fig. 3. 26-(c)). During the cyclic test, the gripper shows consistent changes in pressing force and internal pressure, demonstrating the structural robustness of the gripper and the fully sealed compliant posts during testing. Fig. 3. 26-(d) displays a sample of force and pressure profiles during the test.

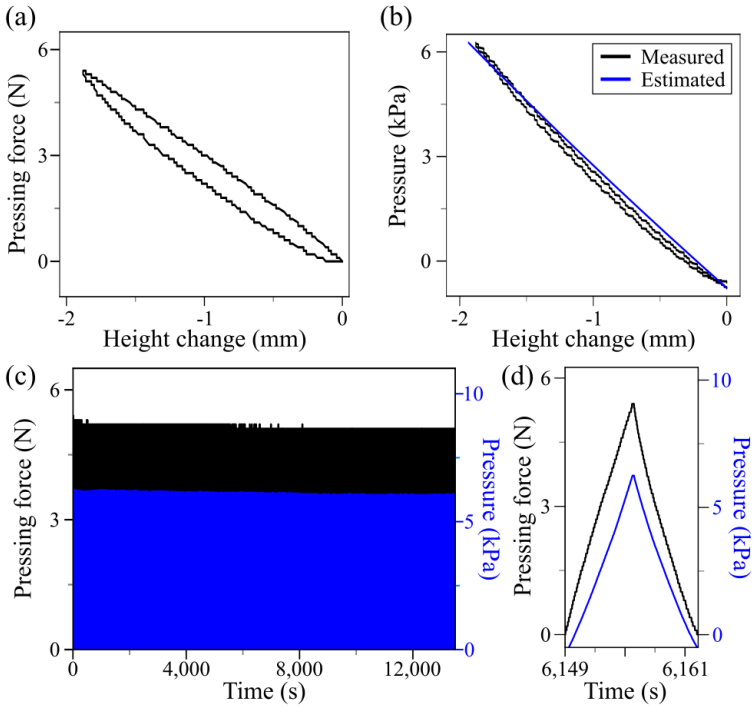

Fig. 3. 26. Experimental results of barometric pressure sensor. (a) Measured force as the height of the gripper changes. (b) Measured pressure as the height of the gripper changes and comparison between height estimation (Blue) and actual measurement (Black). (c) Result of the cyclic test. (d) Force and sensor responses at 500-th cycle.

3.9 Demonstration

I evaluate the proposed gripper in an application involving the automatic sensing, control of fabric sheet, and picking up. The gripper is mounted on the industrial robotic arm (UR5e), and the air source is connected to both the pinching and suction chambers of the gripper through vacuum regulators (ITV2090, SMC). The 1-1 fabric is placed

on a flat surface, and the gripper presses the fabric before lifting. When the force estimated by the pressure sensor reaches 0.5 N, contact is recognized. Then, a vacuum pressure of −80 kPa is applied to the suction chamber to assess the permeability of the contact fabric. The vacuum pressure is measured by the vacuum regulator. All air-permeable fabrics show pressures higher than −72 kPa, while non-air-permeable fabrics show pressures between −80 and −72 kPa. A threshold of −72 kPa, representing 90% of the applied vacuum pressure, is chosen to autonomously determine the air permeability. In Fig. 3. 27-(a), the measured pressure is −67 kPa, indicating contact with an air-permeable fabric. Then, the gripper is pressed until the measured force reaches 1.35 N based on the pressure sensor, which is the force level for single-sheet separation of the 1-1 fabric (Fig. 3. 22-(a)). The pinching sequence is depicted in Fig. 3. 27-(c). A non-air-permeable fabric (2-1) is tested using the same procedure (Fig. 3. 27-(b)). In this case, a vacuum pressure of −77 kPa is measured as the decision value for non-air-permeable fabrics. After determining the air permeability of the fabric, vacuum suction mode is chosen, and the gripper successfully lifts the fabric. Since the gripping performance for non-air-permeable fabrics is not affected by additional pressing force, the same force of 1.35 N is used for suction. In this application, the gripper demonstrates effective gripping and separation of individual sheets without human intervention or prior knowledge of the fabric (e.g., thickness).

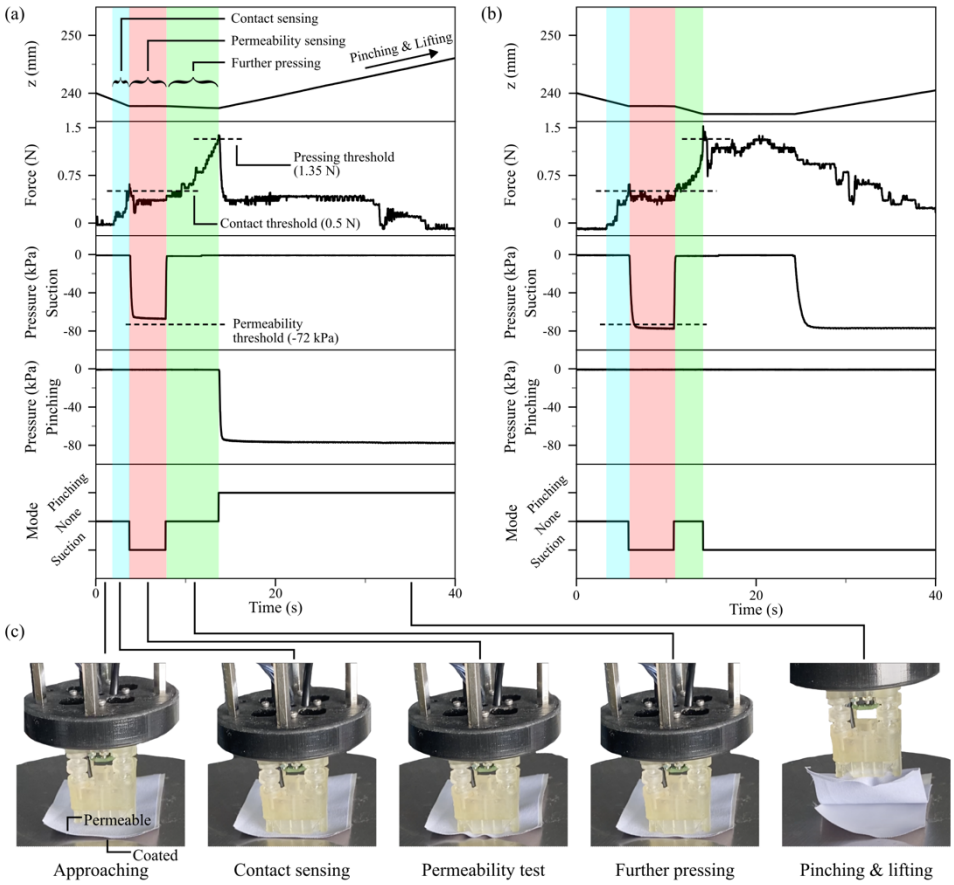

Fig. 3. 27. Automatic fabric handling using proposed gripper system. (a) Sequence of picking up air-permeable fabric placed on coated non-air-permeable fabric. (b) Sequence of picking up coated non-air-permeable fabric. (c) Actual images of pinching sequence.

3.10 Discussion

The primary contribution of this research is the development of a soft gripper, comprised of a single structure, that performs two actuation modes for robotics manipulation of an unstructured and highly flexible fabric. The gripper has two distinct gripping

mechanisms and operates depending on the target fabric type: pinching for air-permeable porous fabrics and suction for non-air-permeable coated fabrics. Bellow-shaped compliant posts provide structural compliance, allowing the gripper to easily conform to the fabric surface, ensuring stable contact. Successful gripping can be achieved even if the attack angle is not perfectly perpendicular to the fabric surface, significantly simplifying the control algorithm and the gripper installation process. The integrated barometric pressure sensor detects contact and controls the pressing force, enabling autonomous operation and preventing excessive load. Additionally, the 3D-printed gripper body makes easy microneedle replacement using the needle holder, easy fabrication, and maintenance in practical applications. Robotic handling system with the proposed gripper demonstrates considerable potential for automating garment manufacturing.

Despite its numerous advantages, there is still room for improvement in design and function. To enhance robustness and autonomous fabric handling, an additional function could be integrated to monitor the single sheet separation. This may be achieved by adding capacitive sensors to the tip of the gripper to measure the fabric thickness held between the fingertips. Single sheet separation performance could also be improved by actively controlling the protruded microneedle length for various fabric thicknesses. Since thin fabrics requires shallow penetration by microneedle to engage only the top layer, the protruded length of the microneedle needs to be dynamically controlled depending on the target thickness of the fabric. This provides flexibility in selecting the pressing force within the range shown in Fig. 3. 22-(a). To further increase robustness and repeatability, an additional air port is needed to the air cover for

connecting to a solenoid valve. This allows exhausting of the residual pressure of the air chamber to ambient pressure after each actuation cycle. Additionally, the resolution of the integrated pressure sensor can be enhanced by employing a more precise sensor, enabling detection of subtle weight differences, such as the number of fabric sheets lifted.

The proposed gripper features a unique design for multi-actuation, compliance, and sensing, which enables handling various fabrics, single-sheet separation, and autonomous operation. Moreover, the gripper is consistency in quality by using 3D printing. By handling fabrics through the proposed gripper, I expect that the gripper contributes to the realization of a smart manufacturing environment by enabling physical connections between processes.

Chapter 4. Soft Modularized Robotic Arm for Safe Human-Robot Interaction Based on Visual and Proprioceptive Feedback

4.1 Backgrounds

Industry 5.0 represents a human-centric smart production environment in which humans occupy a dominant role in the manufacturing process [15]–[17]. In this environment, robots serve as assistants to human production activities and creativities, and cooperation between humans and robots is emphasized. Compared to the straightforward, repetitive automated production environment characterized by Industry 4.0, there are increased interactions between humans and robots, and robots are required to perform more complex and diverse tasks than before [8], [67], [139]. Consequently, a focus on safe collaboration between humans and robots and the dexterity of the robots is essential.

For safe human-robot interactions and dexterous manipulation, continuum manipulators or soft robotic arms made of soft bellows actuators have been studied, and bellow-type artificial muscles have been widely used for their capabilities of large displacement and bi-directional actuation [140]–[143]. In addition, the innate safety of soft materials makes the robots safe even in the case of collisions with

humans, and their large degrees of freedom allow for complex and diverse motions for manipulation. However, the bellows that drive the robotic arms are in general made with a manual process by molding and casting or by thermal bonding of fabric and elastomer materials, making the fabrication process complicated and difficult to control the quality of the device.

To simplify the fabrication process and overcome the issue of relatively large manufacturing tolerance, recently advanced 3D printing technologies have been employed to fabricate the complex structure of the bellow at once [144]–[148]. There have been studies on continuum manipulators composed of 3D-printed bellow actuators [146], [149]–[151].

In this study, I propose a modularized soft robotic arm with integrated sensing of human touches for physical human-robot interactions (pHRI). The proposed robot is composed of multiple soft manipulator modules connected in series, and each module consists of three bellow-type soft actuators, pneumatic valves, and an on-board sensing and control circuit.

For closed-loop control of the soft manipulators or arms (Fig. 4. 1-(a) and 4. 1-(b)), wire encoders [57], [152], [153]. Other Studies have combined the kinematics of the robot with the motion data from cameras or motion capture systems [56], [58], [63]. Despite the simplicity of the system, wire encoders, that directly measure the displacements do not usually provide compact form factors, making it difficult to modularize the robot. In addition, the tension of the string sometimes interrupts the operation of the manipulator. On the other hand, motion capture systems can track 3D positions of the robot accurately without any physical interferences. However, they can be applied only in controlled environments with cleared surroundings,

resulting in limited applications of pHRI.

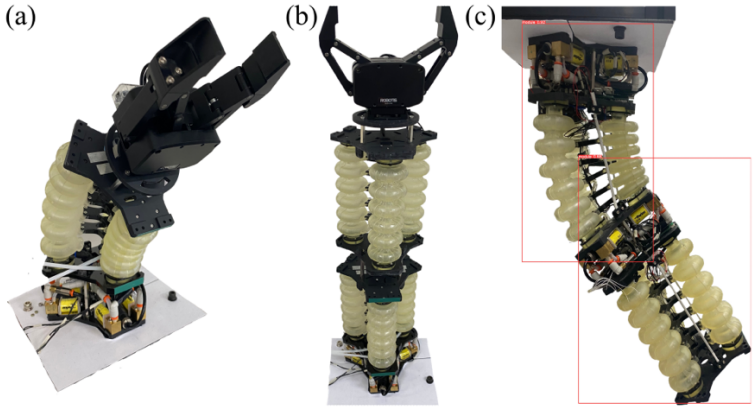

Fig. 4. 1. Soft robotic arm made of manipulator modules composed of bellow-type soft actuators. (a) Single- and (b) double-module manipulators with a gripper. (c) Pose and motion detection of the soft robotic arm.

Studies on soft strain sensors that could overcome the limitations (Fig. 4. 2) of the wire encoders have been conducted [154], [155]. Omnidirectional strain sensor has also been proposed [156], [157]. By embedding microchannels filled with room-temperature liquid conductors in an elastomer matrix, axial strains or displacements can be easily detected based on the change in electrical resistance of the microchannels [158]. Automated processes, such as direct writing or printing, have recently developed for fabrication of liquid-conductor microchannels [159]–[161].

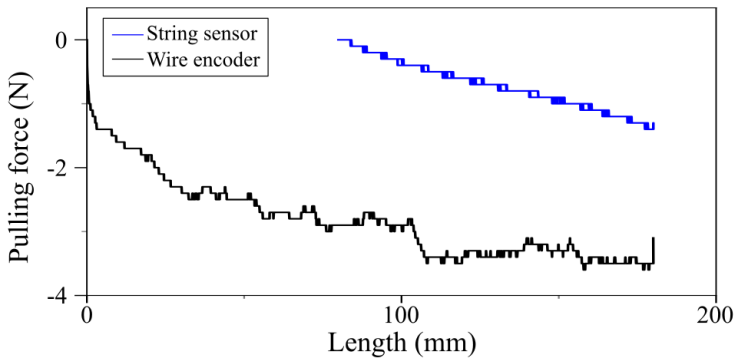

Fig. 4. 2. Force measurement results. Maximum pulling forces are 1.4 N for string strain sensor and 3.5 N for wire encoder (CWPS1000V1, CALT), respectively. Mass of the string sensor is 2.89 g and the wire encoder is 340 g.

With the development of optical equipment, it is possible to obtain 3D images using a depth measurement camera (RealSense L515, Intel). Although the accuracy is not as good as motion capture systems [162], it has an advantage of simplicity in system construction and reconfiguration, since it requires only a single camera. When combined with machine learning techniques, it is possible to recognize and track target objects in a 3D space in near-real time [93], [163] (Fig. 4. 1-(c)).

I combine these two technologies with deep learning for localization and control of the proposed soft robotic arm. However, it is also required to detect contacts with humans for autonomous and interactive operations. Thus, I directly embed a triboelectric nanogenerator (TENG) in each bellow actuator as a tactile sensor specialized for detecting human touches.

A TENG converts a mechanical touch to electrical energy based on coupling of contact electrification and electrostatic induction [164], [165], and the electrical energy is used as a sensing signal for

interaction between the human and a robot. The TENG sensor has a simple structure that consists of only a pair of conductive and dielectric layers, making it easy to be embedded or integrated into a structure without any major modification of the host system. To provide compliance for the structure, ionic hydrogel was used as the conductive layer. In this layer, ions dissolved in the gel act as charge carriers [166], [167], and hydrogel made of organogel with reduced evaporation is used [168]–[170].

In this study, I first propose a bellow-type soft actuator for the soft robotic arm. The actuator has an air chamber for actuation and embedded channels on the wall for TENG touch sensing. The entire structure of the actuator with these complex features is built by stereolithography (SLA) 3D printing that enabled simple fabrication with consistent quality.

I then propose a modularized design of the soft robotic arm. For modularity, I design a custom manifold and a control circuit that integrates all the electronic components. In this way, each manipulator module becomes a complete system as itself and can be operated independently. When connected in series, multiple manipulator modules form and act like a single robotic arm. The modular design also makes it easy to assemble the modules since they have the same components and are made by the same fabrication process. Furthermore, having the manipulator modules of the same shape has an advantage of implementing only a single trained model for detecting their motions.

I also propose a method of localization and control of the robotic arm using omnidirectional soft string sensors. The proposed sensor is extremely lightweight and has a compact form factor compared to a commercial wire encoder. It is possible to estimate the pose of the

robotic arm with low computational power. By combing the data from the soft sensor data, the depth camera with a deep learning model, we were also able to localize and control the position of the end-effector in real time.

Finally, I provide a method not only for recognizing external contacts using the tactile sensors and the string sensors, but also for detecting and localizing human contacts using the TENG sensors.

4.2 Design

The manipulator module consists of 3D-printed soft bellow actuators, soft sensors, and an inertial measurement unit (IMU) to measure and estimate the length and the pose of the module, a pneumatic system to deliver air pressure to each module, and a control circuit (Fig. 4. 3-(a)). All the components were fixed at the base structure, and the soft bellows were connected to the bases thorough 3D-printed circular rings to prevent stress concentration on the soft part.

4.2.1 3D-printed tribo-sensitive soft bellow

The triboelectric voltage generator is embedded in the bellow to recognize and localize external contacts. Since the amount of voltage generation is related to the contact area [171], I design a 3D printable bellow structure that secured a large contact area. The outer radius

of the bellow is designed to maximize the actuation range while maintaining the printability. The total length of the bellow actuator is 171.5 mm, with an active region of 141.5 mm. Both convex and concave areas of the bellow have the same curvature radius of 8.25 mm, and four channels are embedded for organogel (Fig. 4. 3-(b)). Four ports (diameter 2.2 mm) were made on the bellow to inject the organogel into the channel at the top. Each channel has vent holes, allowing residual resin after printing to be discharged. The outer wall thickness is 4 mm, and the depth of the embedded channel is 1.5 mm (Fig. 4. 3-(b)-i). The channel depth is selected considering the structural stiffness and the clogging during printing.

The minimum width of the TENG channel is 3.8 mm and located at the concave part of the bellow. The three actuators in one module are mechanically coupled in parallel through structural constraints (Fig. 4. 3-(b)-ii). When the bellows are fixed only at the top and the bottom, pure bending motion is impossible as the bellows will buckle when actuated. The maximum width of the channel is 8.7 mm and located at the outer convex part. This part is designed to have as large area as possible, for easy detection of external contacts. Four channels are placed to cover a range of 140°. The maximum width between two adjacent channels is 7.7 mm. The bellow actuator has the minimum cross-section area at the concave areas with structural weakness. By adding reinforcement to this part, the stability of printing and the strength of the bellow are increased (Fig. 4. 3-(b)-iii).

4.2.2 Modular design

The control system is designed to generate the required pneumatic pressure to actuate the bellows within the manipulator module, while also delivering pneumatic power to other manipulator modules. Six proportional solenoid valves (VSO series 11, Parker) are mounted to control the input pressure, and they are connected by a custom-built (by 3D printing) manifold to minimize the mass, and compressed air is transmitted to the next manipulator module through the coiled tube at the top port (Fig. 4. 3-(c)).

A custom-designed circuit board is installed to control the manipulator module. The board consists of a current driver for the solenoid valve, a circuit for power delivery, and circuits for acquiring and processing the signals from the tactile sensors and string sensors, and a port to communicate with the IMU (WitMotion, WT901). A wireless communication unit (LOLIN D1 mini, WeMos) is installed to make the entire system untethered. To measure the pressure of the bellow, pressure sensors (XGZP6847-040KPG, CFSensor) are installed in the middle (Fig. 4. 3-(d)).

The manipulator module needs a positive pressure for actuation but has an ejector to generate a negative pressure for contraction of the bellow (Fig. 4. 3-(e)).

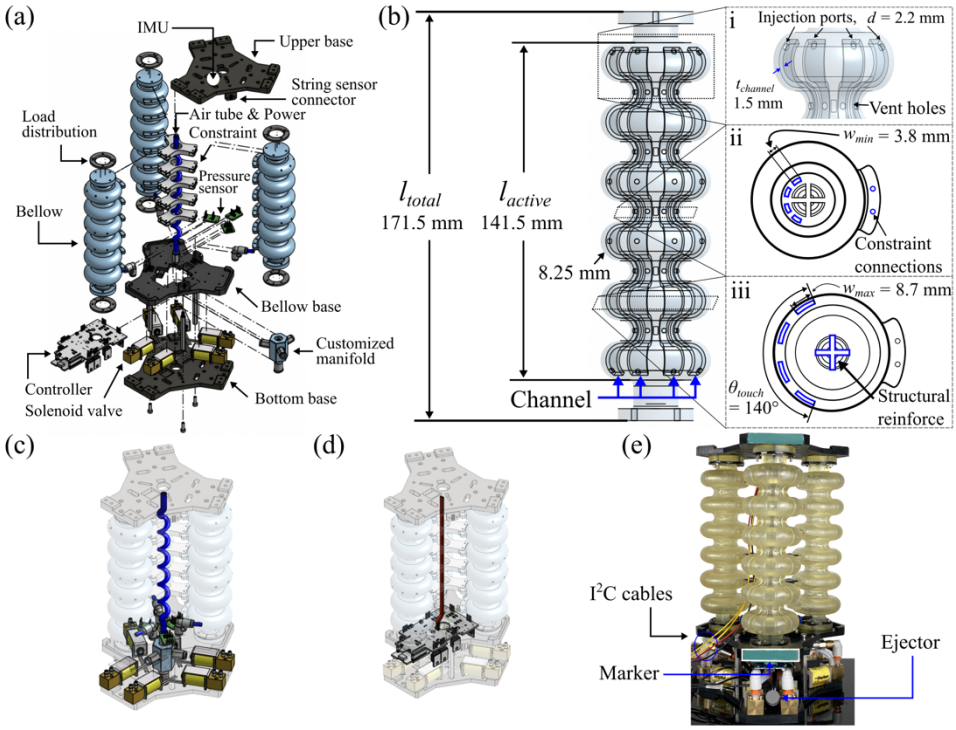

Fig. 4. 3. (a) Exploded view of manipulator module. (b) Design of the bellow soft actuator and configuration of the major components: i. Embedded channels for TENG tactile sensing and ii. and iii. cross-sectional views of the actuator showing the maximum and minimum channel sizes. (c) Pneumatic pressure control system with valves, a manifold, and a coiled tube. (d) Electronic system for wireless communication, sensing, power delivery, and control of the manipulator module. (e) Actual photo of an assembled manipulator module with additional components.

4.2.3 Material selection

The bellow is printed with a photopolymer resin (Elastic 50A, Formlabs) with the lowest shore hardness of 50A and the maximum

strain of 160%. This material is soft enough for safe pHRI and capable of tolerating large enough strains without failures during repeated operations. It also shows a fast shape recovery rate after actuation. The other parts are made of rigid materials (Clear and Black, Formlabs).

Organogel is fabricated using acrylamide (AAm; Sigma, A8887) and N,Nmethylenebisacrylamide (MBAAm; Sigma, M7279) as a monomer and a crosslinker, respectively. Ethylene glycol (EG; DAEJUNG, 4026-4105) is used as a liquid constituent and Lithium phenyl-2,4,6trimethylbenzoylphosphinate (LAP; Sigma, 900889) is used as a photoinitiator. Lithium chloride (LiCl; DAEJUNG, 5086-4405) is used as ionic charge carriers. Trichlorosilane (Heptadecafluoro-1,1,2,2-tetrahydrodecyl) (HDFS; JSI Silicone Co., H5060.1) is used as a surface perfluorination agent.

The soft string strain sensor is made of highly stretchable elastomer (Ecoflex-0030, Smooth-On). Since the manipulator module has a height ranging from 100 mm to 200 mm, the soft string sensor is fabricated with an initial length of 90 mm and prestrained. Ecoflex-0030 is chosen as it easily stretches to the strain of 150% or more, and the stress applied under this range is low [137].

4.3 Fabrication

4.3.1 Tribo-sensitive soft bellow

The bellow actuator is made of relatively complex structure with different features, such as curvatures, channels, and connectors. I fabricate this structure using a SLA 3D-printer (Form3, Formlabs) (Fig. 4. 4-(a)). Since the width of the embedded channel is small, residual resin has to be removed after printing, and it is done by blowing compressed air through the open port of the channel and rinsing the channel using isopropyl alcohol. Afterwards, the bellow is cured to complete the post process (Form Cure, Formlabs). Printing the bellow horizontally rather than vertically increases the printed area of each layer, and stronger bonding between neighboring layers reduced delamination when the bellow is stretched [172].

The 3D-printed bellow is treated air plasma under vacuum for 30 seconds to form hydroxyl terminations on the surface (EQ-PCE-3, MTI Corp.) (Fig. 4. 4-(b)). The surface-activated bellow is immersed in an HDFS solution dissolved in hexane at a 1:300 mixing ratio (Fig. 4. 4-(c)). Self-assembled monolayer formation is carried out for 30 minutes [169]. The treated surface is then rinsed with hexane for 10 minutes. An organogel precursor solution, composed of 3.5 M AAm, 1.5 M LiCl, 0.17 mM LAP, and 8 mM MBAAm, is injected into the bellow (Fig. 4. 4-(d)) and polymerized under 400 nm ultraviolet irradiation in a curing device (Form Cure) for 10 minutes (Fig. 4. 4-(e)).

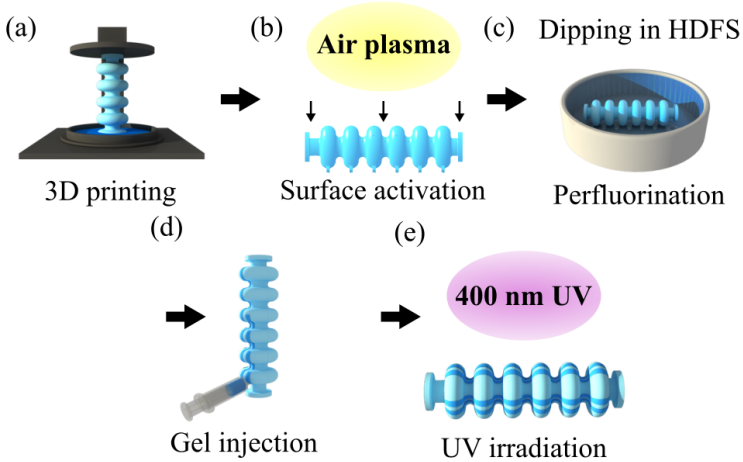

Fig. 4. 4. Fabrication process. (a) 3D printing of the bellow structure. (b) Plasma treatment. (c) Dipping in HDFS for amplifying the triboelectric effect. (d) Injecting organogel precursor solution into embedded channels. (e) UV treatment for curing of organogel.

4.3.2 Soft string strain sensor

To measure the length and to estimate the position of the manipulator module, I develop and use the soft string strain sensor. A liquid metal trace is directly printed on a silicone substrate, and the length is estimated using the resistance change when the manipulator module is actuated.

The string sensor is fabricated with the following procedures. First, a thin layer of liquid-state Ecoflex-0030 is spread using an applicator (Elcometer 4340, elcometer®) and cured. Liquid-metal (eGaIn) trace is printed on the cured silicone substrate using a motorized $x-y-z$ stage (Shotmaster 300ΩX, Musashi), a pneumatic dispensing system (SuperΣ CMIII V2, Musashi), and a laser distance sensor (LK-G32, Keyence) (Fig. 4. 5-(a)). Then, the printed liquid-metal trace is

covered with another layer of Ecoflex-0030, and the signal are connected (Fig. 4. 5-(b)). The sensor is cut and placed on a flexible plastic sheet. This sheet is then rolled into a cylindrical shape (Fig. 4. 5-(c) and 4. 5-(d)). Liquid-state Ecoflex-0030 is injected into the center of the rolled sheet (Fig. 4. 5-(e)) and cured. The flexible sheet is then removed to complete the string sensor with a diameter of 4.5 mm and a length of 90 mm. 3D-printed rigid parts are added to both ends of the sensor for mechanical connection with the manipulator module.

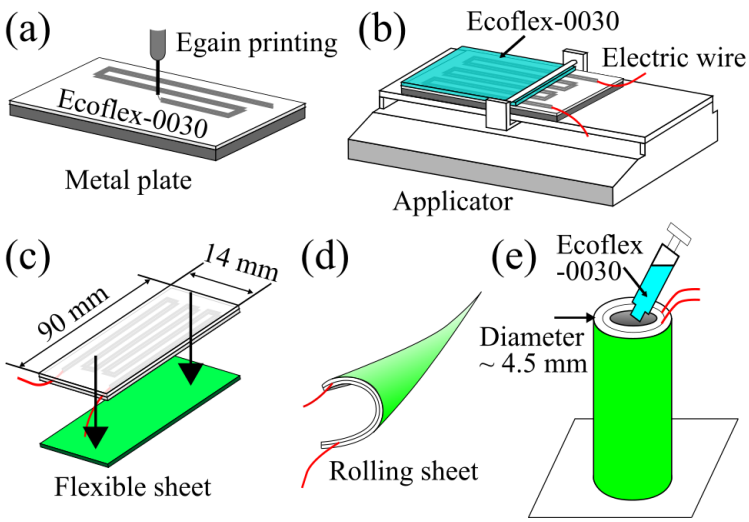

Fig. 4. 5. Fabrication process of soft strain sensor. (a) Direct printing of a liquid-metal trace on a silicone substrate. (b) Encapsulation of the printed trace with another layer of elastomer and wire connection. (c) Transferring the flat sensor on a flexible sheet. (d) Rolling up the sensor to a thin cylinder. (e) Filling the center void with liquid-state silicone and curing.

4.4 Modeling

The bellow actuator contracts or expands depending on the air pressure applied to the chamber. Combinations of single-axis motions of three actuators enables linear and bending motions of the manipulator module. I model the pressure response of the manipulator module in 3D space and the inverse kinematics for calculating the required internal pressure for the manipulator to reach the desired point in the space.

The general method for solving the linkage system of a rigid body by considering contraction and expansion with the changes in link length, is not suitable for a soft body. The analysis is more complex since continuous linear deformation and bending occur in all the elements constituting the body. One approach to simplify this complex system is to assume the manipulator module has a constant curvature [173].

4.4.1 Forward kinematics

In the assumption of constant curvature, the pose of the manipulator module is described with respect to the center point of both ends. The posture is determined by the arc lengths l_1, l_2, and l_3 of the three bellows. These lengths are variables in the actuator space ($\boldsymbol{q} = [l_1, l_2, l_3]^T$) and are used to calculate transformation into configuration space.

Factors affecting the bellow length include the internal pressure,

geometrical parameters of the bellow, and the material property of the bellow. According to Hooke's law, the pressure p_i applied to the i-th bellow causes the length change and the arc length of the i-th bellow can be expressed as:

$$\Delta l_i = \frac{p_i A_{eff}}{k_i}, \tag{10}$$

$$l_i = \Delta l_i + l_0 + f(p_i'), \tag{11}$$

$$f(p_i') = a_1 p_i' + a_0, \tag{12}$$

$$p_i' = p_i - \min(p_1, p_2, p_3), \tag{13}$$

where Δl_i is the deformed length of the i-th bellow, A_{eff} is the effective cross-sectional area of the bellow, l_i is the arc length, l_0 is the initial length of the active region, k_i is the structural stiffness, and $f(p_i')$ is a first-order fitting function adjusts the arc length between predictions by simulation and Hooke's law. a_0 and a_1 are the coefficients of the adjust function, and p_i' is $p_i - \min(p_1, p_2, p_3)$. p_1, p_2, and p_3 are the pressures of the three actuators, respectively.

When all three pressures are the same (Fig. 4. 6-(a)), $f(p_i')$ becomes zero in the Eqn. 12, so only translational motion is considered. In the case of bending, the sequence is divided into two (Fig. 4. 6-(b)). Translation occurs first due to $p_{\min}$, and then bending occurs due to the difference $p_i - p_{\min}$. Since the strain energy by the input pressure will be equal to the sum of the axial and the bending strain energies, different pressures of bellows indicate the bending strain energy. In this case, the axial strain will be reduced, and as a result, the arc length will be increased, as in Eqn. 11. The stiffness k_i is determined through simulation based on the bellow geometry and the material properties [174].

The configuration spaces of the module l_c, ϕ, and κ are then

determined by the actuator space variables l_i [173].

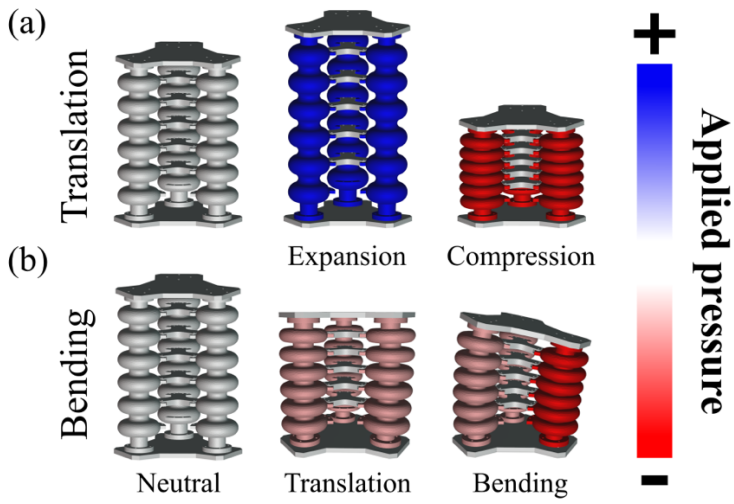

Fig. 4. 6. Two actuation modes of the manipulator module: (a) Linear translation and (b) bending in sequence.

$$l_c(\boldsymbol{q}) = \frac{l_1+l_2+l_3}{3}, \tag{14}$$

$$\phi(\boldsymbol{q}) = \tan^{-1}\left(\frac{\sqrt{3}(l_1+l_2+l_3)}{3(l_2-l_3}\right), \tag{15}$$

$$\kappa(\boldsymbol{q}) = \frac{\sqrt{l_1^2+l_2^2+l_3^2-l_1l_2-l_1l_3-l_2l_3}}{d(l_1+l_2+l_3)}, \tag{16}$$

$$\theta(\boldsymbol{q}) = l_c(\boldsymbol{q})\kappa(\boldsymbol{q}), \tag{17}$$

where l_c is the arc length between the center points of the top and the bottom, ϕ is the angle formed about x axis when the center point on the top is projected on $x-y$ plane, κ is the curvature of the manipulator module, d is the distance between the center point on the top and the center of each bellow, and θ is the angle formed by the arc segment with $x-y$ plane.

From the configuration spaces, the top center position is determined through the geometrical relation [175]. The manipulator module has interfaces for connection to the next module at the top and the bottom. These are passive structures that are not affected by the pneumatic actuation, and so can be modeled as:

$$c = 2\rho \sin\left(\frac{\theta}{2}\right), \tag{18}$$

$$x_c = \mathrm{c} \sin\left(\frac{\theta}{2}\right) \cos\phi + l_u \sin\theta \cos\phi, \tag{19}$$

$$y_c = \mathrm{c} \sin\left(\frac{\theta}{2}\right) \sin\phi + l_u \sin\theta \sin\phi, \tag{20}$$

$$z_c = \mathrm{c} \cos\left(\frac{\theta}{2}\right) + l_b + l_u \cos\phi, \tag{21}$$

where c is the chord length, ρ is the radius of curvature, l_u and l_b are lengths of the passive structures at the top and the bottom, respectively, and x_c, y_c, and z_c are Cartesian coordinates of p_c (Fig. 4. 7).

4.4.2 Inverse kinematics

In this study, inverse kinematics is used to determine the length of each bellow from a given point $p(x, y, z)$ in the task space, and to find the input pressure p_i using the length and Eqns. 11 to 13. The inverse kinematics is solved based on the coordinates of the point p rather than p_c for convenience of calculation (Fig. 4. 7). Alternatively, it is possible to use position p_c and the circular reference in the calculation. The relationship of the configuration space parameters, the lower passive height l_b and the coordinates of the given point $p(x, y, z)$ is as follows [173], [175]:

$$\phi = \begin{cases} \tan^{-1}(y/x) & \text{if x} > 0, \text{y} > 0 \\ 2\pi - \tan^{-1}(y/x) & \text{if x} > 0, \text{y} < 0 \\ \pi + \tan^{-1}(y/x) & \text{if } x < 0 \end{cases}, \tag{22}$$

$$\kappa = \frac{2\sqrt{x^2+y^2}}{x^2+y^2+(z-l_b)^2}, \tag{23}$$

$$\theta = \begin{cases} \cos^{-1}(1 - \kappa\sqrt{x^2+y^2} & \text{if z} > 0 \\ 2\pi - \cos^{-1}\left(1 - \kappa\sqrt{x^2+y^2}\right) & \text{if } z \leq 0 \end{cases}, \tag{24}$$

$$l = \frac{\theta}{\kappa}, \tag{25}$$

$$l_i = l - \theta d\left(\frac{2\pi}{3}(i-1) + \frac{\pi}{2} - \phi\right), \qquad i = 1, 2, 3 \tag{26}$$

From the above equations, the top center point $p_c(x_c, y_c, z_c)$ is determined as:

$$x_c = x + l_u \sin\theta \cos\phi, \tag{27}$$

$$y_c = y + l_u \sin\theta \sin\phi, \tag{28}$$

$$z_c = z + l_u \cos\theta, \tag{29}$$

By combining Eqns. 2, 3, and 4, the deformation Δl_i of the i-th bellow and the corresponding internal pressure p_i are determined as:

$$\Delta l_i = l_i - l_0 - a_1(p_i - \min(p_1, p_2, p_3)) - a_0, \tag{30}$$

$$p_i = \frac{\Delta l_i k_i}{A_{eff}}, \tag{31}$$

Here, coefficients a_0 and a_1 of the function $f(p_i')$ are determined through simulation. To solve Eqn. 30, the lowest pressure value among the three bellows must be found. I determine this value $\min(p_1, p_2, p_3)$ from the result of Eqn. 26. Based on the length of the initial active region l_0 , a positive air pressure is applied when the calculated l_i is larger than l_0 , and vice versa, and a negative pressure is applied. For the positive pressure case, the minimum pressure is applied to the shortest bellow l_i, and a negative pressure is applied vice versa. With

a positive pressure, the smallest pressure is applied to the shortest bellow l_i , and with a negative pressure case, the smallest absolute pressure is applied to the bellow with the longest l_i . For the bellow with the lowest pressure, Eqn. 30 becomes:

$$\Delta l_i = l_i - l_0 - a_0. \tag{32}$$

Therefore, Eqn. 31 is solved to determine the lowest pressure, and this value is used to calculate pressures of the other bellows.

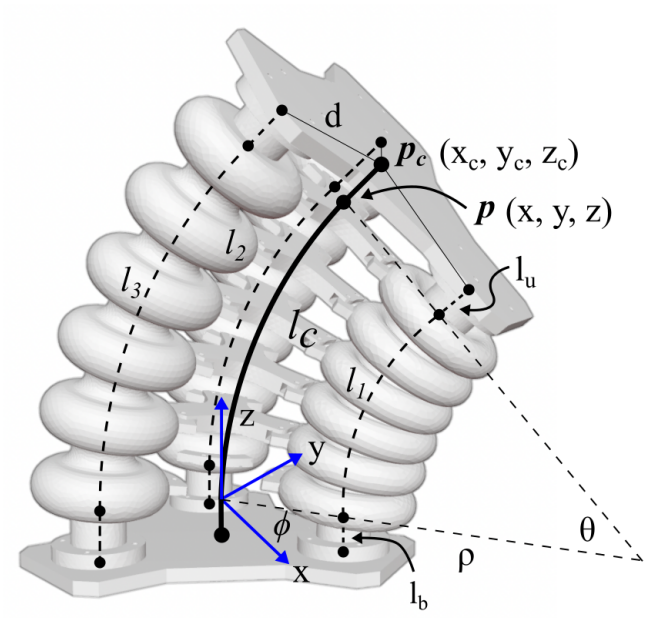

Fig. 4. 7. Constant curvature model. When the bellows are given with different pressures, the manipulator module bends and forms a constant curvature. The top center point p_c of the manipulator module is determined through the deformed length of each bellow.

4.5 Simulation

Finite element analysis (FEA) is conducted using COMSOL Multiphysics® (COMSOL) to find the structural stiffness of the manipulator module and the pressure response to various input pressures. The Neohookian model, suitable for small strain simulation [137] is used to analyze the behavior of soft bodies. The simulation parameter is determined from the stress-stretch curve obtained from a uniaxial tensile test (Fig. 3. 15-(a) and 3. 15-(b)).

4.5.1 Linear translation

I first provide the pressure of the same magnitude and direction to the three bellows and simulated the response of linear translation. I also simulate the response by external compression and tensile forces to mimic the effects of the connected manipulator modules or applied loads. Fig. 4. 8-(a) shows the simulation conditions. The left image shows deformation with an internal pressure, and the right image shows with an external force. Fig. 4. 8-(b) and 4. 8-(c) show the simulation results, depicting the response to the internal pressure, and the response to the external force, respectively. In both cases, the response is smaller in the positive deformation range, and the response pattern changes based on a specific threshold in the negative deformation range. Pressure smaller than the threshold shows a linear behavior because the bellow is fully collapsed and behaved like a cylinder. I perform curve fitting based on the results and obtain the

stiffness by differentiating the fitting curves with respect to the displacement (Fig. 4. 8-(d)). The quadratic fit curves of the positive and the negative regions are expressed as:

$$F_p = \begin{cases} 0.0076(\Delta d)^2 + 0.32(\Delta d) & \text{if } \Delta d > 0 \\ 0.0019(\Delta d)^2 + 0.29(\Delta d) & \text{if } \Delta d \leq 0, \end{cases} \tag{33}$$

$$F_f = \begin{cases} 0.012(\Delta d)^2 + 1.12(\Delta d) & \text{if } \Delta d > 0 \\ 0.0056(\Delta d)^2 + 1.11(\Delta d) & \text{if } \Delta d \leq 0, \end{cases} \tag{34}$$

where F_p is the force due to the internal pressure simulation, F_f is the external force, and Δd is the deformed length. According to the stiffness result, the manipulator module is more resistant (i.e., displays greater stiffness) to external force. The R^2 values of all the fitted curves are greater than 0.99.

4.5.2 Bending

I provide a negative pressure to one bellow to simulate the bending response of the manipulator module since the system shows a higher response to the negative pressure than to the positive pressure from the stiffness result.

Since estimation of the bellow length based on Hooke's law is not accurate in the case of bending, the error is adjusted by comparing the simulation result with the prediction by Hooke's law. Fig. 4. 8-(e) shows the difference in arc length between the simulation and the kinematic model without adjustment. Fig. 4. 8-(f) shows the difference in the arc length according to the magnitude of pressure difference. Assuming the difference in arc length would increase as the pressure difference increases, a linear relation is used as an adjustment function

to solve the inverse kinematics and to avoid overfitting. I find a line passing through the maximum value of the difference and zero (Fig. 4. 8-(f)). The model without adjustment represented by the black dashed curve in Fig. 4. 8-(g) shows a larger difference with the simulation results than the adjusted kinematic model. The bending angle response corresponding to the result Fig. 4. 8-(g) can be seen in Fig. 4. 8-(h).

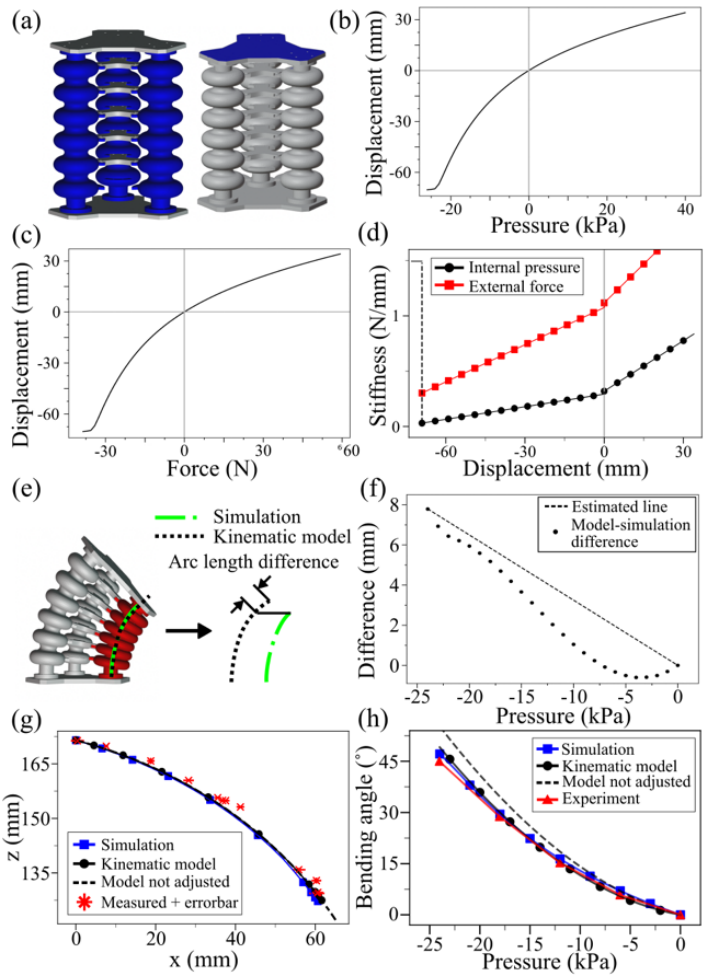

Fig. 4. 8. Simulation conditions and the results. (a) Linear translation: (Left) internally pressurized manipulator, and (Right) externally loaded manipulator on the top. The input stimulus is colored in blue. (b) Internal pressure response. (c) External force response. (d) Stiffness

of the manipulator module. (e) Comparison of the arc lengths between the simulation result and the kinematic model. (f) Arc length difference. (g) Bending simulation result in the task space. (h) Bending angle response.

4.6 Manipulator module localization

I calculate the 3D position of the manipulator module through the forward kinematics calculation based on the onboard pressure sensor readings. However, an error exists between the actual position and the model prediction. Therefore, I use two sensors to localize and control the position of the manipulator module.

4.6.1 String strain sensor-based localization

To estimate the center position of the top, three position vectors of the top plate of the manipulator module are required. Therefore, three string sensors are placed between the bellows. Experiments were first conducted to characterize of the string sensors. The string sensor shows low hysteresis for the displacement up to 100 mm (Fig. 4. 9-(a)). The maximum difference with hysteresis is 18 mV, as shown in the subset of the figure, and the corresponding position difference is 2.6 mm.

The sensor also demonstrates durability and consistent signal readings over 2,000 cycles of 125% strain (Fig. 4. 9-(b) and 4. 9-(c)). The result of quadratic polynomial fitting of the sensor data showed the R^2 value of 0.99. Fig. 4. 9-(d) depicts the initial and fully stretched

(200 mm) lengths of the string sensor.

Different experiments are also conducted to verify the omnidirectionality of the string sensor. An industrial robot arm (UR5e, Universal Robots) is used to stretch the sensor in various directions (Fig. 4. 9-(e)). The sensor is stretched up to 200 mm with the stretching direction varying from -60° to +60° from the vertical, incremented by 30°. The robot's end-effector is driven along the dotted lines from the initial point (i.e., red dot) to the blue target point in each direction for a total length of 200 mm. The sensor responses in all directions are almost identical (Fig. 4. 9-(f)). This contrasts the response of the planar strain sensor, that varies according to the direction of the applied strain.

When assembling the string sensor with the manipulator module, errors may occur due to the different measurement environment. I adjust this using the initialization structure (Fig. 4. 10). I localize the top center point using the measured lengths from the string sensors and the Euler angle measured by the IMU (Fig. 4. 9-(g)). From the string sensors, I obtain the following equations:

$$\left\|\overrightarrow{p_{1,1}p_{2,1}}\right\|^2 = l_{s1}^2, \tag{35}$$

$$\left\|\overrightarrow{p_{1,1}p_{2,1}}\right\|^2 = l_{s1}^2, \tag{36}$$

$$\left\|\overrightarrow{p_{1,1}p_{2,1}}\right\|^2 = l_{s1}^2, \tag{37}$$

I also obtain the following equations from the IMU data and the geometric relationship of the manipulator module:

$$R = R_z(\psi)R_y(\theta)R_x(\phi), \tag{38}$$

$$R \cdot \overrightarrow{O_1p_{1,1}} = [\alpha_1, \beta_1, \gamma_1]^T = \overrightarrow{O_2p_{2,1}}, \tag{39}$$

$$R \cdot \overrightarrow{O_1p_{1,2}} = [\alpha_2, \beta_2, \gamma_2]^T = \overrightarrow{O_2p_{2,2}}, \tag{40}$$

$$R \cdot \overrightarrow{O_1p_{1,3}} = [\alpha_3, \beta_3, \gamma_3]^T = \overrightarrow{O_2p_{2,3}}, \tag{41}$$

where R indicates the rotation matrix along the subscript axis (x, y, and z). Since the position $p_{1,i}$ (i=1, 2, and 3) is initially fixed and the rotation matrix is derived from the IMU data, the product of them is always determined, which is simply expressed as $[\alpha_i, \beta_i, \gamma_i]^T$ (i=1, 2, and 3). Using Eqns. 38-41, Eqns. 35-47 can then be expressed as:

$$\left(x + \alpha_1 - p_{1,1_x}\right)^2 + \left(y + \beta_1 - p_{1,1_y}\right)^2 + \left(z + \gamma_1 - p_{1,1_z}\right)^2 = l_{s1}^2, \quad (42)$$

$$\left(x + \alpha_2 - p_{1,2_x}\right)^2 + \left(y + \beta_2 - p_{1,2_y}\right)^2 + \left(z + \gamma_2 - p_{1,2_z}\right)^2 = l_{s2}^2, \quad (43)$$

$$\left(x + \alpha_3 - p_{1,3_x}\right)^2 + \left(y + \beta_3 - p_{1,3_y}\right)^2 + \left(z + \gamma_3 - p_{1,3_z}\right)^2 = l_{s3}^2, \quad (44)$$

Since these systems of nonlinear equations can only be solved for ideal cases, instead, I find a solution that minimizes the error of the following cost function.

$$f(\vec{x}) = \sum_{i=1}^{3}\left(\left\|\vec{x} + R \cdot \overrightarrow{O_1 p_{1,i}} - \overrightarrow{O_1 p_{1,i}}\right\| - l_{si}\right)^2, \quad (45)$$

where $\vec{x}$ is the position vector of the center of the top. I use a projected gradient descent (PGD) with a backtracking line search algorithm [176] to minimize the cost function, as shown in Algorithm 4. 1.

Algorithm 4. 1 Projected gradient descent with backtracking line search

---

Input: position vector $\vec{x}$, direction α, return β, quadratic cost function f, update termination threshold c_e, step size η, goal position vector $\overrightarrow{x_g}$, projection function P_c

Output: position vector $\vec{x}$

Initialization: $\vec{x} \leftarrow \overrightarrow{x_g}, \eta \leftarrow 1, \alpha \leftarrow 0.5, \beta \leftarrow 0.12$

1: **while** $(f(\vec{x}) > c_e)$ **do**

```
    while (f(x⃗) − αη‖∇f(x⃗)‖² − f(x⃗ − ηf(x⃗)) < 0) do
        η ← β · η
    end while
    x⃗ ← P_c(x⃗ − η · ∇f(x⃗))
    η ← 1
end while
return x⃗
```

Here, I set the termination threshold c_e as 1. The iteration is terminated when the cost function value becomes smaller than c_e. Otherwise, the step size η is iteratively found using the backtracking line search. By multiplying the tangent with direction α, multiplication of the step size η by the return β is repeated until the difference between the $f(\vec{x}) - \alpha \cdot \eta \|\nabla f(\vec{x})\|^2$ and $f(\vec{x} - \eta \cdot \nabla f(\vec{x}))$ turns positive. This approach adaptively adjusts the step size η and updates the cost function at every step. When the computed position exceeds the range of motion of the manipulator module, the result is projected on the boundary. Since the edge device with low computational power is used, this approach helps reducing the number of iterations. The localization result using the string sensor can be seen in Fig. 4. 9-(h). The cost function calculation result with and without applying the PGD can be seen Fig. 4. 11.

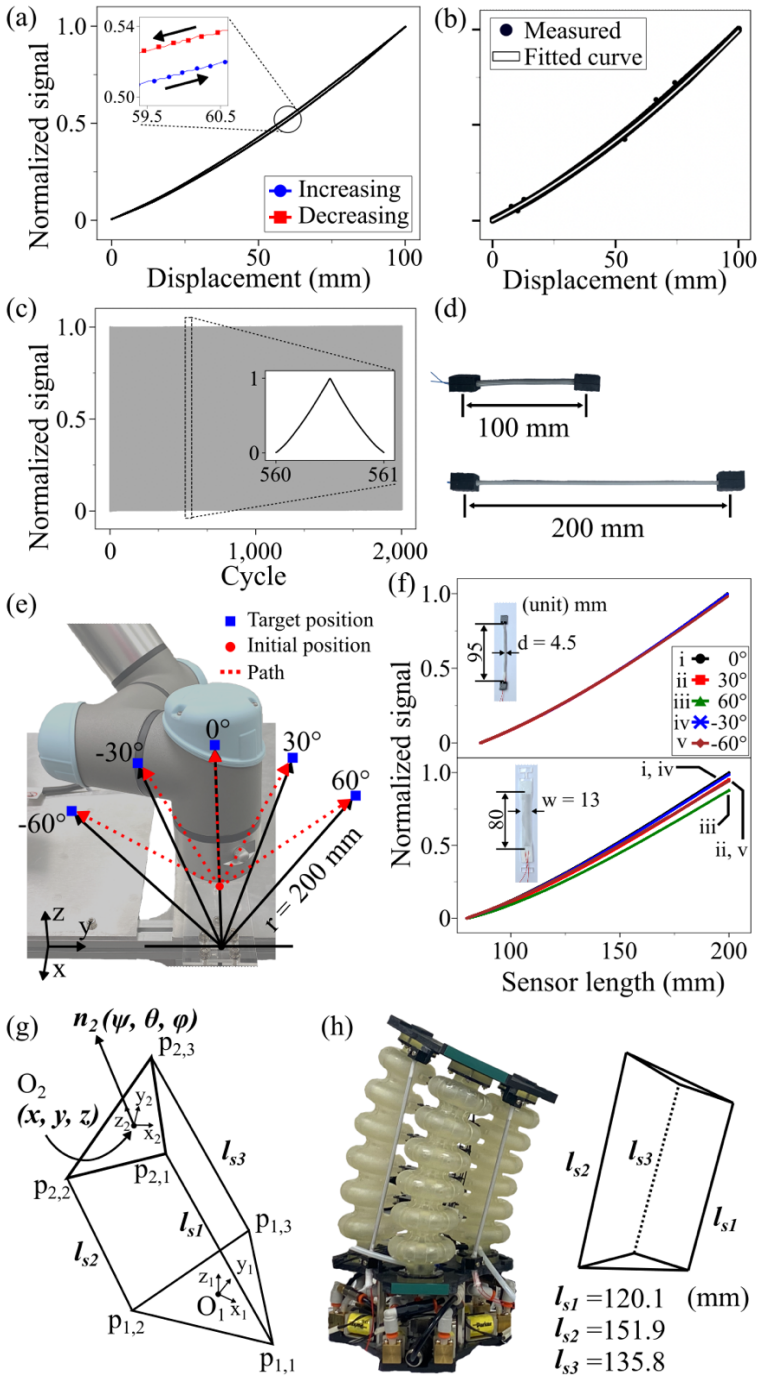

Fig. 4. 9. Experimental result of soft string sensor. (a) Normalized sensor signal during a cycle of stretching and releasing. The blue curve represents extension, and the red curve represents recover. (b) Sensor signal response over 1,000 cycles. The red curve indicates

polynomial fitting. (c) Sensor signal over 2000 cycles. The inset plot is the result of the 280-th cycle. (d) (Top) Initial length of the string sensor and (Bottom) the fully stretched length. (e) The experimental setup for directional response of the string sensor. (f) Signal response to stretching in various directions of the string sensor and a planar sensor. (g) Schematic of manipulator module localization using string sensors. (h) Measurement and localization result.

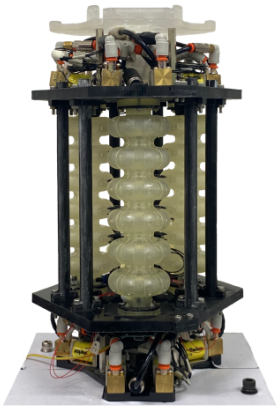

Fig. 4. 10. String sensor initialization structure. Calibration is performed using a tensile tester externally before connecting to the manipulator module. During this process, shifting or changing of readings may occur due to an environment change. The length of each string sensor is initialized after constrained by the initialization structure that limits the body rotation of the upper plate.

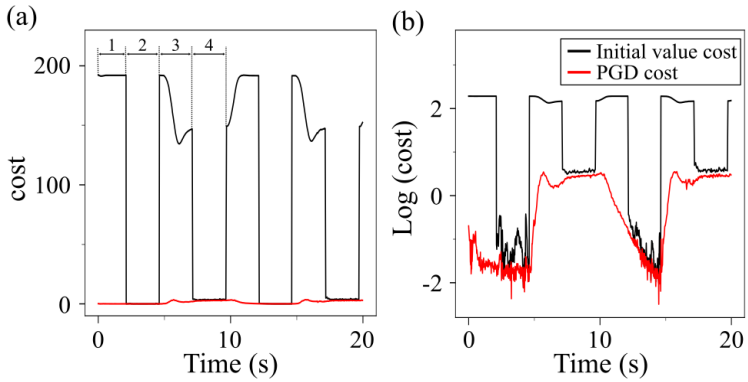

Fig. 4. 11. Cost function calculation result. The manipulator module repeatedly moves between p_1 (0, 0, 162) and p_2 (0, 30, 140). (a) Black curve indicates cost using initial guess and red curve indicates result of applying projected gradient descent method. Interval 1 is a transition period from p_1 to p_2, and the optimization is performed with an initial guess through the constant curvature model. Intervals 2 and 4, the goal positions p_2 and p_1 are used as initial guesses for optimization. Interval 3 is the opposite of the interval 1. (b) Log scale cost function calculation result. When the cost value is 180, the length error per string sensor is $\sqrt{60} = 7.8$ mm. Through PGD, the cost value is reduced to a maximum of 4 or less, and the calculated error is less than 1.2 mm.

4.6.2 Vision-based localization

In addition to the string sensors, the manipulator module is localized externally with a depth camera (RealSense L515, Intel®). Colored landmarks are attached to the top and the bottom plates, and the length of each bellow is calculated using the measured depth information and a transformation matrix. While the color detection mechanism is relatively simple, similar color objects or noises also affect the performance of the depth camera. To solve this issue, the

surrounding must be cleared generally, which poses more constraints to the operating environment. Instead, I utilize a one-stage object detection model named YOLOv5 [89] (Fig. 4. 12-(a)) to find a region of interest which contains the manipulator module in the image. Train images are obtained from various distances from the manipulator module with different orientations (Fig. 4. 12-(b)). The captured images are rotated 90°, 180°, and 270° through image processing to diversify the dataset. The YOLOv5 model can achieve 60 frames per second on a 720×480 image and 30 frames per second on a 1280×720 image with a graphics processing unit (Geforce 1060, NVIDIA), which allows sufficiently fast processing for close-to-real-time control. Fig. 4. 12-(c) compares the performance of the depth camera with and without object detection: the color detection (left) experiences difficulty in locating the manipulator module due to various objects in the surrounding with similar colors, while object detection (right) performs accurate location of the manipulator module despite these noises. In addition, even if a gripper is mounted at the end of the manipulator (Fig. 4. 13-(a) and 4.13-(b)).

With the depth information obtained from the depth camera and the trained model, the top center point of the manipulator module can be calculated using vectors determined by the IMU and other design parameters. The depth camera provides two position vectors ${}^{C}\overrightarrow{O_C LM_1}$ and ${}^{C}\overrightarrow{O_C LM_2}$, which connect the landmarks LM_1 and LM_2 on the manipulator module from the origin of the camera frame $\{C\}$ (Fig. 4. 12-(d)). Also, I define the position vectors from the center points of the top and the bottom to each bellow as ${}^{1}\overrightarrow{O_1 A_1}$, ${}^{1}\overrightarrow{O_1 B_1}$, ${}^{1}\overrightarrow{O_1 C_1}$, and ${}^{1}\overrightarrow{O_1 LM_1}$ which connect the points A_1, B_1, C_1, and LM_1 with the origin of local frame $\{1\}$ and ${}^{2}\overrightarrow{O_2 A_2}$, ${}^{2}\overrightarrow{O_2 B_2}$, ${}^{2}\overrightarrow{O_2 C_2}$, and ${}^{2}\overrightarrow{O_2 LM_2}$ which connect the points A_2, B_2, C_2, and LM_2 with the origin of the local

frame {2}. Then the vectors ${}^{C}\overrightarrow{O_C LM_1}$ and ${}^{C}\overrightarrow{O_C LM_2}$ can be described with respect to local frame {1} as:

$$ {}^{1}\overrightarrow{O_C LM_1} = {}^{1}_{C}R \cdot {}^{C}\overrightarrow{O_C LM_1}, \tag{46} $$

$$ {}^{1}\overrightarrow{O_C LM_2} = {}^{1}_{C}R \cdot {}^{C}\overrightarrow{O_C LM_2}, \tag{47} $$

where ${}^{1}_{C}R$ is the rotation matrix that transforms the local frame {1} into the camera frame $\{C\}$. This matrix is obtained from the initial setup. From Eqns. 46, 47, ${}^{1}\overrightarrow{O_C O_1}$ and ${}^{1}\overrightarrow{O_C O_2}$ are obtained as:

$$ {}^{1}\overrightarrow{O_C O_1} = {}^{1}_{C}R \cdot {}^{C}\overrightarrow{O_C P_1} - {}^{1}\overrightarrow{O_1 LM_1}, \tag{48} $$

$$ {}^{1}\overrightarrow{O_C O_2} = {}^{1}\overrightarrow{O_1 LM_2} - {}^{1}_{2}R \cdot {}^{2}\overrightarrow{O_2 LM_2}, \tag{49} $$

where ${}^{1}_{2}R$ is the rotation matrix that transforms the local frame {1} into {2}. This matrix is derived from the roll, pitch, and yaw angles measured by the IMU. Finally, the following vectors are obtained ${}^{1}\overrightarrow{O_1 O_2}$, ${}^{1}\overrightarrow{O_1 A_2}$, ${}^{1}\overrightarrow{O_1 B_2}$, and ${}^{1}\overrightarrow{O_1 C_2}$ and expressed as:

$$ {}^{1}\overrightarrow{O_1 O_2} = {}^{1}\overrightarrow{O_C O_2} - {}^{1}\overrightarrow{O_C O_1}, \tag{50} $$

$$ {}^{1}\overrightarrow{O_1 A_2} = {}^{1}\overrightarrow{O_1 O_2} - {}^{1}_{2}R \cdot {}^{2}\overrightarrow{O_2 A_2}, \tag{51} $$

$$ {}^{1}\overrightarrow{O_1 B_2} = {}^{1}\overrightarrow{O_1 O_2} - {}^{1}_{2}R \cdot {}^{2}\overrightarrow{O_2 B_2}, \tag{52} $$

$$ {}^{1}\overrightarrow{O_1 C_2} = {}^{1}\overrightarrow{O_1 O_2} - {}^{1}_{2}R \cdot {}^{2}\overrightarrow{O_2 C_2}, \tag{53} $$

The lengths between the centers of each bellow l'_1, l'_2, and l'_3 are expressed using the Eqns. 51-53 as:

$$ l'_1 = \left\| {}^{1}\overrightarrow{O_1 A_2} - {}^{1}\overrightarrow{O_1 A_1} \right\|, \tag{54} $$

$$ l'_2 = \left\| {}^{1}\overrightarrow{O_1 B_2} - {}^{1}\overrightarrow{O_1 B_1} \right\|, \tag{55} $$

$$ l'_3 = \left\| {}^{1}\overrightarrow{O_1 C_2} - {}^{1}\overrightarrow{O_1 C_1} \right\|. \tag{56} $$

Estimation of each lengths using Eqns. 54-56 can be seen in Fig. 4.12-(e).

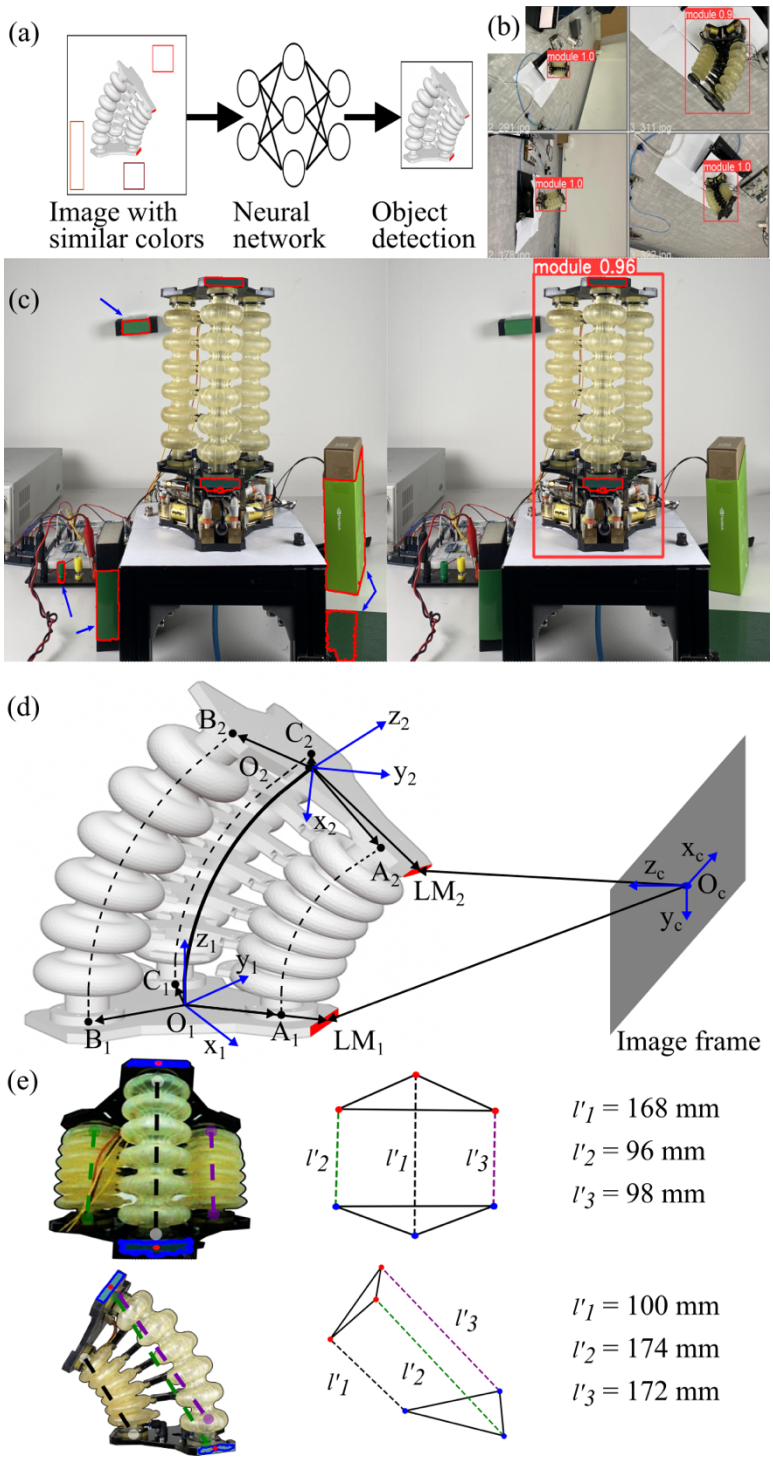

Fig. 4. 12. Vision-based object detection and central point localization of the top of the manipulator module. (a) Schematic of object detection using deep learning (YOLOv5). (b) Example of training data obtained

from various rotation angles and distances. (c) Result of object detection: (Left) Color detection result without object detection. Arrows indicate non-target objects. (Right) Color detection result with object detection. (d) Local frame and position vector schematic of the camera and the manipulator module for expressing the center position. (e) Experimental results: (Left) marker detection result located on the manipulator module base using deep learning. (Right) Simplified manipulator module and lengths of each bellows.

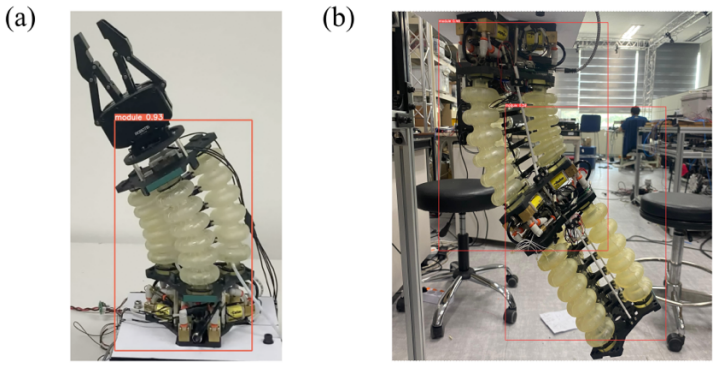

Fig. 4. 13. Object detection result with different configuration. (a) Photo of the manipulator module is bent to the left with the gripper mounted. (b) Manipulator module detection result in real environment.

4.7 Experiment

4.7.1 Pressure response

An experiment was conducted to verify the workspace and repeatability of the manipulator module. First, we measured the bending response to different input pressures for each bellow actuator

(Fig. 4. 14-(a) and 4. 14-(b)). The maximum bending angle of 70.4° is achieved with an input pressure of −40 kPa at P_1 and +30 kPa at P_2. The bending angle can be further increased by increasing the positive pressure, but I limit the maximum pressure to +30 kPa for safety (Position 1). When only the positive pressure of P_2 is removed while maintaining the negative pressure at P_1, the bending angle is decreased to 49.2° (Position 2). The dash-dotted line shows the bending responses when only the negative pressure is applied. Fig. 4. 14-(c) shows the maximum and the minimum lengths achieved by expansion and contraction, respectively. The manipulator module reaches 102 mm for contraction and to 204 mm for expansion when the input pressures of −40 kPa and +50 kPa, respectively, are applied to the three actuators. However, as mentioned previously, I limit the maximum input pressure to +30 kPa for safety, with the corresponding length of 198 mm.

The manipulator module is also tested under repeated actuations and length changes (Fig. 4. 14-(d)). All three bellows are loaded and unloaded with an input pressure of −40 kPa pressure. The minimum and the maximum lengths of the manipulator module are consistent over more than 5,000 cycles. The inset in Fig. 4. 14-(d) shows the length changes during one cycle.

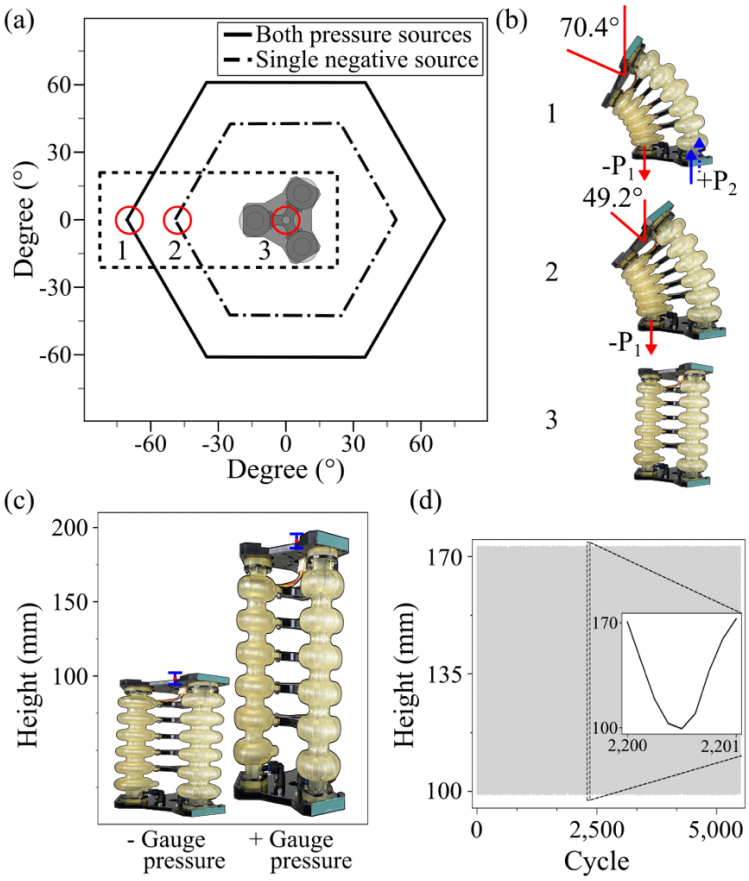

Fig. 4. 14. Pressure responses of the manipulator module. (a) Range of bending angles with different input pressures. The solid line represents the maximum angles achieved using both negative and positive pressure, and the dash-dotted line represents the angles achieved using negative pressures only. (b) Measured bending angles at Positions 1, 2, and 3 when P_1 and P_2 were −40 kPa and P_2, respectively. (c) Linear translation: (Left) Negative pressure response and (Right) Positive pressure response. (d) Repeatability test result. Inset plot shows the 2,200-th cycle.

Next, the manipulator module is controlled by a proportional-derivative (PD) controller, with P and D gains K_P and K_D of 0.013 and 0.5, respectively. I first experiment of step input responses (Fig. 4.

15-(a)). The pressure is increased with an increment of 10 kPa in the range −40 kPa to + 20 kPa, which is selected to prevent any damages to the bellows. As a result, when the difference between the input and the initial value increase, so do the settling time.

I also experiment the effect of the control limit (Fig. 4. 15-(b)). The flow rate of the solenoid valve is controlled by the input voltage, and I limit the change of the input voltage to 10 mV, which is determined empirically; Voltage changes smaller than 10 mV requires too long settling times for effective control of the manipulator module compared to the voltage change larger than 10 mV (Fig. 4. 15-(b)). However, the change in voltage is larger than 10 mV results in an overshoot with positive pressure inputs. As a result, I select a control limit of 10 mV.

Both the negative and positive pressure sources are connected to the bellow, allowing for both contraction and expansion. Since the flow rate of the vacuum input generated by the ejector is smaller than that of the compressed air, it is not necessary to change the control mode between the positive and the negative pressures (Fig. 4. 15-(c)). I apply a + 25 kPa to one bellow, and one case used both pressure sources and the other case, used compressed air only. In both cases, the target pressure is achieved, demonstrating control of the manipulator module is possible without changing the control mode. However, when both the positive and the negative pressure sources are used, the overshoot is larger, and the settling time is longer than those of a single source.

In addition, I conduct an experiment to determine the resolution of the manipulator module. The response is recorded while the input pressure is changed by 0.1 kPa or 0.05 kPa. By controlling each solenoid valve, the desired pressure is achieved (Fig. 4. 15-(d)-left).

However, the bending angle was unable to resolve 0.05 kPa changes (Fig. 4. 15-(d)-right). Finally, the pressure response is tested with sinusoidal inputs with various periods ranging from 3.96 sec. to 1.98 sec. (Fig. 4. 15-(e)). The shortest period the manipulator module is able to follow is 2.64 sec., as it can be observed that the pressure failed to follow the input with a period of 1.98 sec. Fig. 4. 15-(f) shows the pressure response and the corresponding response of the bending angle with a sinusoidal input wave with a period of 3.96 sec. The manipulator module responds to even small fluctuations in pressure, with a delay of approximately 130 msec. after the minimum or the maximum pressure is measured.

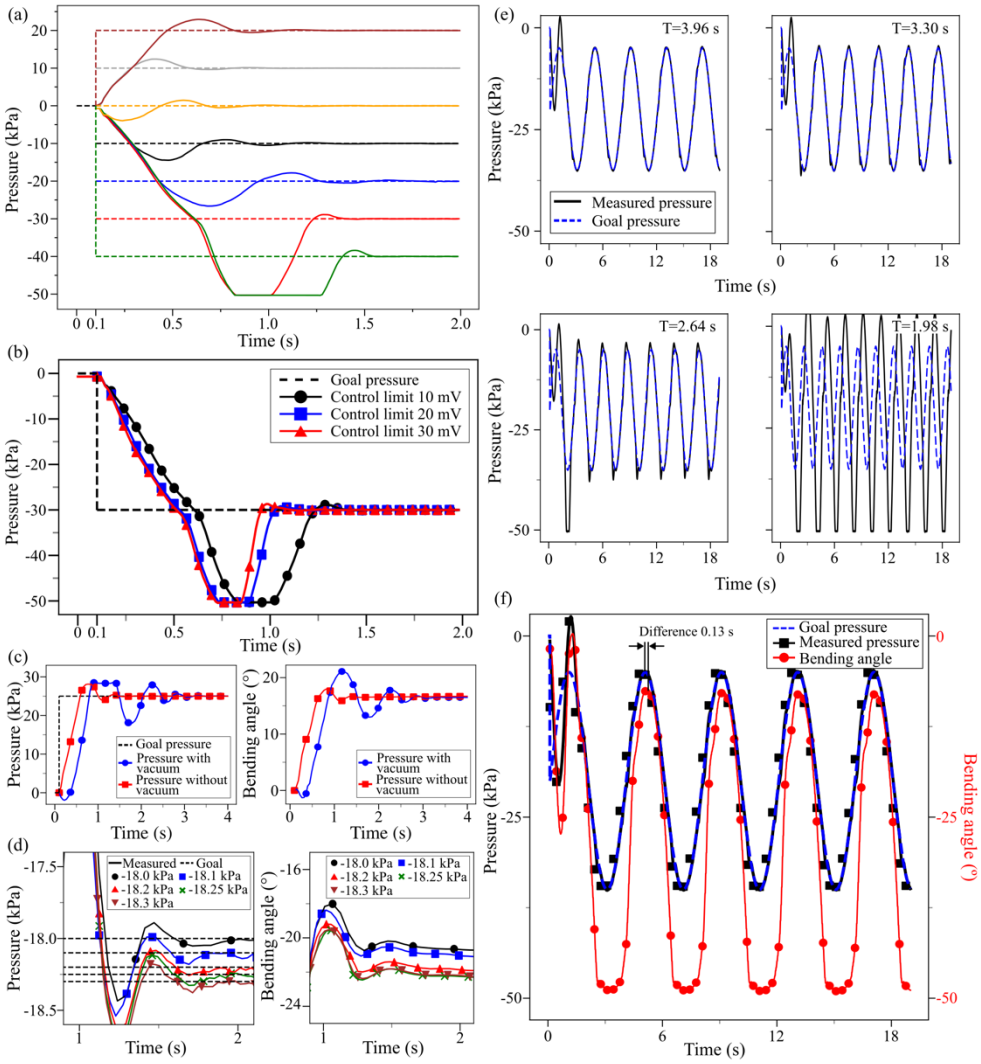

Fig. 4. 15. Experimental result with various pressure inputs. (a) Step responses of the module. (b) Pressure response with different control limits. (c) Response to positive target pressure according to operation of the ejector: (Left) pressure response and (Right) bending angle. (d) Pressure resolution test result: (Left) pressure response and (Right) the corresponding bending angle. (e) Pressure response to sinusoidal input waves with periods (T) of 3.96, 3.3, 2.64, and 1.98 sec., respectively. (f) Bending for a sinusoidal pressure input (T = 3.96 sec.).

4.7.2 Contact recognition

I implement contact detection using embedded sensors to ensure safe interaction with the surrounding environment. The manipulator module detects contact through air pressure sensors, which respond to changes in internal pressure when the internal volume of the bellows changes by contact. I employ the density-based local outlier factor (LOF) algorithm for contact recognition, as described by [177], [178]. The main concept of this algorithm is that a point with a lower local density is more likely to be an outlier of the cluster. For example, when weak contact induces a pressure change of 0.1 kPa, the LOF value is -3.02, which is clearly different from the average of the cluster. To quantify the LOF, the following are defined $k-\mathrm{dist}(p)$ is the k-th smallest distance from the given point p. The k-nearest neighbor set of data points whose distance from the point p is less than $k-\mathrm{dist}(p)$ is denoted as $N_k(P)$. The reachability distance $r-\mathrm{dist}_k(p,q)$ is defined as:

$$r-\mathrm{dist}_k(p,q) = \max\{\mathrm{dist}(p,q), k-\mathrm{dist}(q)\}, \tag{57}$$

where q is another data point the k-nearest neighbors $N_k(p)$. The local reachability density $\mathrm{lrd}(p)$ is the reciprocal of the average reachability density of given point p and its k-nearest neighbors. i.e.,

$$\mathrm{lrd}(p) = 1/\frac{\sum_{q\in N_k(p)} \mathrm{r-dist_k}(p,q)}{|N_k(p)|}, \tag{58}$$

where $|N_k(p)|$ is the number of elements in the set. Finally, the local outlier factor $\mathrm{lof}(p)$ is defined as:

$$\mathrm{lof}(p) = \frac{\sum_{q\in N_k(p)} \mathrm{lrd}(q)}{|N_k(p)|}/\mathrm{lrd}(p), \tag{59}$$

which is the ratio of $\mathrm{lrd}(p)$ to the average of $\mathrm{lrd}(q)$ at point q

belonging to the k-nearest neighbors of point p.

I apply the LOF to pressure measurements for contact detection. During a state without contact, I gather 40 data points for each sensor and used them as a dataset for calculating the LOF of the cluster. Since the pressure has continuous values, it is impossible to calculate the LOF for all pressure levels. So, I collect pressure measurements for a specific pressure p_0 from the pressure sensor. For the target pressure p_g, the difference $p_g - p_0$ is added to all pressures in the original dataset. Shifting the pressures in the original dataset is valid because the measured pressure values are bounded after the settling time, regardless of the input pressure (Fig. 4. 15-(a)).

The manipulator module's contact detection capability is tested using data collected for -10 kPa. Corresponding the LOF calculation of the dataset can be seen in Table 4. 1. The pressure of all bellows is set to -10 kPa, and I alternately touch each bellow and measured its pressure. The pressure response and touch detection results are shown in Fig. 4. 16-(a). Five pressure level spikes are detected (Fig. 4. 16-(a)-left), corresponding to five intervals (Fig. 4. 16-(a)-right). I then apply different negative gauge pressures to each bellow to produce bending and repeat the experiment. Detection is possible even in bending states by calculating the LOF using pressure measurements (Fig. 4. 16-(b)). Finally, I conduct an experiment to detect contact with the positive gauge pressure applied. Contact is detected even if different pressures are applied to the bellows (Fig. 4. 16-(c)).

Since all bellows are mechanically connected, contact in one bellow affects the other bellows as well. A triboelectric touch sensing mechanism can be used to enable decoupling of sensing signals from each bellow. The simple structure and working mechanism of triboelectric touch sensing allow each bellow to have independent

sensing capability without significant structural modifications. To quantitatively investigate the triboelectric sensing capability, I conduct an experiment using a film-type sample. Fig. 4. 16-(d) and 4. 16-(e) show voltage generation when the sample is touched by copper and a finger under a contact frequency of 5 Hz, and voltages of over 10 V are generated. Based on these results, I embed organogel into the bellow and measure the voltage generation due to various external contacts (Fig. 4. 16-(h)). The test is conducted with and without actuation. The measured intensity is decoupled, and touch is independently identified on each bellow even in the case of multi-touch (Fig. 4. 16-(f)). In addition, detect is possible when the manipulator module is actuated (Fig. 4. 16-(g)). Actual touching of the bellows can be seen in Fig. 4. 16-(h).

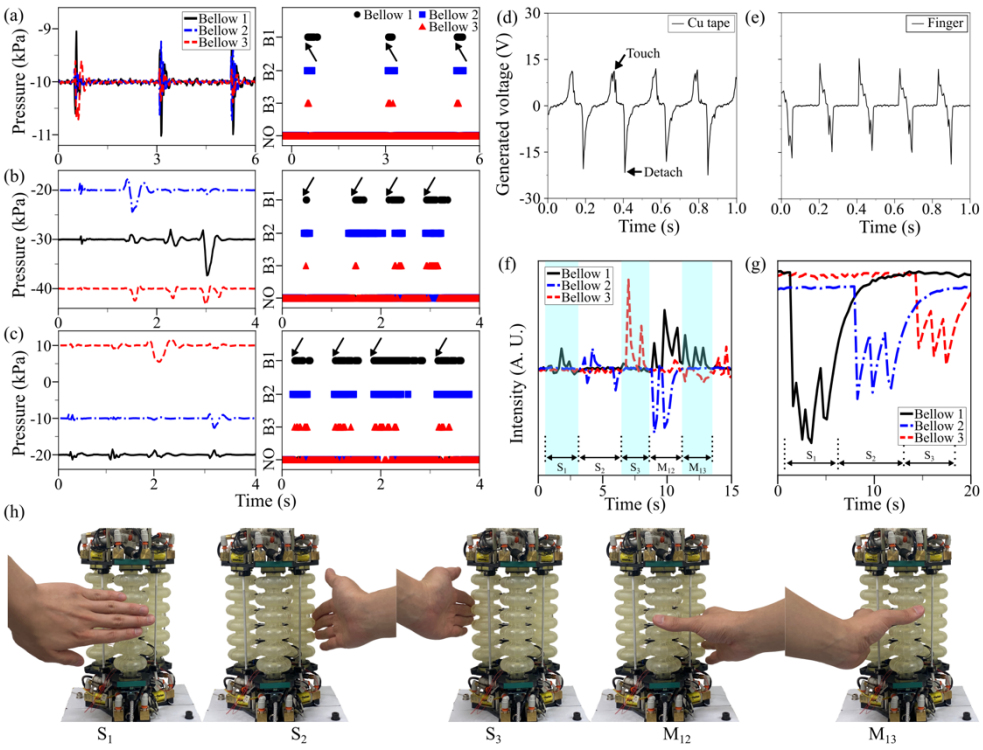

Fig. 4. 16. Pressure and touch sensing results when (a) p_1, p_2, and $p_3 = -10$ kPa. (b) $p_1 = -30$ kPa, $p_2 = -20$ kPa, and $p_3 = -40$ kPa. (c)

$p_1 = -20$ kPa, $p_2 = -10$ kPa, and $p_3 = 10$ kPa. For all touch recognition results, the dataset was sampled at -10 kPa. Arrows indicate the start of touch. Voltage generation when touched with (d) copper tape and (e) finger. Intensity changes due to touching of bellow with embedded gel (f) without actuation, and (g) with actuation. Subscripts S and M indicate single touch and multi-touch. (h) Images of various touch modes.

Table 4. 1. Calculation of LOF means and standard deviations according to the pressure and the number of samples

Pressure [kpa] (# data)	-10 (40)	-10 (20)	-20 (40)	-30 (40)	-40 (40)	10 (40)
Mean	-1.00	-1.00	-1.00	-1.00	-1.00	-1.00
Std-dev	0.005	0.01	0.006	0.006	0.005	0.005

4.7.3 Control of manipulator module

I control the manipulator module based on forward and inverse kinematics, using measurements from the string sensors, the IMU, and the depth measurement camera. I set goal positions in a 3D space and calculate the target length of each bellow based on inverse kinematics. I then implement feedback control without calculating the input pressures corresponding to the target lengths of the actuators to reduce the computational load on the processor. Here, a controller with P and D gains of 0.010 and 0.5, respectively, is used to control the lengths of the bellows.

First, the accuracy of the depth camera is tested, as shown in Fig. 4. 17. Then I control the manipulator module using only the vision data. The three bellows of the manipulator module are controlled and follow the target lengths in the actuator space (Fig. 4. 18-(a)). The corresponding results in the task space show that the manipulator module is controlled and follows the target position (Fig. 4. 18-(b)). Fig. 4. 18-(c) shows the tracking results projected on $x-y$ plane of the top center point of the manipulator module. These results validate the constant curvature model for the manipulator.

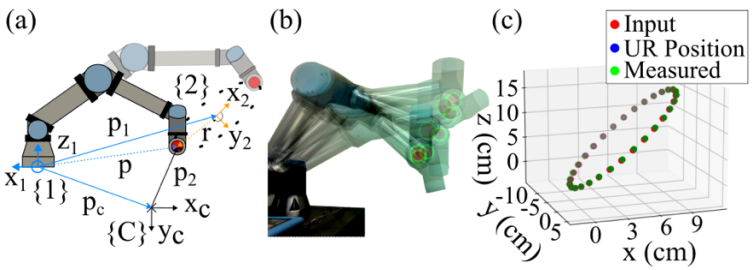

Fig. 4. 17. Depth camera measurement accuracy test setup and result. (a) Schematic of local frames and position vectors for the depth camera, UR base, and the center of the 3D circular orbit. (b) Nested real UR robot trajectory of the end-effector. (c) Result of the input position, the position calculated by the UR controller and the position estimated by the camera measurement. The error between the goal position and the measured by the depth camera is 1.57 mm, and the standard deviation is 0.75 mm.

The manipulator can also be controlled using the string sensors and the IMU. The manipulator is programmed to repeatedly move between the points $(0, 0, 162)$ and $(0, 30, 140)$, using feedback control

based on the measurements from the string sensor and IMU. The bellows follow the target lengths in the actuator space (Fig. 4. 18-(d)). I conduct an experiment with the tracking the movement of the manipulator module in the task space with vision while controlling it with string sensors (Fig. 4. 18-(e)).

As is done for the vision-based control, control with the string sensors is tested for various goal positions. Two experiments are conducted with different time intervals (5 sec. and 0.05 sec.) between the goal positions. The longer interval time allows the manipulator to reach the target positions with the higher accuracy (Fig. 4. 18-(f) and 4. 18-(g)). Experiments are conducted that the manipulator is controlled to repeatedly move to the target positions of $(0, 0, 162)$ and $(0, 30, 140)$ using the camera and string sensors, respectively. After three seconds, the current position of the manipulator is measured and calculated the standard deviation of 1.16 mm and 0.02 mm for the camera and the string strain sensor, respectively.

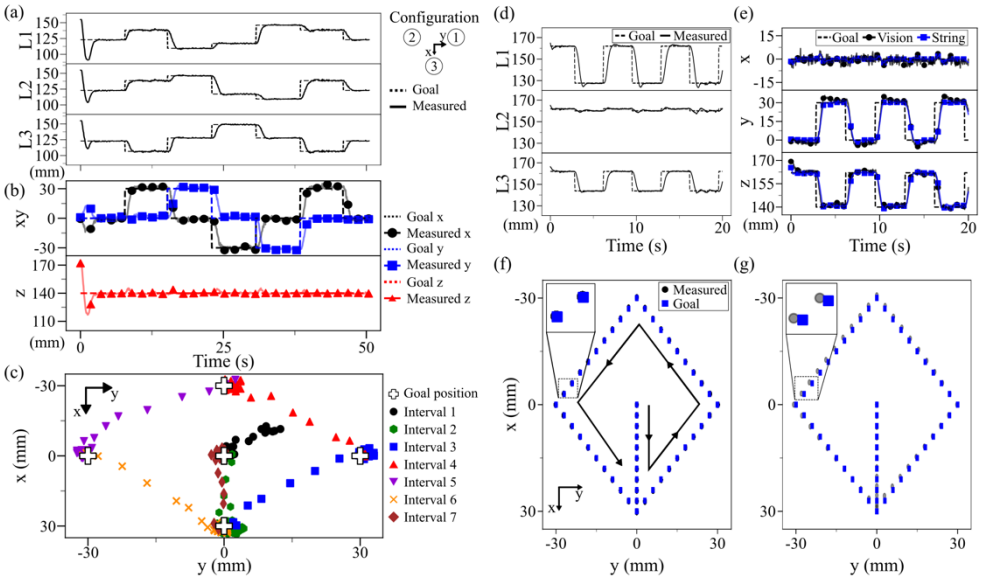

Fig 4. 18. Manipulator module control results. (a) Results of bellow

length feedback control using only vision. (b) The corresponding results in task space. (c) Positions of the manipulator module and goal in $x-y$ plane. (d) Results of string sensor-based feedback control of the bellows. (e) The corresponding results in task space. Time interval of between each goal is 5 sec. (f) and 0.05 sec. (g). The arrows in (f), indicate the direction of the movements.

While the experiment discussed above only concerned a single manipulator module alone, additional loads or manipulator modules can be applied or connected. First, a robotic gripper (RH-P12-RN; ROBOTIS) with a mass of 600 g, is mounted on top of the manipulator module (Fig. 4. 19-(a)-left). The same target points are given, and the manipulator position is tracked (Fig. 4. 19-(a)-right). Next, I mount another manipulator module (Fig. 4. 19-(b)-left), weighing about 500 g, and tracked the motion of the entire arm. Compared to 4. 18-(c), the error between the target and the measured positions increases when the load or another manipulator module is mounted or connected. This is because the constant curvature model does not consider the change in the kinetics due to the external load.

Therefore, an algorithm correcting the position error is applied to compensate the inaccuracy of the constant curvature model in the presence of an external load. The error $\vec{e}$ between the measured current position $\vec{p}$ and the target position $\overrightarrow{g_p}$ is calculated, and it is determined whether the distance $\|\vec{e}\|$ exceeded the threshold k when $t_e > t_s$ (where t_e is elapsed time and t_s is settling time). Within the threshold, the current state of the module is maintained. Otherwise, the target position is adjusted to $\overrightarrow{g_p}'$ by subtracting the product of the

error $\vec{e}$ and the decay rate γ from the former target position $\overrightarrow{g_p}$. The decay rate γ is set as $0 < \gamma < 1$ to prevent oscillation. The whole process is provided in Algorithm 4. 2. Fig. 4. 19-(b)-right shows the motion of the module when this algorithm is applied. The manipulator module is given with seven goal positions, and the measurements are recorded with both the depth camera and the string strain sensors. Compared to the results in Fig. 4. 19-(a), I observe clear reduction in error when the adjustment algorithm is applied. The coordinates in the time domain are shown in Fig. 4. 19-(c), and I confirm that the manipulator successfully reaches the goal positions through continuous adjustments.

Algorithm 4. 2 Goal position adjustment

Input: decay rate γ, goal position $\overrightarrow{g_p}$, adjusted goal position $\overrightarrow{g_p'}$, error $\vec{e}$, current position $\vec{p}$, settling time t_s, elapsed time t_e, threshold k

Output: None

Initialization: $k \leftarrow 1$

```
while (k < ||e||) do
    if (t_s < t_e) then
        e = p − g_p
        if (||e|| < k) then
            Maintain current goal position
        else
            g_p' = g_p − γ · e
            PD control based on g_p'
        end if
```

```
    end if
end while
```

I also test translation of the manipulator from $(0, 0, 162)$ to $(30, 0, 140)$, with and without the adjustment algorithm (Fig. 4. 19-(d)). Similarly, the final positions of the manipulator are closer to the goal positions with the adjustment algorithm, reaches within one or two adjustments. The insets show the maximum error of 10 mm in the x-position and 4 mm in the z-position.

Arbitrary points in a 3D space were given to the manipulator, and the trajectory is tracked using a motion capture system (OptiTrack) and the string sensors in $x - y$ plane (Fig. 4. 19-(e)). The corresponding measurements in a 3D space are shown in Fig. 4. 19-(f). The assembled soft robotic arm is shown in Fig. 4. 19-(g)-i through 4. 19-(g)-vi. The mean position error of 14 randomly chosen goal positions calculated from the sensors is 0.78 mm, and the standard deviation is 0.31 mm. The maximum position error is 0.98 mm, which is smaller than the termination condition $k = 1$, confirming that the algorithm works on the manipulator's own coordinate system. From the measurements of the motion capture system, the mean position error is 1.94 mm, the standard deviation is 0.96 mm, and the maximum error is 3.70 mm. The proposed algorithm works in presence of touch while actuation (Fig. 4. 20).

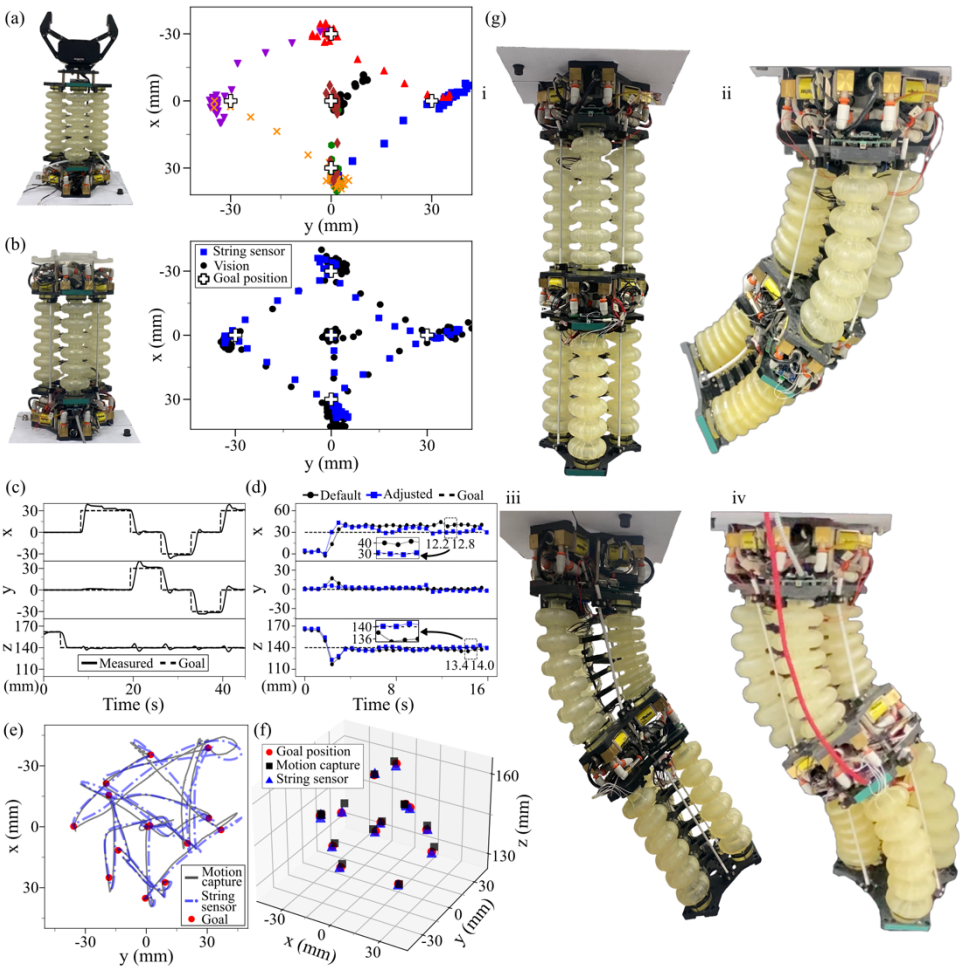

Fig. 4. 19. Load mounted manipulator module control experiment results. (a) Image of gripper mounted manipulator module (left) and vision-based manipulator module control results without adjustment algorithm (right). (b) Pneumatic components mounted manipulator module image (left) and string sensor-based manipulator module control results with the adjustment algorithm (right). (c) Manipulator module coordinates in time domain. (d) Comparison of the two control methods. Experimental results of reaching random goal points tacked with motion capture system and string sensors (e) and corresponding results in 3D space (f). (g) Images of various actuation of the soft robotic arm. i. Default state. ii. Bending both manipulator modules to form the same curvature. iii. Bending upper manipulator module only.

vi. Opposite bending of the manipulator modules.

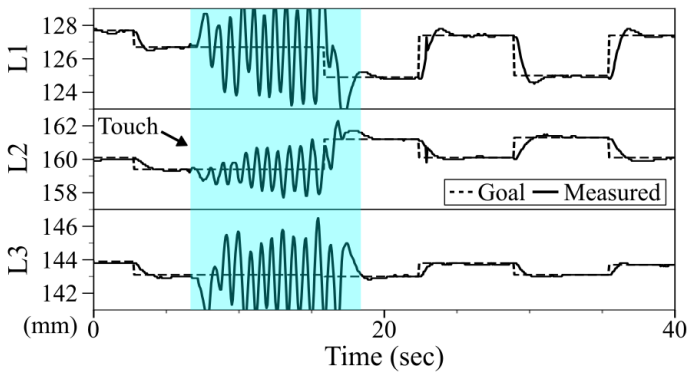

Fig. 4. 20. Goal position adjustments in the presence of touch while controlling the load-mounted manipulator module. Even if a touch occurs and makes position change of the manipulator module, the position is controlled by changing the target length of the bellows to reach the goal position.

4.8 Demonstration

4.8.1 Interaction based task performs

I test the proposed manipulator for safe human interactions (Fig. 4. 21-(a) and 4. 21-(b)). The robotic arm is composed of two manipulator modules and a gripper. I set the human touch signals as triggers to perform three actions: one for closing and opening of the gripper, another for contraction of the upper manipulator module, and other for bending of the entire arm. For the bellows numbered 1, 2, and 3 on the upper module (Fig. 4. 21-(a)), the touch sequence 3-2-1-3 (i.e., gripping an object, contracting the upper manipulator module, bending forward both modules in the forward direction, and releasing

the object) is performed (Fig. 4. 21-(b)). In the intensity plots, the threshold level is different for each bellow since the baseline intensity changes according to the operation state of the manipulator module, and so the threshold level for each actuator is automatically adjusted after each touch.

By customizing the end-effector and mapping the specific tasks, this application can be further extended for multi-touch or continuous-touch sequence with specific intervals, which will allow the soft robotic arm to perform more complex tasks.

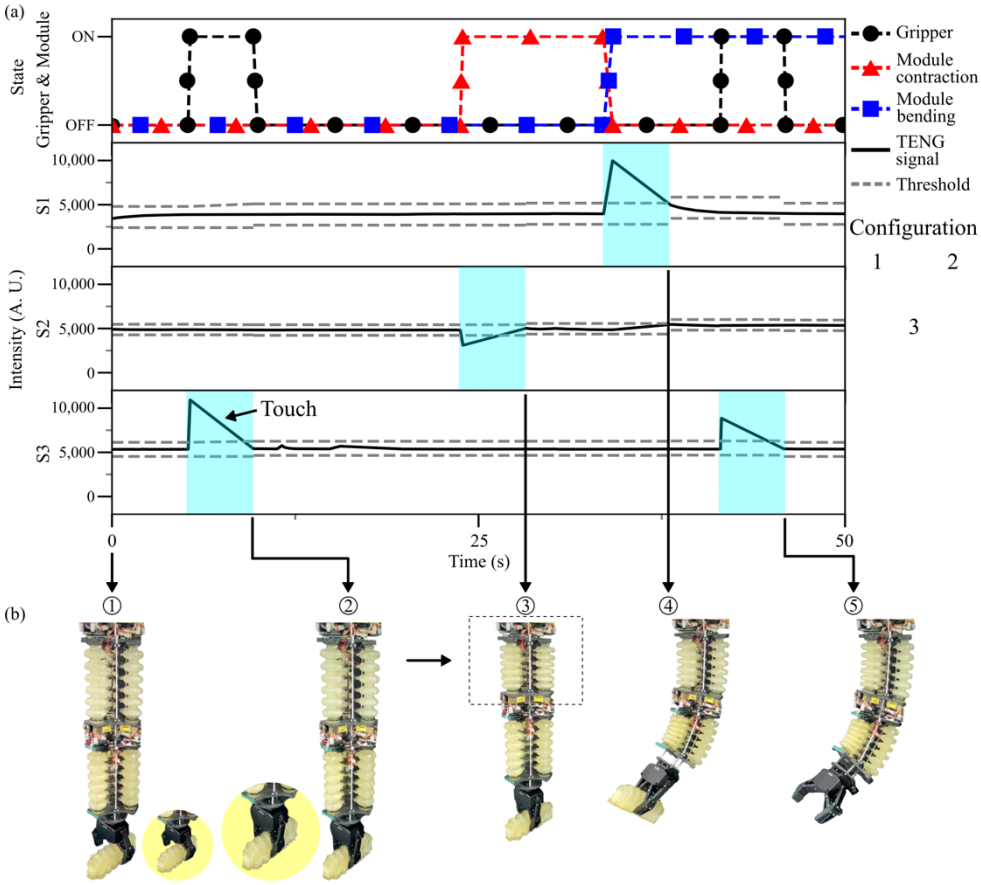

Fig. 4. 21. Application using the assembled soft robotic arm with embedded gels and mounted gripper. (a) The top graph plots the state of the gripper and the manipulator modules. The rest of the plots in (a)

are the read intensities by the embedded gels in each bellows. (b) Images of the actuation sequence.

4.8.2 Robotic manipulation of fabric using soft multi-functional gripper

I construct a robotic manipulation system that combines the soft multi-functional gripper from Chapter 3 with the soft robotic arm (Fig. 21-(a)). The soft robotic arm can provide safer interactions for human operators during complicated fabric handling processes. I mount two grippers at the end of the soft robotic arm to carry out lifting and folding tasks with a fabric sheet. Initial contact between the system and the fabric is detected by a soft pressure sensor, which consisted of liquid metal patterns embedded within an elastomer matrix (Fig. 4. 22-(b)). The grippers then grasp the fabric (Fig. 4. 22-(c)) and transport it to the specified location (Fig. 4. 22-(d)). Finally, the fabric is released by grippers and folded (Fig. 4. 22-(e)).

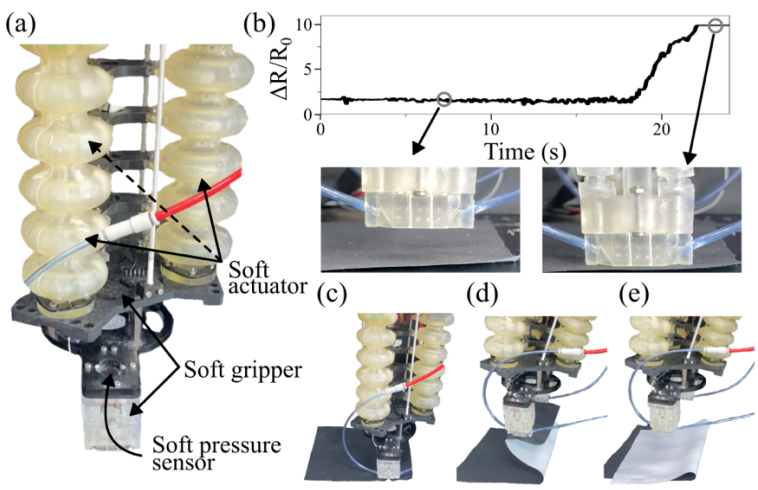

Fig 4. 22. Fabric handling soft manipulation system. (a) Soft robotic arm equipped with the soft grippers. (b) Soft pressure sensor reading up to contact with fabric. (c)-(e) Fabric handling process: fabric gripping, movement to the designated location, and releasing and folding the fabric, respectively.

4.9 Discussion

In this study, I propose the design of bellow-type compliant actuators for building a modularized soft robotic arm and methods of localizing and controlling the arm. Although the proposed system shows the required functionality, there are still rooms for further improvements.

First, the payload of the arm is relatively low due to the compliance of the material. One simple solution to address this issue is to use a stiffer material with modification of the tactile sensing channels to keep the high sensitivity to touch even with the increased stiffness. Another possibility is to make manipulator modules with different structural stiffnesses. The module in the proximal side that need to bear the weights of the other module as well as the object for manipulation can be stiffer than the module in the distal side.

Second, the string sensors may degrade the control performance of the arm since the they are externally exposed and susceptible to contacts made to the string sensors directly. By moving them to inside the bellow, unintended perturbations are prevented and consequently the soft robotic arm is more reliable and stable in physical interactions between the robot and humans.

Lastly, the TENG sensors are an effective method to detect human touches. However, they are responsive only to physical contacts but not to any objects in proximity. It is sometimes useful to recognize objects or humans in proximity that approach to the robot. One possible solution is to use organogel channels as a proximity sensor by measuring the change in capacitance [179], [180].

Chapter 5. Conclusion

This thesis suggests an automation method for legacy production machines, and a novel soft gripper and a robotic arm for fabric handling. Chapter 2 provides automated sewing system enabled by machine vision. Chapter 3 addresses the soft gripper for delicate fabric handling and Chapter 4 covers the soft robotic arm for safe interaction with humans.

In constructing a smart manufacturing environment, I consider the automation of existing production equipment to be basic. These traditional production machines perform repetitive tasks with precision, but they require human intervention for operation, and are lack of flexibility because the machines are specialized certain tasks. To make production equipment more intelligent, machine vision is key to automating existing production equipment, as it mainly enables autonomous object recognition, inspecting the quality of intermediate parts or final product, and monitoring manufacturing processes. Once the existing production equipment is automated, the next step is to seamlessly connect between production equipment. From this perspective, a gripper that handling fabrics is important. Fabrics used in garment manufacturing are unstructured and highly flexible. These characteristics make handling difficult with conventional grippers. To overcome this issue, I devise a soft gripper that fuses pinching and suction mechanisms in a single structure. The gripper can pinch air-permeable porous fabric and grip non-air-permeable coated fabrics using vacuum suction. In addition, the gripper can separate a single sheet from a stack regardless of an air permeability of the fabric. The proposed gripper enables the fabric handling, and the next step is

manipulating the gripper. In the smart manufacturing environment, since human-centric production is emphasized, robots play a role of assisting human. These robots require complex motion and functional interaction with humans. To meet this requirement, I devise a soft robotic arm consisting of soft bellows for actuation and design an integrated structure that embeds organogel below the surface of the bellow. The soft robotic arm enables contract, expansion, and bending in all directions and recognizing human contact as well. Chapter 2 introduces automated sewing system. A seam line is detected and an additional path for sewing can be generated based on the detected seam line by a deep learning model and algorithms for image processing. The proposed sewing machine can automatically sew along the generated path. Chapter 3 introduces a soft gripper for handling delicate fabrics. The complex design for multi-actuation of pinching and suction is presented. In addition, multi-functional compliant structure is introduced for adaptive contact and distribution of applied load. The gripper grips a fabric using both pinching and suction in a single structure. Chapter 4 introduces a soft modularized robotic arm with proprioceptive receptors for functional interacting with humans to perform tasks.

For future work, I plan to integrate an actively controlled multi-functional compliant structure to the soft gripper. Protruding length of 0.25 mm is not sufficient for the fabric with exceeding 0.25 mm thickness, and penetrates multiple sheets when gripping the fabric with thickness of less than 0.25 mm. Therefore, by adding an actuation to the current compliant structure, the protruding length can be actively adjusted to reduce failures during single sheet separation and enable reliable engagement. In addition, by redesigning the compliant structure to allow for twisting, so that it can be aligned parallel to the

edges of the fabric. Next, I plan to add functionality to the soft bellow. By integrating the string strain sensor inside the bellow, the length of the actuator can be measured directly. Currently, the bellow length is estimated after repeatedly calculating the gradient descent operation, which requires about 30 msec. on the edge device. However, through integration of the sensor, the bellow length can be measured directly, enhancing a higher control loop frequency. In addition, I plan to integrate a granular jamming structure to compensate for the low stiffness of the soft bellow structure. This makes the base manipulator module of the soft robotic arm stiff and reduces the external noise or actuation of connected manipulator module. Lastly, I plan to construct simulation environment.

Bibliography

[1] E. Lee, "The Past, Present and Future of Cyber-Physical Systems: A Focus on Models," *Sens.*, vol. 15, no. 3, pp. 4837–4869, Feb. 2015, doi: 10.3390/s150304837.

[2] H. Chen, "Applications of Cyber-Physical System: A Literature Review," *J. Ind. Integr. Manage.*, vol. 02, no. 03, p. 1750012, Sep. 2017, doi: 10.1142/S2424862217500129.

[3] B. Chen, J. Wan, L. Shu, P. Li, M. Mukherjee, and B. Yin, "Smart Factory of Industry 4.0: Key Technologies, Application Case, and Challenges," *IEEE Access*, vol. 6, pp. 6505–6519, 2018, doi: 10.1109/ACCESS.2017.2783682.

[4] W. K. Jung *et al.*, "Appropriate Smart Factory for SMEs: Concept, Application and Perspective," *Int. J. Precis. Eng. Manuf.*, vol. 22, no. 1, pp. 201–215, Jan. 2021, doi: 10.1007/s12541-020-00445-2.

[5] E. Hozdić, "SMART FACTORY FOR INDUSTRY 4.0: A REVIEW," *Int. J. Mod. Manuf. Technol.*, 2015.

[6] G. Büchi, M. Cugno, and R. Castagnoli, "Smart factory performance and Industry 4.0," *Technol. Forecasting Social Change*, vol. 150, Jan. 2020, doi: 10.1016/j.techfore.2019.119790.

[7] M. Sony and S. Naik, "Key ingredients for evaluating Industry 4.0 readiness for organizations: a literature review," *Benchmarking: Int. J.*, vol. 27, no. 7, pp. 2213–2232, Jan. 2019, doi: 10.1108/BIJ-09-2018-0284.

[8] M. Ghobakhloo, "Industry 4.0, digitization, and opportunities for sustainability," *J. Cleaner Prod.*, vol. 252, p. 119869, Apr. 2020, doi: 10.1016/j.jclepro.2019.119869.

[9] J. Lee *et al.*, "Key Enabling Technologies for Smart Factory in Automotive Industry: Status and Applications," *Int. J. Precis. Eng. Manuf.-Smart Technol.*, vol. 1, no. 1, pp. 93–105, Jan. 2023, doi: 10.57062/ijpem-st.2022.0017.

[10] D. Cemernek, H. Gursch, and R. Kern, "Big data as a promoter of industry 4.0: Lessons of the semiconductor industry," in *15th Int. Conf. Ind. Inf. (INDIN)*, IEEE, Jul. 2017, pp. 239–244. doi: 10.1109/INDIN.2017.8104778.

[11] B. Ding, "Pharma Industry 4.0: Literature review and research opportunities in sustainable pharmaceutical supply chains," *Process Saf. Environ. Prot.*, vol. 119, pp. 115–130, Oct. 2018, doi: 10.1016/j.psep.2018.06.031.

[12] S. Paul *et al.*, "Industry 4.0 Applications for Medical/Healthcare Services," *J. Sens. Actuator Netw.*, vol. 10, no. 3, p. 43, Jun. 2021, doi: 10.3390/jsan10030043.

[13] A. Hassoun *et al.*, "The fourth industrial revolution in the food industry—Part I: Industry 4.0 technologies," *Crit. Rev. Food Sci. Nutr.*, pp. 1–17, Feb. 2022, doi: 10.1080/10408398.2022.2034735.

[14] R. French, M. Benakis, and H. Marin-Reyes, "Intelligent sensing for robotic re-manufacturing in aerospace — An industry 4.0 design based prototype," in *Int. Symp. Rob. Intell. Sens. (IRIS)*, IEEE, Oct. 2017, pp.

272–277. doi: 10.1109/IRIS.2017.8250134.
[15] X. Xu, Y. Lu, B. Vogel-Heuser, and L. Wang, "Industry 4.0 and Industry 5.0—Inception, conception and perception," *J. Manuf. Syst.*, vol. 61, pp. 530–535, Oct. 2021, doi: 10.1016/j.jmsy.2021.10.006.
[16] J. Leng *et al.*, "Industry 5.0: Prospect and retrospect," *J. Manuf. Syst.*, vol. 65, pp. 279–295, Oct. 2022, doi: 10.1016/j.jmsy.2022.09.017.
[17] P. K. R. Maddikunta *et al.*, "Industry 5.0: A survey on enabling technologies and potential applications," *J. Ind. Inf. Integr.*, vol. 26, p. 100257, Mar. 2022, doi: 10.1016/j.jii.2021.100257.
[18] J. Bellemare, "Fashion Apparel Industry 4.0 and Smart Mass Customization Approach for Clothing Product Design," *Customization 4.0: Proc. 9th World Mass Customization & Personalization Conf* (MCPC 2017). 2018, pp. 619–633. doi: 10.1007/978-3-319-77556-2_39.
[19] E. Gökalp, M. Onuralp Gökalp, and P. Erhan Eren, "Industry 4.0 Revolution in Clothing and Apparel Factories: Apparel 4.0 Cloud Computing Based Predictive Maintenance Framework for Medical Imaging Devices View project Industry 4.0 From the Management Information Systems Perspectives 169 INDUSTRY 4.0 REVOLUTION IN CLOTHING AND APPAREL FACTORIES: APPAREL 4.0", *Ind. 4*, 2018, doi: 10.3726/b15120/21.
[20] S. Ahmad, S. Miskon, R. Alabdan, and I. Tlili, "Towards Sustainable Textile and Apparel Industry: Exploring the Role of Business Intelligence Systems in the Era of Industry 4.0," *Sustainability*, vol. 12, no. 7, p. 2632, Mar. 2020, doi: 10.3390/su12072632.
[21] G. E. H. Wijewardhana, S. K. Weerabahu, J. L. D. Nanayakkara, and P. Samaranayake, "New product development process in apparel industry using Industry 4.0 technologies," *Int. J. Prod. Perform. Manage.*, vol. 70, no. 8, pp. 2352–2373, Nov. 2021, doi: 10.1108/IJPPM-02-2020-0058.
[22] Y. Liu, Y. Liu, S. Xu, K. Cheng, S. Masuko, and J. Tanaka, "Comparing VR- and AR-Based Try-On Systems Using Personalized Avatars," *Electron. (Basel)*, vol. 9, no. 11, p. 1814, Nov. 2020, doi: 10.3390/electronics9111814.
[23] S. Idrees, G. Vignali, and S. Gill, "Interactive Marketing with Virtual Commerce Tools: Purchasing Right Size and Fitted Garment in Fashion Metaverse," in *The Palgrave Handb. Interact. Mark.*, Cham: Springer International Publishing, 2023, pp. 329–351. doi: 10.1007/978-3-031-14961-0_15.
[24] I. Pachoulakis, "Augmented Reality Platforms for Virtual Fitting Rooms," *Int. J. Multimedia & Its Appl.*, vol. 4, no. 4, pp. 35–46, Aug. 2012, doi: 10.5121/ijma.2012.4404.
[25] F. Baytar, T. Chung, and E. Shin, "Evaluating garments in augmented reality when shopping online," *J. Fashion Market. Manage.: Int. J.*, vol. 24, no. 4, pp. 667–683, Apr. 2020, doi: 10.1108/JFMM-05-2018-0077.
[26] R. Brouet, A. Sheffer, L. Boissieux, and M.-P. Cani, "Design Preserving Garment Transfer," *ACM Trans. Graphics*, 2012, [Online]. Available: www.osinka.ru

[27] M. Zhu, Y. Mori, T. Wakayama, A. Wada, and S. Kawamura, "A Fully Multi-Material Three-Dimensional Printed Soft Gripper with Variable Stiffness for Robust Grasping," *Soft Rob.*, vol. 6, no. 4, pp. 507–519, Aug. 2019, doi: 10.1089/soro.2018.0112.

[28] S. Kim and C. Kyu Park, "Basic garment pattern generation using geometric modeling method," *Int. J. Clothing Sci. Technol.*, vol. 19, no. 1, pp. 7–17, Jan. 2007, doi: 10.1108/09556220710717017.

[29] S. M. Kim and T. J. Kang, "Garment pattern generation from body scan data," *Comput.-Aided Des.*, vol. 35, no. 7, pp. 611–618, Jun. 2003, doi: 10.1016/S0010-4485(02)00081-7.

[30] R. Stojanovic, P. Mitropulos, C. Koulamas, Y. Karayiannis, S. Koubias, and G. Papadopoulos, "Real-Time Vision-Based System for Textile Fabric Inspection," *Real-Time Imaging*, vol. 7, no. 6, pp. 507–518, Dec. 2001, doi: 10.1006/rtim.2001.0231.

[31] M. S. Millán and J. Escofet, "Fabric inspection by near-infrared machine vision," *Opt. Lett.*, vol. 29, no. 13, p. 1440, Jul. 2004, doi: 10.1364/OL.29.001440.

[32] R. G. Saeidi, M. Latifi, S. S. Najar, and A. G. Saeidi, "Computer Vision-Aided Fabric Inspection System for On-Circular Knitting Machine," *Text. Res. J.*, vol. 75, no. 6, pp. 492–497, 2005, doi: 10.1177/0040517505053874.

[33] C.-S. Cho, B.-M. Chung, and M.-J. Park, "Development of Real-Time Vision-Based Fabric Inspection System," *IEEE Trans. Ind. Electron.*, vol. 52, no. 4, pp. 1073–1079, Aug. 2005, doi: 10.1109/TIE.2005.851648.

[34] S. Albawi, T. A. Mohammed, and S. Al-Zawi, "Understanding of a convolutional neural network," in *Int. Conf. Eng. Technol. (ICET)*, IEEE, Aug. 2017, pp. 1–6. doi: 10.1109/ICEngTechnol.2017.8308186.

[35] J. Gu *et al.*, "Recent advances in convolutional neural networks," *Pattern Recognit.*, vol. 77, pp. 354–377, May 2018, doi: 10.1016/j.patcog.2017.10.013.

[36] Q. Xie, D. Li, J. Xu, Z. Yu, and J. Wang, "Automatic Detection and Classification of Sewer Defects via Hierarchical Deep Learning," *IEEE Trans. Autom. Sci. Eng.*, vol. 16, no. 4, pp. 1836–1847, Oct. 2019, doi: 10.1109/TASE.2019.2900170.

[37] H. Kim, W.-K. Jung, Y.-C. Park, J.-W. Lee, and S.-H. Ahn, "Broken stitch detection method for sewing operation using CNN feature map and image-processing techniques," *Expert Syst. Appl.*, vol. 188, p. 116014, Feb. 2022, doi: 10.1016/j.eswa.2021.116014.

[38] M. Ahmed, G. Kibria, and T. Islam, "Estimation of the Standard Minute Value of Polo Shirt by Work Study 5-Books of colleagues View project Assessment of fastness properties of knitted cotton fabric dyed with natural dyes View project Estimation of the Standard Minute Value of Polo Shirt by Work Study," *Article in Int. J. Sci. Eng. Res.*, 2018, [Online]. Available: http://www.ijser.org

[39] V. B. Peralta *et al.*, "Increasing Productivity in Garments Manufacturing through Time Standardization and Work Measurement," in *Proc. Int. Conf. Ind. Eng. Oper. Manage.*, Bangkok, Thailand, 2019, pp. 1719–

1726.
[40] M. ATM, M. ATM, and T. UM, "Using Critical Path Method for Making Process Layout of a T-Shirt within Earliest Finish Time," *J. Text. Sci. Eng.*, vol. 07, no. 05, 2017, doi: 10.4172/2165-8064.1000316.
[41] S. D. V and M. A. Preethi, "Implementation of Industrial Engineering Techniques for Improving Productivity and Its Impact in Controlling Labour Cost in Garment Industry," 2019.
[42] Zhe Xu and E. Todorov, "Design of a highly biomimetic anthropomorphic robotic hand towards artificial limb regeneration," in *Int. Conf. Rob. Autom. (ICRA)*, IEEE, May 2016, pp. 3485–3492. doi: 10.1109/ICRA.2016.7487528.
[43] Leo Jiang, K. Low, J. Costa, R. J. Black, and Y.-L. Park, "Fiber optically sensorized multi-fingered robotic hand," in *2015 IEEE/RSJ Int. Conf. Intell. Rob. Syst. (IROS)*, IEEE, Sep. 2015, pp. 1763–1768. doi: 10.1109/IROS.2015.7353606.
[44] J. Gafford *et al.*, "Shape Deposition Manufacturing of a Soft, Atraumatic, Deployable Surgical Grasper1," *J. Med. Device.*, vol. 8, no. 3, Sep. 2014, doi: 10.1115/1.4027048.
[45] F. Ilievski, A. D. Mazzeo, R. F. Shepherd, X. Chen, and G. M. Whitesides, "Soft Robotics for Chemists," *Angew. Chem.*, vol. 123, no. 8, pp. 1930–1935, Feb. 2011, doi: 10.1002/ange.201006464.
[46] A. Yamaguchi, K. Takemura, S. Yokota, and K. Edamura, "A robot hand using electro-conjugate fluid," in *Int. Conf. Rob. Autom. (ICRA)*, IEEE, May 2011, pp. 5923–5928. doi: 10.1109/ICRA.2011.5979691.
[47] S. Terryn, J. Brancart, D. Lefeber, G. Van Assche, and B. Vanderborght, "Self-healing soft pneumatic robots," *Sci. Rob.*, vol. 2, no. 9, Aug. 2017, doi: 10.1126/scirobotics.aan4268.
[48] H. Zhao, K. O'Brien, S. Li, and R. F. Shepherd, "Optoelectronically innervated soft prosthetic hand via stretchable optical waveguides," *Sci. Rob.*, vol. 1, no. 1, Dec. 2016, doi: 10.1126/scirobotics.aai7529.
[49] E. Brown *et al.*, "Universal robotic gripper based on the jamming of granular material," *PNAS*, vol. 107, no. 44, pp. 18809–18814, Nov. 2010, doi: 10.1073/pnas.1003250107.
[50] Z. Zhakypov, F. Heremans, A. Billard, and J. Paik, "An Origami-Inspired Reconfigurable Suction Gripper for Picking Objects With Variable Shape and Size," *IEEE Rob. Autom. Lett.*, vol. 3, no. 4, pp. 2894–2901, Oct. 2018, doi: 10.1109/LRA.2018.2847403.
[51] Z. Xie *et al.*, "Octopus Arm-Inspired Tapered Soft Actuators with Suckers for Improved Grasping," *Soft Rob.*, vol. 7, no. 5, pp. 639–648, Oct. 2020, doi: 10.1089/soro.2019.0082.
[52] T. Ishikawa and T.-W. Chou, "Nonlinear Behavior of Woven Fabric Composites." *J. Compos. Mater.*, vol. 17, no. 5, pp. 399-413, 1983, doi: 10.1177/002199838301700502.
[53] A. Tabiei and Y. Jiang, "Woven fabric composite material model with material nonlinearity for nonlinear finite element simulation," *Int. J. Solids Struct.*, vol. 36, no. 18, pp. 2757–2771, Jun. 1999, doi: 10.1016/S0020-7683(98)00127-9.
[54] Y. Duan, M. Keefe, T. A. Bogetti, and B. A. Cheeseman, "Modeling

friction effects on the ballistic impact behavior of a single-ply high-strength fabric," *Int. J. Impact. Eng.*, vol. 31, no. 8, pp. 996–1012, Sep. 2005, doi: 10.1016/j.ijimpeng.2004.06.008.

[55] E. Takane, K. Tadakuma, T. Yamamoto, M. Konyo, and S. Tadokoro, "A mechanical approach to realize reflexive omnidirectional bending motion for pneumatic continuum robots," *ROBOMECH J.*, vol. 3, no. 1, Dec. 2016, doi: 10.1186/s40648-016-0067-x.

[56] Giuseppe Del Giudice, Long Wang, Jin-Hui Shen, Karan Joos, and Nabil Simaan, "Continuum Robots for Multi-Scale Motion:Micro-Scale Motion Through Equilibrium Modulation," in *IEEE/RSJ Int. Conf. Intell. Rob. Syst. (IROS)*, Vancouver, BC, Canada, Sep. 2017.

[57] T. Mahl, A. Hildebrandt, and O. Sawodny, "A variable curvature continuum kinematics for kinematic control of the bionic handling assistant," *IEEE Trans. Rob.*, vol. 30, no. 4, pp. 935–949, 2014, doi: 10.1109/TRO.2014.2314777.

[58] Y. Ansari, M. Manti, E. Falotico, Y. Mollard, M. Cianchetti, and C. Laschi, "Towards the development of a soft manipulator as an assistive robot for personal care of elderly people," *Int. J. Adv. Rob. Syst.*, vol. 14, no. 2, Mar. 2017, doi: 10.1177/1729881416687132.

[59] S. Neppalli *et al.*, "OctArm - A soft robotic manipulator," in *IEEE/RSJ Int. Conf. Intell. Rob. Syst. (IROS)*, IEEE, Oct. 2007, pp. 2569–2569. doi: 10.1109/IROS.2007.4399146.

[60] A. Shiva *et al.*, "Tendon-Based Stiffening for a Pneumatically Actuated Soft Manipulator," *IEEE Rob. Autom. Lett.*, vol. 1, no. 2, pp. 632–637, Jul. 2016, doi: 10.1109/LRA.2016.2523120.

[61] T. Ranzani, G. Gerboni, M. Cianchetti, and A. Menciassi, "A bioinspired soft manipulator for minimally invasive surgery," *Bioinspir Biomim*, vol. 10, no. 3, p. 035008, May 2015, doi: 10.1088/1748-3190/10/3/035008.

[62] X. Wang *et al.*, "Eye-in-Hand Visual Servoing Enhanced with Sparse Strain Measurement for Soft Continuum Robots," *IEEE Rob. Autom. Lett.*, vol. 5, no. 2, pp. 2161–2168, Apr. 2020, doi: 10.1109/LRA.2020.2969953.

[63] P. Werner, M. Hofer, C. Sferrazza, and R. D'Andrea, "Vision-based proprioceptive sensing: Tip position estimation for a soft inflatable bellow actuator," in *Int. Conf. Intell. Rob. Syst. (IROS)*, IEEE, Oct. 2020, pp. 8889–8896. doi: 10.1109/IROS45743.2020.9341271.

[64] M. M. Dalvand, S. Nahavandi, and R. D. Howe, "High speed vision-based 3D reconstruction of continuum robots," in *Int. Conf. Syst., Man, Cybern., SMC 2016 – Conf. Proc.*, IEEE, Feb. 2017, pp. 618–623. doi: 10.1109/SMC.2016.7844309.

[65] M. W. Hannan and I. D. Walker, "Real-time shape estimation for continuum robots using vision," *Robotica*, vol. 23, no. 5, pp. 645–651, Sep. 2005, doi: 10.1017/S0263574704001018.

[66] D. B. Camarillo, K. E. Loewke, C. R. Carlson, and J. K. Salisbury, "Vision based 3-D shape sensing of flexible manipulators," in *Int. Conf. Rob. Autom. (ICRA)*, IEEE, May 2008, pp. 2940–2947. doi: 10.1109/ROBOT.2008.4543656.

[67] H. Lasi, P. Fettke, H.-G. Kemper, T. Feld, and M. Hoffmann, "Industry

4.0," *Bus. Inf. Syst. Eng.*, vol. 6, no. 4, pp. 239–242, Aug. 2014, doi: 10.1007/s12599-014-0334-4.

[68] C. Cronin, A. Conway, and J. Walsh, "Flexible manufacturing systems using IIoT in the automotive sector," *Procedia Manuf.*, vol. 38, pp. 1652–1659, 2019, doi: 10.1016/j.promfg.2020.01.119.

[69] N. S. Arden, A. C. Fisher, K. Tyner, L. X. Yu, S. L. Lee, and M. Kopcha, "Industry 4.0 for pharmaceutical manufacturing: Preparing for the smart factories of the future," *Int. J. Pharm.*, vol. 602, p. 120554, Jun. 2021, doi: 10.1016/j.ijpharm.2021.120554.

[70] J. Moyne and J. Iskandar, "Big Data Analytics for Smart Manufacturing: Case Studies in Semiconductor Manufacturing," *Processes*, vol. 5, no. 3, p. 39, Jul. 2017, doi: 10.3390/pr5030039.

[71] S. Lee *et al.*, "Implementation of an Automated Manufacturing Process for Smart Clothing: The Case Study of a Smart Sports Bra," *Processes*, vol. 9, no. 2, p. 289, Feb. 2021, doi: 10.3390/pr9020289.

[72] S. Ku, J. Myeong, H.-Y. Kim, and Y.-L. Park, "Delicate Fabric Handling Using a Soft Robotic Gripper With Embedded Microneedles," *IEEE Rob. Autom. Lett.*, vol. 5, no. 3, pp. 4852–4858, Jul. 2020, doi: 10.1109/LRA.2020.3004327.

[73] E. Torgerson and F. W. Paul, "Vision-guided robotic fabric manipulation for apparel manufacturing," *IEEE Control Systems Magazine*, vol. 8, no. 1, pp. 14–20, Feb. 1988, doi: 10.1109/37.463.

[74] Ltd. Brother Industries, "Brother Electronic Controlled Programmable Sewing Machine with Vision Camera System JJB," *https://www.brother-usa.com/products/7905387*.

[75] J.-Y. Lee, D.-H. Lee, J.-H. Park, and J.-H. Park, "Study on sensing and monitoring of sewing machine for textile stream smart manufacturing innovation," in *24th Int. Conf. Mechatron. Mach. Vision Pract. (M2VIP)*, IEEE, Nov. 2017, pp. 1–3. doi: 10.1109/M2VIP.2017.8211433.

[76] Y. Li, W. Zhao, and J. Pan, "Deformable Patterned Fabric Defect Detection With Fisher Criterion-Based Deep Learning," *IEEE Trans. Autom. Sci. Eng.*, vol. 14, no. 2, pp. 1256–1264, Apr. 2017, doi: 10.1109/TASE.2016.2520955.

[77] P. R. Jeyaraj and E. R. Samuel Nadar, "Computer vision for automatic detection and classification of fabric defect employing deep learning algorithm," *Int. J. Clothing Sci. Technol.*, vol. 31, no. 4, pp. 510–521, Aug. 2019, doi: 10.1108/IJCST-11-2018-0135.

[78] A. Shahriar, "The Optimization of Knitted T-Shirt for Rapid Production Process," *Int. J. Text. Sci.,* 2019, doi: 10.5923/j.textile.20190801.03.

[79] R. E. Glock and Grace I. Kunz, *Apparel Manufacturing: Sewn Product Analysis*. Pearson/Prentice Hall, 2005.

[80] G. Li, C. M. Haslegrave, and E. N. Corlett, "Factors affecting posture for machine sewing tasks," *Appl. Ergon.*, vol. 26, no. 1, pp. 35–46, Feb. 1995, doi: 10.1016/0003-6870(94)00005-J.

[81] T. Gries and V. Lutz, "Application of robotics in garment manufacturing," in *Autom. Garment Manuf.*, Elsevier, 2018, pp. 179–197. doi: 10.1016/B978-0-08-101211-6.00008-2.

[82] R. C. Winck, S. Dickerson, W. J. Book, and J. D. Huggins, "A novel

approach to fabric control for automated sewing," in *IEEE/ASME Int. Conf. Adv. Intell. Mechatron.*, IEEE, Jul. 2009, pp. 53–58. doi: 10.1109/AIM.2009.5230040.

[83] C. W. M. Yuen, W. K. Wong, S. Q. Qian, D. D. Fan, L. K. Chan, and E. H. K. Fung, "Fabric Stitching Inspection Using Segmented Window Technique and BP Neural Network," *Text. Res. J.*, vol. 79, no. 1, pp. 24–35, Jan. 2009, doi: 10.1177/0040517508090503.

[84] I. G. Mariolis and E. S. Dermatas, "Automated assessment of textile seam quality based on surface roughness estimation," *J. Text. Inst.*, vol. 101, no. 7, pp. 653–659, Jun. 2010, doi: 10.1080/00405000902732883.

[85] R. Brad, L. Barac, and R. Brad, "Defect Detection Techniques for Airbag Production Sewing Stages," *J. Text.*, vol. 2014, pp. 1–7, Feb. 2014, doi: 10.1155/2014/738504.

[86] B. Zhu, J. Liu, R. Pan, W. Gao, and J. Liu, "Seam detection of inhomogeneously textured fabrics based on wavelet transform," *Text. Res. J.*, vol. 85, no. 13, pp. 1381–1393, Aug. 2015, doi: 10.1177/0040517514555796.

[87] R. Pan, W. Gao, W. Li, and B. Xu, "Image analysis for seam-puckering evaluation," *Text. Res. J.,* vol. 87, no. 20, pp. 2513–2523, Dec. 2017, doi: 10.1177/0040517516673330.

[88] L. Torrey and J. Shavlik, "Transfer Learning," *Handb. Res. Mach. Learn. Appl. Trends: Algorithms, Methods Tech.,* IGI global, 2010, pp. 242-264.

[89] G. Jocher *et al.*, "ultralytics/yolov5: v6.1 - TensorRT, TensorFlow Edge TPU and OpenVINO Export and Inference." doi: 10.5281/zenodo.6222936.

[90] A. Chandio *et al.*, "Precise Single-stage Detector," *arXiv Prepr.*, Oct. 2022, [Online]. Available: http://arxiv.org/abs/2210.04252

[91] J. Ren *et al.*, "Accurate Single Stage Detector Using Recurrent Rolling Convolution," in *Proc. IEEE Conf. Comput. Vision Pattern Recognit.*, 2017, pp. 5420–5428. [Online]. Available: https://github.com/xiaohaoChen/rrc_detection

[92] Z. Li, C. Peng, G. Yu, X. Zhang, Y. Deng, and J. Sun, "Light-Head R-CNN: In Defense of Two-Stage Object Detector," *arXiv Prepr.*, Nov. 2017, [Online]. Available: http://arxiv.org/abs/1711.07264

[93] S. Ren, K. He, R. Girshick, and J. Sun, "Faster R-CNN: Towards Real-Time Object Detection with Region Proposal Networks," *Adv. Neural Inf. Process. Syst. 28*, 2015, [Online]. Available: https://github.com/

[94] Karel Zuiderveld, *Contrast limited adaptive histogram equalization*. Graphics gems IV, 1994.

[95] A. Savitzky and M. J. E, "Smoothing and Differentiation of Data by Simplified Least Squares Procedures," *Anal. Chem.*, Vol. 36, no. 8. pp. 1627-1639, 1951. [Online]. Available: https://pubs.acs.org/sharingguidelines

[96] M. Quigley *et al.*, "ROS: an open-source Robot Operating System," *ICRA Workshop Open Source Software*, [Online]. Available: http://stair.stanford.edu

[97] J. Canny, "A Computational Approach to Edge Detection," *IEEE Trans.*

Pattern. Anal. Mach. Intell., vol. PAMI-8, no. 6, pp. 679–698, Nov. 1986, doi: 10.1109/TPAMI.1986.4767851.

[98] Xin Wang, "Laplacian Operator-Based Edge Detectors," *IEEE Trans. Pattern. Anal. Mach. Intell.*, vol. 29, no. 5, pp. 886–890, May 2007, doi: 10.1109/TPAMI.2007.1027.

[99] N. Kanopoulos, N. Vasanthavada, and R. L. Baker, "Design of an image edge detection filter using the Sobel operator," *IEEE J. Solid-State Circuits*, vol. 23, no. 2, pp. 358–367, Apr. 1988, doi: 10.1109/4.996.

[100] M. Hermann, T. Pentek, and B. Otto, "Design Principles for Industrie 4.0 Scenarios," in *49th Hawaii Int. Conf. Syst. Sci. (HICSS)*, IEEE, Jan. 2016, pp. 3928–3937. doi: 10.1109/HICSS.2016.488.

[101] S. Hankammer, K. Nielsen, F. T. Piller, G. Schuh, and N. Wang, "Customization 4.0," in *Springer International Publishing (Springer Proceedings in Business and Economics)*, S. Hankammer, K. Nielsen, F. T. Piller, G. Schuh, and N. Wang, Eds., in Springer Proceedings in Business and Economics. Cham: Springer International Publishing, 2018. doi: 10.1007/978-3-319-77556-2.

[102] Zhe Xu and E. Todorov, "Design of a highly biomimetic anthropomorphic robotic hand towards artificial limb regeneration," in *Int. Conf. Rob. Autom. (ICRA)*, IEEE, May 2016, pp. 3485–3492. doi: 10.1109/ICRA.2016.7487528.

[103] J. K. Parker, R. Dubey, F. W. Paul, and R. J. Becker, "Robotic Fabric Handling for Automating Garment Manufacturing," *J. Eng. Ind.*, vol. 105, no. 1, pp. 21–26, Feb. 1983, doi: 10.1115/1.3185859.

[104] P. N. Koustoumpardis and N. A. Aspragathos, "A Review of Gripping Devices for Fabric Handling," *Hand*, vol. 19, pp 20, 2004.

[105] P. M. Taylor, D. M. Pollett, and M. T. Grieβer, "Pinching grippers for the secure handling of fabric panels," *Assem. Autom.*, vol. 16, no. 3, pp. 16–21, Sep. 1996, doi: 10.1108/01445159610126357.

[106] A. A. Brotherton and David J. Tyler, *Clupicker performance and flexible apparel automation*. Hollings Apparel Industry Review 3.2, 1986.

[107] R. Kolluru, K. P. Valavanis, A. Steward, and M. J. Sonnier, "A flat surface robotic gripper for handling limp material," *IEEE Rob. Autom. Mag.*, vol. 2, no. 3, pp. 19–26, 1995, doi: 10.1109/100.414922.

[108] J. Schmalz GmbH, "Needle Gripper." https://www.emicorp.com/products/214/Needle-Grippers (accessed Apr. 03, 2023).

[109] EMI Corp., "Needle Gripper." https: //www.schmalz.com/en/vacuum-technology-for-automation/vacuum- (accessed Apr. 03, 2023).

[110] P. M. Taylor, G. J. Monkman, and G. E. Taylor, "Electrostatic grippers for fabric handling," in *Proc. Int. Conf. Rob. Autom.*, IEEE Comput. Soc. Press, pp. 431–433, 1988, doi: 10.1109/ROBOT.1988.12086.

[111] Zhengwen Zhang, "Modeling and analysis of electrostatic force for robot handling of fabric materials," *IEEE/ASME Trans. Mechatron.*, vol. 4, no. 1, pp. 39–49, Mar. 1999, doi: 10.1109/3516.752083.

[112] Y. Ebraheem, E. Drean, and D. C. Adolphe, "Universal gripper for fabrics – design, validation and integration," *Int. J. Clothing Sci.*

Technol., vol. 33, no. 4, pp. 643–663, 2020, doi: 10.1108/IJCST-11-2019-0180.

[113] C. B. Renaud, H. S. Gill, and I. C. Potter, "Relationships between the diets and characteristics of the dentition, buccal glands and velar tentacles of the adults of the parasitic species of lamprey," *J. Zool.*, vol. 278, no. 3, pp. 231–242, Jul. 2009, doi: 10.1111/j.1469-7998.2009.00571.x.

[114] S. J. Yoon, M. Choi, B. Jeong, and Y.-L. Park, "Elongatable Gripper Fingers With Integrated Stretchable Tactile Sensors for Underactuated Grasping and Dexterous Manipulation," *IEEE Trans. Rob.*, vol. 38, no. 4, pp. 2179–2193, Aug. 2022, doi: 10.1109/TRO.2022.3144949.

[115] VacMotion Inc., "Suction Cups, Vacuum Cups, Vacuum Pads." https://www.vacmotion.com/ Products/Main SuctionCups.aspx (accessed Mar. 31, 2023).

[116] Festo Co. Ltd., "Octopus Griper." https://www.festo.com/kr/ko/c/jepum/gongjang-jadonghwa/ jingong-gisul/jingong-heubcagkeob-id pim113/ (accessed Mar. 31, 2023).

[117] T. T. Hoang, P. T. Phan, M. T. Thai, N. H. Lovell, and T. N. Do, "Bio-Inspired Conformable and Helical Soft Fabric Gripper with Variable Stiffness and Touch Sensing," *Adv. Mater. Technol.*, vol. 5, no. 12, p. 2000724, Dec. 2020, doi: 10.1002/admt.202000724.

[118] S. Song, D. Drotlef, D. Son, A. Koivikko, and M. Sitti, "Adaptive Self-Sealing Suction-Based Soft Robotic Gripper," *Adv. Sci.*, vol. 8, no. 17, p. 2100641, Sep. 2021, doi: 10.1002/advs.202100641.

[119] J. Guo, K. Elgeneidy, C. Xiang, N. Lohse, L. Justham, and J. Rossiter, "Soft pneumatic grippers embedded with stretchable electroadhesion," *Smart Mater. Struct.*, vol. 27, no. 5, p. 055006, May 2018, doi: 10.1088/1361-665X/aab579.

[120] X. Zeng and H.-J. Su, "A High Performance Pneumatically Actuated Soft Gripper Based on Layer Jamming," *J Mech Robot*, vol. 15, no. 1, Feb. 2023, doi: 10.1115/1.4053857.

[121] Y. Hao *et al.*, "A Multimodal, Enveloping Soft Gripper: Shape Conformation, Bioinspired Adhesion, and Expansion-Driven Suction," *IEEE Trans. Rob.*, vol. 37, no. 2, pp. 350–362, Apr. 2021, doi: 10.1109/TRO.2020.3021427.

[122] F. Liu, F. Sun, B. Fang, X. Li, S. Sun, and H. Liu, "Hybrid Robotic Grasping With a Soft Multimodal Gripper and a Deep Multistage Learning Scheme," *IEEE Trans. Rob.*, vol. 39, no. 3, pp. 2379–2399, Jun. 2023, doi: 10.1109/TRO.2023.3238910.

[123] S. Jain, S. Dontu, J. E. M. Teoh, and P. Valdivia Y Alvarado, "A Multimodal, Reconfigurable Workspace Soft Gripper for Advanced Grasping Tasks," *Soft Rob.*, Nov. 2022, doi: 10.1089/soro.2021.0225.

[124] D. Wang, X. Wu, J. Zhang, and Y. Du, "A Pneumatic Novel Combined Soft Robotic Gripper with High Load Capacity and Large Grasping Range," *Actuators*, vol. 11, no. 1, p. 3, Dec. 2021, doi: 10.3390/act11010003.

[125] Y. Chen, D. W. Lloyd, and S. C. Harlock, "Mechanical Characteristics of Coated Fabrics," *J. Text. Inst.*, vol. 86, no. 4, pp. 690–700, Jan. 1995,

doi: 10.1080/00405009508659045.
[126] H. Steven George and V. Praburaj, *Materials and Technology for Sportswear and Performance Apparel*. CRC Press, 2015.
[127] E. Ono, S. Nishikawa, H. Ichijo, and N. Aisaka, "New robot hand for cloth handling.," *Sen'i Gakkaishi*, vol. 48, no. 9, pp. 501–506, 1992, doi: 10.2115/fiber.48.9_501.
[128] I. D. Dadiotis, J. S. Sakellariou, and P. N. Koustoumpardis, "Development of a Low-Cost Force Sensory System for Force Control via Small Grippers of Cooperative Mobile Robots Used for Fabric Manipulation," *Int. Conf. Rob. Alpe-Adia Danube Region*, 2021, pp. 47–58. doi: 10.1007/978-3-030-75259-0_6.
[129] P. I. Kaltsas, P. N. Koustoumpardis, and P. G. Nikolakopoulos, "A Review of Sensors Used on Fabric-Handling Robots," *Mach.*, vol. 10, no. 2, p. 101, Jan. 2022, doi: 10.3390/machines10020101.
[130] R. S. Sabeenian and M. E. Paramasivam, "Defect detection and identification in textile fabrics using Multi Resolution Combined Statistical and Spatial Frequency Method," in *Int. Adv. Comput. Conf. (IACC)*, IEEE, Feb. 2010, pp. 162–166. doi: 10.1109/IADCC.2010.5423017.
[131] E. Ono and Kunikatsu Takase, "On better pushing for picking a piece of fabric from layers," in *Int. Conf. Rob. Biomimetics (ROBIO)*, IEEE, Dec. 2007, pp. 589–594. doi: 10.1109/ROBIO.2007.4522228.
[132] Sachin, Z. Wang, T. Matsuno, and S. Hirai, "Analytical Modeling of a Membrane-Based Pneumatic Soft Gripper," *IEEE Rob. Autom. Lett.*, vol. 7, no. 4, pp. 10359–10366, Oct. 2022, doi: 10.1109/LRA.2022.3183794.
[133] C. Tawk, H. Zhou, E. Sariyildiz, M. in het Panhuis, G. M. Spinks, and G. Alici, "Design, Modeling, and Control of a 3D Printed Monolithic Soft Robotic Finger With Embedded Pneumatic Sensing Chambers," *IEEE/ASME Trans. Mechatron.*, vol. 26, no. 2, pp. 876–887, Apr. 2021, doi: 10.1109/TMECH.2020.3009365.
[134] C. Tawk, A. Gillett, M. in het Panhuis, G. M. Spinks, and G. Alici, "A 3D-Printed Omni-Purpose Soft Gripper," *IEEE Trans. Rob.*, vol. 35, no. 5, pp. 1268–1275, Oct. 2019, doi: 10.1109/TRO.2019.2924386.
[135] Matthews-Fairbanks and Jennifer Lynne, *Pattern Design: Fundamentals: Construction and Pattern Drafting for Fashion Design*. Fairbanks Publishing LLC, 2018.
[136] B. Kumar, A. K. Jaiswal, and B. Kumar, "Vacuum Cup Grippers for Material Handling In Industry," *Int. J. Sci. Technol.*, vol. 7, no. 1, pp. 1–8, 2017, [Online]. Available: https://www.researchgate.net/publication/317823110
[137] M. S. Xavier, A. J. Fleming, and Y. K. Yong, "Finite Element Modeling of Soft Fluidic Actuators: Overview and Recent Developments," *Adv. Intell. Syst.*, vol. 3, no. 2, p. 2000187, Feb. 2021, doi: 10.1002/aisy.202000187.
[138] M. Wei, "The Theory of the Cantilever Stiffness Test," *J. Text. Inst.*, vol. 80, no. 1, pp. 98–106, Jan. 1989, doi: 10.1080/00405008908659188.
[139] A. G. Frank, L. S. Dalenogare, and N. F. Ayala, "Industry 4.0

technologies: Implementation patterns in manufacturing companies," *Int. J. Prod. Econ.*, vol. 210, pp. 15–26, Apr. 2019, doi: 10.1016/j.ijpe.2019.01.004.

[140] T. Ranzani, M. Cianchetti, G. Gerboni, I. De Falco, G. Petroni, and A. Menciassi, "A modular soft manipulator with variable stiffness," in *Joint Workshop New Technol. Comput/Rob. Assisted Surg.*, 2013, pp. 11–13.

[141] P. H. Nguyen, C. Sparks, S. G. Nuthi, N. M. Vale, and P. Polygerinos, "Soft Poly-Limbs: Toward a New Paradigm of Mobile Manipulation for Daily Living Tasks," *Soft Rob.*, vol. 6, no. 1, pp. 38–53, Feb. 2019, doi: 10.1089/soro.2018.0065.

[142] H. D. Yang and A. T. Asbeck, "Design and Characterization of a Modular Hybrid Continuum Robotic Manipulator," *IEEE/ASME Trans. Mechatron.*, vol. 25, no. 6, pp. 2812–2823, Dec. 2020, doi: 10.1109/TMECH.2020.2993543.

[143] X. Jing, J. Jiang, F. Xie, C. Zhang, S. Chen, and L. Yang, "Continuum Manipulator With Rigid-Flexible Coupling Structure," *IEEE Rob. Autom. Lett.*, vol. 7, no. 4, pp. 11386–11393, Oct. 2022, doi: 10.1109/LRA.2022.3199683.

[144] H. Hsu, L.-Y. Liu, L.-Y. Liu, and Y.-C. Su, "3D manufactured, water-powered soft actuators for orthodontic application," *Smart Mater. Struct.*, vol. 27, no. 8, p. 084006, Aug. 2018, doi: 10.1088/1361-665X/aabc2d.

[145] D. K. Patel, A. H. Sakhaei, M. Layani, B. Zhang, Q. Ge, and S. Magdassi, "Highly Stretchable and UV Curable Elastomers for Digital Light Processing Based 3D Printing," *Adv. Mater.*, vol. 29, no. 15, p. 1606000, Apr. 2017, doi: 10.1002/adma.201606000.

[146] B. N. Peele, T. J. Wallin, H. Zhao, and R. F. Shepherd, "3D printing antagonistic systems of artificial muscle using projection stereolithography," *Bioinspiration Biomimetics*, vol. 10, no. 5, p. 055003, Sep. 2015, doi: 10.1088/1748-3190/10/5/055003.

[147] D. Gonzalez, J. Garcia, R. M. Voyles, R. A. Nawrocki, and B. Newell, "Characterization of 3D printed pneumatic soft actuator," *Sens. Actuators A Phys.*, vol. 334, p. 113337, Feb. 2022, doi: 10.1016/j.sna.2021.113337.

[148] M. Schaffner, J. A. Faber, L. Pianegonda, P. A. Rühs, F. Coulter, and A. R. Studart, "3D printing of robotic soft actuators with programmable bioinspired architectures," *Nat. Commun.*, vol. 9, no. 1, p. 878, Feb. 2018, doi: 10.1038/s41467-018-03216-w.

[149] A. Grzesiak, R. Becker, and A. Verl, "The Bionic Handling Assistant: a success story of additive manufacturing," *Assem. Autom.*, vol. 31, no. 4, pp. 329–333, Sep. 2011, doi: 10.1108/01445151111172907.

[150] V. Falkenhahn, T. Mahl, A. Hildebrandt, R. Neumann, and O. Sawodny, "Dynamic Modeling of Bellows-Actuated Continuum Robots Using the Euler–Lagrange Formalism," *IEEE Trans. Rob.*, vol. 31, no. 6, pp. 1483–1496, Dec. 2015, doi: 10.1109/TRO.2015.2496826.

[151] D. Sui, S. Zhao, T. Wang, Y. Liu, Y. Zhu, and J. Zhao, "Design of a Bio-inspired Extensible Continuum Manipulator with Variable Stiffness," *J. Bionic Eng.*, Jul. 2022, doi: 10.1007/s42235-022-00213-0.

[152] A. D. Kapadia, K. E. Fry, and I. D. Walker, “Empirical investigation of closed-loop control of extensible continuum manipulators,” in *IEEE/RSJ Int. Conf. Intell. Rob. Syst. (IROS)*, IEEE, Sep. 2014, pp. 329–335. doi: 10.1109/IROS.2014.6942580.
[153] I. Tamadon, Y. Huan, A. G. Groot, A. Menciassi, and E. Sinibaldi, “Positioning and stiffening of an articulated/continuum manipulator for implant delivery in minimally invasive surgery,” *Int. J. Med. Rob. Comput. Assisted Surg.*, vol. 16, no. 2, Apr. 2020, doi: 10.1002/rcs.2072.
[154] J.-B. Chossat, Y.-L. Park, R. J. Wood, and V. Duchaine, “A Soft Strain Sensor Based on Ionic and Metal Liquids,” *IEEE Sens. J.*, vol. 13, no. 9, pp. 3405–3414, Sep. 2013, doi: 10.1109/JSEN.2013.2263797.
[155] J. Chen *et al.*, “A Liquid Metal Based Super-Stretchable Strain Sensor,” in *Annu. Int. Conf. Nano/Micro Eng. Mol. Syst. (NEMS)*, IEEE, Apr. 2018, pp. 377–380. doi: 10.1109/NEMS.2018.8556925.
[156] D. Zymelka, T. Yamashita, S. Takamatsu, T. Itoh, and T. Kobayashi, “Thin-film flexible sensor for omnidirectional strain measurements,” *Sens. Actuators A Phys.*, vol. 263, pp. 391–397, Aug. 2017, doi: 10.1016/j.sna.2017.05.040.
[157] Yong-Lae Park, Bor-Rong Chen, and R. J. Wood, “Design and Fabrication of Soft Artificial Skin Using Embedded Microchannels and Liquid Conductors,” *IEEE Sens. J.*, vol. 12, no. 8, pp. 2711–2718, Aug. 2012, doi: 10.1109/JSEN.2012.2200790.
[158] Y.-L. Park, C. Majidi, R. Kramer, P. Bérard, and R. J. Wood, “Hyperelastic pressure sensing with a liquid-embedded elastomer,” *J. Micromech. Microeng.*, vol. 20, no. 12, p. 125029, Dec. 2010, doi: 10.1088/0960-1317/20/12/125029.
[159] T. Kim, H.-S. Shin, K.-H. Nam, S. Bergbreiter, and Y.-L. Park, “Soft Airflow Sensors With Artificial Hair Structures and Printed Ionogel Channels for Wind Gust Detection for Small Uncrewed Vehicles,” *IEEE/ASME Trans. Mechatron.*, pp. 1–11, 2023, doi: 10.1109/TMECH.2022.3233669.
[160] J. W. Boley, E. L. White, G. T.-C. Chiu, and R. K. Kramer, “Direct Writing of Gallium-Indium Alloy for Stretchable Electronics,” *Adv. Funct. Mater.*, vol. 24, no. 23, pp. 3501–3507, Jun. 2014, doi: 10.1002/adfm.201303220.
[161] G. Shin, B. Jeon, and Y.-L. Park, “Direct printing of sub-30 μ m liquid metal patterns on three-dimensional surfaces for stretchable electronics,” *J. Micromech. Microeng.,* vol. 30, no. 3, p. 034001, Mar. 2020, doi: 10.1088/1361-6439/ab6dbc.
[162] A. M. M. Breitbarth, C. Hake, and G. Notni, “Measurement accuracy and practical assessment of the lidar camera Intel RealSense L515,” in *Opt. Meas. Syst. Ind. Inspection XII*, P. Lehmann, W. Osten, and A. Albertazzi Gonçalves, Eds., SPIE, Jun. 2021, p. 39. doi: 10.1117/12.2592570.
[163] R. Girshick, “Fast R-CNN,” *Proc. Int. Conf. Comput. Vision.*, IEEE, pp. 1440-1448, 2015, [Online]. Available: https://github.com/rbgirshick/
[164] S. Pan and Z. Zhang, “Fundamental theories and basic principles of

triboelectric effect: A review," *Friction*, vol. 7, no. 1, pp. 2–17, Feb. 2019, doi: 10.1007/s40544-018-0217-7.
[165] C. Wu, A. C. Wang, W. Ding, H. Guo, and Z. L. Wang, "Triboelectric Nanogenerator: A Foundation of the Energy for the New Era," *Adv. Energy Mater.*, vol. 9, no. 1, p. 1802906, Jan. 2019, doi: 10.1002/aenm.201802906.
[166] Y. Lee, W. J. Song, and J.-Y. Sun, "Hydrogel soft robotics," *Mater. Today Phys.*, vol. 15, p. 100258, Dec. 2020, doi: 10.1016/j.mtphys.2020.100258.
[167] C. Yang and Z. Suo, "Hydrogel ionotronics," *Nat. Rev. Mater.*, vol. 3, no. 6, pp. 125–142, May 2018, doi: 10.1038/s41578-018-0018-7.
[168] D. Y. Kim, S. Choi, H. Cho, and J.-Y. Sun, "Electroactive Soft Photonic Devices for the Synesthetic Perception of Color and Sound," *Adv. Mater.*, vol. 31, no. 2, p. 1804080, Jan. 2019, doi: 10.1002/adma.201804080.
[169] Y. Lee, S. H. Cha, Y.-W. Kim, D. Choi, and J.-Y. Sun, "Transparent and attachable ionic communicators based on self-cleanable triboelectric nanogenerators," *Nat. Commun.*, vol. 9, no. 1, p. 1804, May 2018, doi: 10.1038/s41467-018-03954-x.
[170] Y. Lee *et al.*, "Triboresistive Touch Sensing: Grid-Free Touch-Point Recognition Based on Monolayered Ionic Power Generators," *Adv. Mater.*, vol. 34, no. 19, p. 2108586, May 2022, doi: 10.1002/adma.202108586.
[171] Y. Lee, W. Kim, D. Bhatia, H. J. Hwang, S. Lee, and D. Choi, "Cam-based sustainable triboelectric nanogenerators with a resolution-free 3D-printed system," *Nano Energy*, vol. 38, pp. 326–334, Aug. 2017, doi: 10.1016/j.nanoen.2017.06.015.
[172] S. T. Dwiyati, A. Kholil, R. Riyadi, and S. E. Putra, "Influence of layer thickness and 3D printing direction on tensile properties of ABS material," *J. Phys. Conf. Ser.*, vol. 1402, no. 6, p. 066014, Dec. 2019, doi: 10.1088/1742-6596/1402/6/066014.
[173] R. J. Webster and B. A. Jones, "Design and kinematic modeling of constant curvature continuum robots: A review," *Int. J. Rob. Res.*, vol. 29, no. 13, pp. 1661–1683, Nov. 2010, doi: 10.1177/0278364910368147.
[174] M. Hermann and A. Jönsson, "Static Characteristics of Flexible Bellows," *Master Philos. Thesis*, 1997.
[175] D. Drotman, M. Ishida, S. Jadhav, and M. T. Tolley, "Application-Driven Design of Soft, 3-D Printed, Pneumatic Actuators With Bellows," *IEEE/ASME Trans. Mechatron.*, vol. 24, no. 1, pp. 78–87, Feb. 2019, doi: 10.1109/TMECH.2018.2879299.
[176] L. Armijo, "Minimization of functions having Lipschitz continuous first partial derivatives," *Pac. J. Math.*, vol. 16, no. 1, pp. 1–3, Jan. 1966, doi: 10.2140/pjm.1966.16.1.
[177] O. Alghushairy, R. Alsini, T. Soule, and X. Ma, "A Review of Local Outlier Factor Algorithms for Outlier Detection in Big Data Streams," *Big Data Cognit. Comput.*, vol. 5, no. 1, p. 1, Dec. 2020, doi: 10.3390/bdcc5010001.

[178] M. M. Breunig, H.-P. Kriegel, R. T. Ng, and J. Sander, “LOF: identifying density-based local outliers,” in *Proc. ACM SIGMOD Int. Conf. Manage. Data*, New York, NY, USA: ACM, May 2000, pp. 93–104. doi: 10.1145/342009.335388.

[179] S. E. Navarro *et al.*, “Proximity Perception in Human-Centered Robotics: A Survey on Sensing Systems and Applications,” *IEEE Trans. Rob.*, vol. 38, no. 3, pp. 1599–1620, Jun. 2022, doi: 10.1109/TRO.2021.3111786.

[180] J. Kwon *et al.*, “Selectively Stiffening Garments Enabled by Cellular Composites,” *Adv. Mater. Technol.*, vol. 7, no. 9, p. 2101543, Sep. 2022, doi: 10.1002/admt.202101543.

국문초록

스마트 제조 환경은 제조 효율을 높이고 유연한 생산을 가능하게 하며 위험한 환경에서 로봇이 작업자를 대신할 수 있도록 하여 안전성을 높인다. 노동 집약적인 의류 제조 산업도 마찬가지로 자동화된 로봇 시스템에 대한 수요가 높다. 그러나 대상을 인식하는 기술, 원단을 다루는 기능, 사람과 안전하게 상호작용하면서 동시에 원단을 다루는 조작기 등의 부족으로 인해 의류 제조 자동화가 지연되고 있다. 이러한 장애물은 머신 비전을 통한 지능화, 다양한 속성의 직물을 다루는 정교한 그리퍼, 사람의 접촉을 감지하고 본질적인 소프트함으로 충돌로부터 안전한 재질로 제작된 조작기를 통해 극복할 수 있다.

본 논문에서는 의류 생산을 자동화하고 유연한 원단 취급을 지원하기 위한 세 가지 로봇 조작 기술을 제안한다. 첫째, 머신 비전을 통해 사람의 개입 없이 기존 재봉 장비를 자율적으로 구동할 수 있는 자동 재봉 시스템을 제안한다. 둘째, 원단을 섬세하게 다룰 수 있는 소프트 로봇 그리퍼를 제안한다. 셋째, 인간과 안전하게 상호작용할 수 있도록 고유수용감각을 가진 모듈화된 소프트 로봇 팔을 제안한다.

첫번째로, 머신비전과 재봉기기가 결합된 맞춤형 자동화 생산 시스템을 제안한다. 카메라는 옷을 구성하는 패턴이라고 하는 재봉선을 포함하는 디자인된 원단을 촬영한다. 학습된 딥러닝 모델을 통해 이미지에서 재봉선이 포함된 관심 영역(ROI)을 분할하고, 제안한 이미지 처리 알고리즘을 통해 재봉선을 검출한다. 이를 통해 노출 시간과 원단의 색상, 노이즈와 이물질에 관계없이 재봉선 검출이 가능하다. 재봉선을 기반으로 2차 재봉을 위한 경로를 생성하고, 이 경로를 맞춤 제작된 재봉기기에 자동으로 전송하여 2차 재봉을 수행한다.

둘째, 비정형이고 유연성이 높은 원단을 조작하기 위한 소프트 그리퍼를 제안한다. 제안한 소프트 그리퍼는 작은 폼팩터로 구조적 변형을 통해 원단을 집는다. 그리퍼는 직조 간격이 넓어, 공기 투과성이 높은 원단을 집으며, 빳빳하지 않은 코팅된 원단을 집는다. 그리퍼 팁에 내장된 전극으로 정전 용량을 측정하여 집은 원단의 개수를 추정하며, 이를 통해 그리핑 과정을 모니터링하여 작업 수행의 정확도를 높인다. 구조적 변형 기반의 그리핑 방식과, 진공 흡착에 의한 원단을 집는 방식을 하나의 구조에서 구현한 발전된 소프트 그리퍼를 제안한다. 또한 그리퍼에 다기능 컴플라이언트 구조를 추가하여 원단 표면에 적응형으로

밀착하고 그리퍼 끝에 가해지는 과도한 하중을 분산한다. 컴플라이언트 구조에 연결된 공기압 센서가 접촉을 감지하며, 누르는 힘을 제어하여 그리핑 과정을 자동화한다. 전극을 통한 정전용량 측정 방식 외에 카메라와 딥러닝 모델을 통하여 집은 개수를 추정하는 방식을 제안한다. 이는 원단에 대한 사전 정보를 필요로 하지 않아 쉽게 사용이 가능하며, 원단을 집는 프로세스의 신뢰도를 높이고 모니터링을 가능하게 하여 스마트 제조환경 구축에 도움이 된다. 또한 제안한 그리퍼는 공기 투과도를 자동으로 판단하여 원단을 집는 모드를 선택하며, 공기투과도에 상관 없이 원단 스택에서 한 장의 시트를 분리한다.

마지막으로 사람과 안전하게 상호작용할 수 있는 소프트 모듈화된 로봇 팔을 제안한다. 로봇 팔을 구성하는 액추에이터는 공압 벨로우이며, 내부에 오가노젤 채널이 있는 복잡한 구조이지만 3D 프린팅으로 쉽게 제작한다. 오가노젤을 벨로우에 내장해 사람과의 접촉을 독립적으로 인식한다. 로봇 팔을 구성하는 매니퓰레이터 모듈은 공압 벨로우즈, 센싱 솔루션, 제어 시스템으로 구성된다. 매니퓰레이터 모듈은 수축, 팽창 및 전방향 굽힘이 가능하여 이에 대응하는 전방향 소프트 스트링 센서를 제안한다. 매니퓰레이터 모듈은 제안한 소프트 스트링 센서, IMU, 비전을 통해 주변 환경을 인식하고 스트링 센서와 비전 측정 결과를 융합해 제어하거나, 스트링 센서만을 이용하여 폐색 환경 (Occlusion environment)에서 제어된다. 매니퓰레이터 모듈을 여러 개 연결한 소프트 로봇 팔에는 강체 기반의 일반 그리퍼나 원단을 다루는 제안된 소프트 그리퍼가 탑재되어 인간 활동을 보조하거나 원단의 로봇 기반 조작이 가능하다.

키워드: 스마트 제조, 머신 비전, 다기능 복합 구조, 소프트 그리퍼, 소프트 로봇 팔

학번: 2017-23754